University of Alberta

Thermo-mechanical Modelling of Progressing Cavity Pumps and Positive Displacement Motors

by

Daniel Dall'Acqua ©

A thesis submitted to the Faculty of Graduate Studies and Research in partial fulfilment of the requirements for the degree of **Master of Science**

Department of Mechanical Engineering

Edmonton, Alberta

Fall, 2000

National Library of Canada

Acquisitions and Bibliographic Services

395 Wellington Street
Ottawa ON K1A 0N4
Canada

Bibliothèque nationale du Canada

Acquisitions et services bibliographiques

395, rue Wellington
Ottawa ON K1A 0N4
Canada

Your file Votre référence

Our file Notre référence

The author has granted a non-exclusive licence allowing the National Library of Canada to reproduce, loan, distribute or sell copies of this thesis in microform, paper or electronic formats.

L'auteur a accordé une licence non exclusive permettant à la Bibliothèque nationale du Canada de reproduire, prêter, distribuer ou vendre des copies de cette thèse sous la forme de microfiche/film, de reproduction sur papier ou sur format électronique.

The author retains ownership of the copyright in this thesis. Neither the thesis nor substantial extracts from it may be printed or otherwise reproduced without the author's permission.

L'auteur conserve la propriété du droit d'auteur qui protège cette thèse. Ni la thèse ni des extraits substantiels de celle-ci ne doivent être imprimés ou autrement reproduits sans son autorisation.

0-612-59796-2

Canadä

University of Alberta

Library Release Form

Name of Author: Daniel Dall'Acqua

Title of Thesis: Thermo-mechanical Modelling of Progressing Cavity Pumps and Positive Displacement Motors

Degree: Master of Science

Year this Degree Granted: 2000

Permission is hereby granted to the University of Alberta Library to reproduce single copies of this thesis and to lend or sell such copies for private, scholarly, or scientific research purposes only.

The author reserves all other publication and other rights in association with the copyright in the thesis, and except as herein before provided, neither the thesis nor any substantial portion thereof may be printed or otherwise reproduced in any material form whatever without the author's written permission.

9745 – 88th Avenue
Edmonton, Alberta
T6E 2R1

Date: September 28, 2000

University of Alberta

Faculty of Graduate Studies and Research

The undersigned certify that they have read, and recommend to the Faculty of Graduate Studies and Research for acceptance, a thesis entitled **Thermo-Mechanical Modelling of Progressing Cavity Pumps and Positive Displacement Motors** submitted by **Daniel Dall'Acqua** in partial fulfillment of the requirements for the degree of **Master of Science.**

aw Lipsett

Dr. A.W. Lipsett (Co-Supervisor)

Gary Faulkner

Dr. M.G. Faulkner (Co-Supervisor)

Roger W Toogood

Dr. R.W. Toogood

Dr. T.M. Hrudey

Date: Sept. 26, 2000

ABSTRACT

The use of Progressing Cavity Pumps (PCPs) and Positive Displacement Motors (PDMs) in oilfield production and drilling capacities is widespread. Both types of machines consist of a steel rotor rotating within a mating elastomeric stator. Cyclic loading of the stator elastomer generates heat that causes the temperature of the elastomer to climb well above the environment temperature, sometimes resulting in failure or poor performance of the pump or motor unit.

An efficient, pseudo-steady-state thermo-mechanical modelling strategy for determining the stabilised downhole elastomer temperature and associated structural response in PCP and PDM stators is presented. Structural, heat generation, and thermal models form the basis for an iterative solution procedure that may be extended to any configuration of PCP or PDM. Full-scale testing using an instrumented stator shows that the modelling strategy provides a reasonable estimate of the stabilised operating temperature.

For my grandfather Aladar (who was always fascinated by science), my parents (who encouraged me to follow his lead) and my loving wife Michelle and daughter Maia (who graciously accommodate my fascinations).

ACKNOWLEDGEMENTS

The research described in this document was made possible through the support of Weatherford Artificial Lift Systems and Noetic Engineering Inc. Weatherford provided a wealth of helpful information pertaining to their elastomers and pumps, the equipment and facilities required to complete verification testing, and financial support. Noetic provided the computer and finite element software required for the work and a great deal of guidance. In particular, I would like to thank Dr. Trent Kaiser of Noetic Engineering for his contribution to the project. His advice was always insightful and his positive outlook made him a pleasure to work with.

I would like to thank my supervisors, Dr. Bill Lipsett and Dr. Gary Faulkner, for all of their help and support through the course of the project. In addition to the guidance they provided, they made my return to the University of Alberta a pleasant one.

Finally, I would like to thank the Mechanical Engineering Department at the University of Alberta for its financial support, as well as Black Max Downhole Tool Ltd. and the Association of Professional Engineers, Geologists, and Geophysicists of Alberta (APEGGA) for the scholarship funding they provided.

TABLE OF CONTENTS

1 INTRODUCTION 1

2 BACKGROUND 3

2.1 General Principles of PCP and PDM Operation 3

2.1.1 Cross-sectional geometry 4

2.1.2 Axial geometry 6

2.2 Single-lobe Progressing Cavity Pumps 7

2.3 Applications of PCPs and PDMs 11

3 LITERATURE REVIEW 13

3.1 Response and Modelling of Elastomers 13

3.2 Thermomechanical Modelling of Elastomeric Components 14

4 INTRODUCTION TO MODELLING STRATEGY 18

5 STRUCTURAL MODELLING 20

5.1 Material Considerations (Structural Models) 20

5.1.1 Hyperelastic material models 21

5.1.2 Linear approximation to elastomer material response 23

5.1.3 Bulk modulus effects 27

5.1.4 Temperature-sensitive material property considerations and thermal expansion considerations: 28

5.1.5 Approximation to dynamic loading 29

5.2 Structural Finite Element Formulations 29

5.2.1 Continuum element formulations 30

5.2.2 Contact element formulations 31

5.2.3 Mesh density 32

5.3 Two-dimensional Structural Modelling 35

5.3.1 General two-dimensional modelling considerations 35

5.3.2 Description of the models 35

5.3.3 Generalised plane strain assumption 38

5.3.4 Stator boundary conditions 39

5.3.5 Loading 41

5.3.5.a Rotor/stator interference 41

5.3.5.b Thermal expansion 47

5.3.5.c Volumetric swell 49
5.3.5.d Uniform internal pressure 51
5.3.5.e Differential pressure 52
5.3.5.f Friction 54
5.3.6 Results interpretation 55
5.4 Three-dimensional Structural Modelling 56
5.4.1 General three-dimensional modelling considerations 56
5.4.2 Model length 57
5.4.3 Model creation 57
5.4.4 Boundary conditions 59
5.4.5 Loading 62
5.5 2D Equilibrium Position Procedure 64
5.6 Structural Analysis Comparisons 67
5.6.1 Energy comparison criterion 69
5.6.2 Comparison cases 70
5.6.3 Rotor position for rotor/stator interference cases 71
5.6.4 Energy comparisons for rotor/stator interference cases 73
5.6.4.a Pointwise energy comparisons 73
5.6.4.b Planar energy comparisons 77
5.6.5 Modified 2D analysis approach 80
5.6.6 Results of differential pressure comparisons 84
5.6.7 Summary of comparisons 92

6 HEAT GENERATION MODELLING 93
6.1 General Heat Generation Considerations 93
6.2 Material Considerations (Heat Generation) 93
6.2.1 Viscoelastic response 94
6.2.2 Available dynamic test results 97
6.2.3 Application of dynamic test results 97
6.2.4 Frequency, temperature, and amplitude dependence of dynamic material properties 98
6.3 Modelling Strategy 100
6.3.1 Stress and strain history characterisation 100
6.3.2 Heat generation calculations 108
6.3.3 Element heat generation summation 109

7 THERMAL MODELLING 113

7.1 General Thermal Modelling Considerations 113

7.1.1 Steady-state heat transfer 114

7.1.2 Heat transfer to rotor 115

7.1.3 Planar heat transfer 115

7.1.4 Perfect bond at housing inside diameter 117

7.2 Material Considerations (Thermal Modelling) 118

7.3 Thermal Finite Element Formulations 118

7.3.1 Continuum elements 118

7.3.2 Convection elements 119

7.4 Modelling Strategy 119

7.4.1 Mesh density 119

7.4.2 Boundary conditions 120

7.4.2.a Heat transfer at housing outside diameter 121

7.4.2.b Heat transfer at stator inner profile 122

7.4.3 Thermal loading 124

7.4.3.a Hysteresis heat input 124

7.4.3.b Friction heat input 124

7.5 Sample Results 126

8 COUPLED THERMO-MECHANICAL MODELLING 129

8.1 General Thermo-Mechanical Considerations 129

8.2 Iterative Solution Procedure 132

8.2.1 Description 132

8.2.2 Physical relevance of successive iterations 134

8.2.3 Convergence criterion 134

8.2.4 Convergence considerations 136

8.2.5 Convergence optimisation 138

9 VERIFICATION TESTING 145

9.1 Test Objectives 145

9.2 Test Program 146

9.3 Test Setup and Instrumentation 147

9.4 Test Procedure 152

9.5 Test Results 153

9.5.1 General discussion 153

9.5.2 Peak stabilised temperatures ... 156
9.5.3 Stabilised temperature distributions ... 159
9.6 Comparison to Thermo-Mechanical Modelling Results ... 164
9.6.1 Stabilised temperature comparisons ... 164
9.6.2 Temperature profile comparisons ... 172
9.6.3 Hoop strain comparisons ... 174
9.6.4 Error identification ... 175
9.7 Test Conclusions ... 182

10 CONCLUSIONS AND RECOMMENDATIONS ... 184
10.1 Conclusions ... 184
10.2 Recommendations ... 186

REFERENCES ... 188

APPENDIX A 191

LIST OF FIGURES

Figure 2.1. Photographs of single-lobe pump rotor with sectioned stator (left) and single-lobe stators (right). 3

Figure 2.2. Sample two, three, and four-lobe hypocycloids. 4

Figure 2.3. Two, three, and four-lobe profiles generated with hypocycloid paths. 5

Figure 2.4 Rotor motion in stator profile for 1:2 lobe (top) and 2:3 lobe (bottom) geometries with compatible hypocycloids. 6

Figure 2.5. End views of rotor (left) and stator (right) components of a conventional single-lobe pump with associated nomenclature. 8

Figure 2.6. End view of pump showing interaction between rotor and stator. 8

Figure 2.7. Major and minor seal definitions in a single-lobe progressing cavity pump. 9

Figure 2.8. Relative positions of rotor and stator cross-sections at different axial positions. 10

Figure 2.9. PCP and PDM operating configurations. 12

Figure 4.1. Iterative thermomechanical solution strategy. 19

Figure 5.1 Sample uniaxial tension behaviour for two elastomers (adapted from Beatty and Studebaker). 21

Figure 5.2. Sample uniaxial tension data with corresponding Mooney-Rivlin curve and associated linear approximation in terms of engineering stress and engineering strain. 25

Figure 5.3. Sample uniaxial tension data with corresponding Mooney-Rivlin curve and associated linear approximation in terms of Cauchy stress and true strain. 26

Figure 5.4. Continuum elements used to model stator elastomer and housing. 30

Figure 5.5. Improvement of elastomer effective stress contour results with mesh refinement. (Units in MPa) 33

Figure 5.6. Rotor contact element discretisation at contact point in a single-lobe stator. Contact elements are marked with a "1"; continuum elements are numbered. 34

Figure 5.7. Sample stator cross-sections used for two-dimensional modelling. 36

Figure 5.8. Cross-sections of common pump configurations: (a) Conventional single-lobe; (b) Uniform thickness single-lobe; (c) Conventional 2:3 multi-lobe; (d) Modified 2:3 multi-lobe. 37

Figure 5.9. Definition of single-lobe rotor position angle θ. 38

Figure 5.10. Fixed elastomer OD boundary condition used previously. 40

Figure 5.11. Single-lobe pump stator boundary conditions. 40

Figure 5.12. Stress concentration at constraint location on housing due to excessive interference at major seal (90° position). (Stress in MPa) 41

Figure 5.13. Position of seal location(s) in single-lobe cross-section 42

Figure 5.14. Rotor interaction with inner stator profile at time *t* at pump cross-sections spaced one-half rotor pitch apart. 43

Figure 5.15. Eccentric paths of rotor centre for assumed and equilibrium (elliptical) rotor paths. 44

Figure 5.16. Rotor positions used to model quarter rotor cycle 45

Figure 5.17. Sample elastomer effective stress profile with uneven interference on minor seal (i.e., $e_{3D}\neq0$) with rotor at 0° position. (Units in MPa) 47

Figure 5.18. Sample elastomer temperature profile. (Units in °C) 48

Figure 5.19. Thermal expansion schematic. 49

Figure 5.20. Combined thermal/swell loading application strategy for 2D modelling. 51

Figure 5.21. Applied uniform internal pressure loading for 2D model. 52

Figure 5.22. Sample pressure distribution in a single-lobe pump. 52

Figure 5.23. Applied differential pressure profile for 2D half pump model (rotor at 0°). 53

Figure 5.24. Applied differential pressure profile for 2D half pump model at -90°, -22.5°, 22.5°, and 90° rotor positions ((a) through (d) respectively). 54

Figure 5.25. Unrotated 3D stator and rotor meshes 58

Figure 5.26. Rotated 3D stator and rotor meshes 59

Figure 5.27. Nodes used to prevent rigid-body translations of the stator. Nodes A through D are spaced at 90° increments on the outside diameter of the stator housing; node E is an auxiliary node connected to ground through springs. 60

Figure 5.28. End constraints (applied to all face nodes at $x = P_{rotor}$). 62

Figure 5.29. Pressure profile in a cross-section of "unwrapped" single-lobe pump stator 63

Figure 5.30. Pressure profile in a cross-section of single-lobe pump stator. 64

Figure 5.31. Path of rotor centre in 2D cross-section of single-lobe pump. 65

Figure 5.32. Cross-sections of single-lobe pump taken at various points along the length of the pump, shown relative to the global Y and Z axes. P_{rotor} is the rotor pitch...........66

Figure 5.33. Flowchart of iterative procedure used for determining equilibrium rotor position using 2D models. 67

Figure 5.34. Equilibrium position variations with pitch length. 72

Figure 5.35. Rotor/stator interference at the 0° and 90° rotor position for interference comparison models. 73

Figure 5.36. Points used for pointwise energy comparisons. 74

Figure 5.37. Contributions of distortional strain energy at point A as a function of p/d ratio with the rotor positioned at 0°. 75

Figure 5.38. Distortional strain energy density comparison at point A as a function of rotor position. 76

Figure 5.39. Distortional strain energy density comparison at point B as a function of rotor position. 76

Figure 5.40. Cross-sectional energy density integral with rotor at 0° position. 77

Figure 5.41. Planar energy comparison for 2D and 3D models for interference loading case. 78

Figure 5.42. Stator stiffness comparison at major diameter. 79

Figure 5.43. Planar energy comparison for modified rotor path model for interference loading case. 81

Figure 5.44. Contour plots of distortional strain energy density for (a) modified 2D model, (b) 3D model with p/d=1.85, and (c) 3D model with p/d=5.56 at rotor position 0°. (All units in mJ/mm³) 82

Figure 5.45. Contour plots of distortional strain energy density for (a) modified 2D model, (b) 3D model with p/d=1.85, and (c) 3D model with p/d=5.56 at rotor position 90°. (All units in mJ/mm³) 83

Figure 5.46. Strain energy density at point A with 0.31 MPa differential cavity pressure. 85

Figure 5.47. Strain energy density at point B with 0.31 MPa differential cavity pressure. 85

Figure 5.48. Planar energy comparison for 2D and 3D models for differential pressure loading case. 86

Figure 5.49. Contour plots of distortional strain energy density for (a) 2D model, (b) 3D model with p/d=1.85, and (c) 3D model with p/d=5.56 with rotor at 0° position, differential pressure 0.31 MPa. (All units in mJ/mm³) 87

Figure 5.50. Contour plots of distortional strain energy density for (a) 2D model, (b) 3D model with p/d=1.85, and (c) 3D model with p/d=5.56 with rotor at 90° position, differential pressure 0.31 MPa. (All units in mJ/mm³) 88

Figure 5.51. Planar strain energy comparison for short-pitch 3D model at differential pressures of 0.155 MPa and 0.31 MPa. 89

Figure 5.52. Relative contributions of pressure and interference energy as a function of applied differential pressure for 3D model with p/d=1.85. 90

Figure 5.53. Planar energy comparison for pressure, interference and combined load 3D analysis cases. 91

Figure 6.1. Dynamic response of elastomer to applied sinusoidal strain. 94

Figure 6.2. Vector diagram relating elastic, viscous, and complex moduli. 96

Figure 6.3. Sample variations in dynamic elastomer properties with temperature at an engineering strain amplitude of 12% and frequency of 20 Hz. 98

Figure 6.4. Sample variations in dynamic elastomer properties with frequency at an engineering strain amplitude of 12% and temperature of 30°C. 99

Figure 6.5. Sample variations in dynamic elastomer properties with strain amplitude at a frequency of 20 Hz and temperature of 30°C. 99

Figure 6.6. Sample variations in normal strain (ε_{yy}) in a single-lobe pump. 101

Figure 6.7. Element locations for strain histories shown in Figure 6.6. 101

Figure 6.8. Sample correlation between FEA results and Fourier series approximations to static stress and strain. 104

Figure 6.9. Sinusoids showing 20 degree phase shift at 1 and 2 Hz over a one-second interval. 105

Figure 6.10. Sample stress and strain descriptions (from Fourier series) before and after a phase shift of 20° was applied to the strain series. 106

Figure 6.11. Hysteresis loops from Fourier series and sinusoidal descriptions of shear stress/strain history over one cycle at a single point in a two-dimensional model. . 107

Figure 6.12. Integration points for a single 9-node element with 3 X 3 integration in global and natural coordinate systems and the associated weighting factors α_i and α_j. 110

Figure 7.1. Heat transfer conditions in a single-lobe pump. 113

Figure 7.2 Surface normal vector at inner profile of stator elastomer. 116

Figure 7.3 Description of out-of-plane normal component along inner profile of single-lobe stator. 117

Figure 7.4. Sample contour plots of temperature (top) and magnitude of total heat flux (bottom) in the elastomer from thermal finite element model showing suitability of structural mesh density. (Temperature units °C, Flux units mW/mm^2) 120

Figure 7.5. Flow situation that is analogous to cavity flow within PCPs and PDMs. 122

Figure 7.6. Circulating flow pattern within pipe that is analogous to flow in cavity. 123

Figure 7.7. Sample temperature distribution in stator with annular convection boundary condition on housing outside diameter. (Units in °C) 127

Figure 7.8. Sample temperature distribution in stator with insulated boundary condition on housing outside diameter and hysteresis heat input distribution used in Figure 7.7. (Units in °C) 127

Figure 7.9 Sample temperature distribution in stator with friction heat input for insulated boundary condition on housing outside diameter and hysteresis heat input distribution used in Figure 7.7. (Units in °C) 128

Figure 8.1. Temperature distributions in stator elastomer resulting from (a) interference loading at ambient temperature (20.0°C) and (b) interference loading at temperature profile shown in (a). 130

Figure 8.2. Progression of estimated peak elastomer temperature through successive iterations. 132

Figure 8.3. Iterative solution strategy flowchart (also presented as Figure 4.1). 133

Figure 8.4. Comparison of convergence criteria for thermomechanical analysis of sample single-lobe pump. 135

Figure 8.5. Convergence pattern for sample single-lobe thermomechanical analysis. 136

Figure 8.6. Sample converging and diverging thermomechanical analyses. 138

Figure 8.7. Sample temperature profiles through elastomer thickness from 1st, 3rd, and 9th (final) iterations of a thermomechanical analysis with convective boundary condition at housing outside diameter. 139

Figure 8.8. Relationship between radial rotor/stator interference and peak elastomer temperature for sample thermomechanical analysis of single-lobe pump with temperature-insensitive material properties. 141

Figure 8.9. Convergence optimisation routine flowchart. 142

Figure 8.10. Convergence pattern for optimised and non-optimised sample thermomechanical analyses of single-lobe pump with temperature-insensitive material properties. 144

Figure 9.1. Setup for verification testing. 148

Figure 9.2. Cross-sectional thermocouple distribution. Thermocouples 1 to 10 and 21 were primary thermocouples; the remainder were redundant. 149

Figure 9.3. Photograph of thermocouple hole in stator cross-section. 150

Figure 9.4. Axial thermocouple distribution showing hole locations in plan view. 150

Figure 9.5. Photograph of stator showing thermocouples (along pump length) and uniaxial hoop strain gauge (at right) 151

Figure 9.6. Photograph of insulated test stator 152

Figure 9.7. Position of strain gauge on housing outside diameter. 153

Figure 9.8. Elastomer and outlet fluid temperature readings for rotor 54, 400 RPM; pump speed was increased from rest to 400 RPM at t=400 seconds. 154

Figure 9.9. Orientation of thermocouple holes relative to direction of rotor rotation 156

Figure 9.10. Test results showing relationship between pump speed and peak elastomer temperature change for four rotors. 157

Figure 9.11. Test results showing relationship between nominal minor interference and peak elastomer temperature change at four speeds. 158

Figure 9.12 Test results showing relationship between radial minor interference predicted by 3D model and peak elastomer temperature change at four speeds 159

Figure 9.13. Stabilised elastomer temperature profiles for rotor 54 at 300 RPM 160

Figure 9.14. Stabilised temperature profile through thickest section of elastomer for rotor 54 at four speeds 161

Figure 9.15. Stabilised temperature profile through thickest section of elastomer for rotor 54 at four speeds, normalised to peak temperature at each speed 162

Figure 9.16. Stabilised temperature profile through thickest section of elastomer at 300 RPM for four rotors. 163

Figure 9.17. Stabilised temperature profile through thickest section of elastomer at 300 RPM for four rotors, normalised to peak temperature for each rotor. 163

Figure 9.18. Comparison of peak predicted and measured temperature increases in the stator elastomer 165

Figure 9.19. Errors in predicted temperature increase showing weak correlation between pump speed and error. 166

Figure 9.20 Errors in predicted temperature increase as a function of rotor number showing a strong correlation between error and rotor number. 167

Figure 9.21. Error in peak temperature prediction as a function of rotor/stator interference..... 168

Figure 9.22. Predicted peak temperature increase as a function of pump speed. 170

Figure 9.23. Trend in predicted temperature increase with pump speed, normalised to 400 RPM. 170

Figure 9.24. Comparison of predicted and actual trends in peak temperature increase with interference. 172

Figure 9.25. Comparison of predicted and measured temperature profiles through elastomer thickness at minor seal. 173

Figure 9.26 Comparison of normalised predicted and measured temperature profiles through elastomer thickness at minor seal. 174

LIST OF TABLES

Table 5.1. Comparison analysis cases. 71

Table 5.2. Errors in average strain energy for 2D approximations to 3D models. 84

Table 9.1. Test program summary. 147

Table 9.2. Comparison of peak stabilised elastomer temperature increases obtained from testing and modelling. 165

Table 9.3. Range of error in predicted temperature increase for four speeds. 167

Table 9.4. Range of error in predicted temperature increase for rotors. 168

Table 9.5. Comparison of measured and predicted hoop strains at gauge on outside diameter of housing at major diameter. 175

Table 9.6. Thermomechanical analyses conducted for error identification. All analyses were conducted at 400 RPM. 179

Table 9.7. Results of thermomechanical analyses conducted for error identification. 180

LIST OF VARIABLES

Single-Lobe Pump Geometry Description

P_{rotor}	rotor pitch length (mm)
P_{stator}	stator pitch length (mm)
N_{rotor}	number of rotor lobes
N_{stator}	number of stator lobes
D_{rotor}^{minor}	rotor minor diameter (mm)
D_{rotor}^{major}	rotor major diameter (mm)
D_{stator}^{minor}	stator minor diameter (mm)
D_{stator}^{major}	stator major diameter (mm)
X, Y, Z	global cartesian coordinate axes
θ	rotor position (°)
e_{actual}	operating eccentricity of single lobe pump (mm)
e_{rotor}	eccentricity of single-lobe pump rotor (mm)
e_{3D}	eccentricity offset (mm)
L_{major}	length of major axis of ellipse defining single-lobe rotor path (mm)
L_{minor}	length of minor axis of ellipse defining single-lobe rotor path (mm)

Structural Modelling

u_i^Q	is the displacement of node Q in direction i (mm)
U	strain energy density (J/m^3)
U''	distortional strain energy density (J/m^3)
U_{ij}''	contribution of stress and strain components in direction ij to distortional strain energy density (J/m^3)
C_i	constants in Mooney-Rivlin description
I_1, I_2, I_3	invariants of the Cauchy-Green deformation tensor
κ	bulk modulus (MPa)
ε_{ij}	components of true (Hencky) strain tensor
ε_{mean}	mean true strain
τ_{ij}	components of Cauchy stress tensor (MPa)

τ_{ij}^{dev}	deviatoric components of Cauchy stress tensor (MPa)
τ_{mean}	mean Cauchy stress (MPa)
α	thermal expansion coefficient (1/°C)
$T_{elastomer}$	operating temperature of elastomer (°C)
T_{ref}	material reference temperature (°C)
$T_{ref(elastomer)}$	modified elastomer reference temperature for elastomer swelling loads (°C)
ΔT_{swell}	equivalent temperature change for applying elastomer swelling loads (°C)
$swell$	volumetric swell (%)
μ	coefficient of friction
L_{min}	minimum 3D structural model length (mm)
δ_{ij}	Kronecker delta (equals 1 if $i=j$, equals 0 if $i \neq j$)

Heat Generation Modelling

δ	elastomer viscous loss angle (°)
$\tan \delta$	elastomer loss tangent
E, E'	elastic (storage) tensile modulus (MPa)
E''	viscous (loss) tensile modulus (MPa)
E^*	complex tensile modulus (MPa)
D^*	complex tensile compliance (1/MPa)
G'	elastic shear modulus (MPa)
G''	viscous shear modulus (MPa)
G^*	complex shear modulus (MPa)
J^*	complex shear compliance (1/MPa)
τ_{ij}^{static}	component ij of the static deviatoric stress (MPa)
M	highest order of Fourier sine or cosine series
t	time (s)
T	period of rotational cycle (s)
η	nondimensional time variable
${}^{ij}E^{cos}{}_{k}$, ${}^{ij}E^{sin}{}_{k}$	k^{th}-order cosine and sine Fourier series coefficients for component ij of the static total strain

${}^{ij}_{static}S^{\cos}_{m}$, ${}^{ij}_{static}S^{\sin}_{m}$	m^{th}-order cosine and sine Fourier series coefficients for component *ij* of the static deviatoric stress
α_i *and* α_j	weighting factors for element integration
J	Jacobian matrix
r *and* s	natural coordinate directions in a planar finite element
h_i	i^{th} shape function of a finite element
Y_i, Z_i	Y and Z coordinates of node i (mm)
E^{total}	total heat input for an element (J)
$E^{density}_{ij}$	heat input density at integration point *ij* in a planar finite element (J/mm^3)
$A_{element}$	planar element area (mm^2)

Thermal Modelling

k_e	stator elastomer thermal conductivity (W/m·K)
k_h	stator housing (steel) thermal conductivity (W/m·K)
$E_{friction}$	frictional heat input at a point on the inner profile of the stator elastomer (J)
$F_{friction}$	frictional force (N)
Δd^{n}_{app}	distance the rotor/stator contact patch travels in the n^{th} substep (mm)
θ_n	rotor position at the n^{th} substep (°)

Coupled Modelling

ΔT_{max}	maximum temperature increase along a radial line through the thickest part of the elastomer (°C)
A	scalar (coefficient) for power-law interference/temperature description
n	exponent for power-law interference/temperature description
B	scalar describing the ratio of peak temperature to average temperature through thickest section of elastomer
C	scalar relating the thermal strain to the rotor/stator interference at the minor seal

1 INTRODUCTION

Progressing Cavity Pumps (PCPs) and Positive Displacement Motors (PDMs) are used extensively in downhole oilfield production and drilling operations. These positive-displacement machines are derived from the design of the Moineau pump that was originally patented in the 1930's. Each consists of a rotating steel rotor and a stationary elastomeric stator which mesh helically to form a series of sealed cavities which move axially as the rotor is rotated. PCPs provide excellent capability for pumping fluids with high sand content, high viscosity, and entrained gas. PDMs provide an effective means of generating downhole shaft power for drilling using fluid pressure applied from the surface.

This study has been undertaken to develop a series of tools for analysing stator performance under representative loading conditions. The primary goal of the research is to develop a coupled thermo-mechanical solution strategy for obtaining the temperature distribution in the stator in its stabilised downhole operating mode. The realisation of this goal requires structural and steady-state thermal finite element modelling and quantification of the viscoelastic response of the stator elastomer to cyclic structural loads. A bench-scale testing program was completed to validate modelling results. It is expected that the modelling strategies developed through the study will prove valuable in PCP and PDM design optimisation and failure prevention.

Specific innovations made through the course of this research are:

- Development of a strategy for modelling structural behaviour of PCPs and PDMs with two-dimensional finite element models under loads representative of downhole operating environments. This included the creation of a method of accounting for three-dimensional deformation effects using two-dimensional models in the context of heat generation within the elastomer;

- Modification and implementation of an existing strategy for quantifying hysteresis heat generation in elastomeric components to PCPs and PDMs;
- Use of a pseudo-steady-state analysis approach to reduce solution time for a dynamic viscoelastic material problem; and
- Development and optimisation of an iterative solution strategy for determining the stabilised thermal and structural operating conditions in the stator elastomer of PCPs and PDMs.

Chapter 2 provides background information on the operation of PCPs and PDMs specifically required for a full comprehension of the discussion presented herein. A review of literature relevant to the problem at hand is presented in Chapter 3. In Chapter 4, the iterative thermomechanical modelling strategy developed for obtaining the stabilised operating temperature distribution in the stator is introduced. Structural modelling, heat generation modelling, and thermal modelling strategies are described in detail in Chapters 5, 6, and 7 respectively. A complete description of the thermomechanical solution method is presented in Chapter 8. Verification testing and comparisons between modelling and testing results are discussed in Chapter 9. Finally, Chapter 10 lists a series of conclusions and recommendations for future work related to this study.

2 BACKGROUND

A basic comprehension of the operating principles and operating conditions of Progressing Cavity Pumps (PCPs) and Positive Displacement Motors (PDMs) is imperative for understanding the modelling strategy proposed herein. Discussions presented in Chapters 4 through 8 assume that the reader has this basic understanding.

2.1 General Principles of PCP and PDM Operation

The basic operating principle of PCPs and PDMs is the same. Both designs stem from the Moineau pump, a device developed in the 1930s by Renée Moineau.[1,2] Each has two components, a stator and a rotor. The stator consists of a shaped elastomeric core surrounded by a steel housing. The rotor is usually fabricated from chrome-coated steel and rotates within the stator cavity. Compatible rotor and stator geometries mesh with one another. Figure 2.1 shows sample conventional single-lobe rotors and stators. PCPs may be up to 13.7 cm (5.5") in diameter and as long as 15 m. PDMs may have diameters of up to 33 cm (12-7/8") and can exceed 5 m in length.

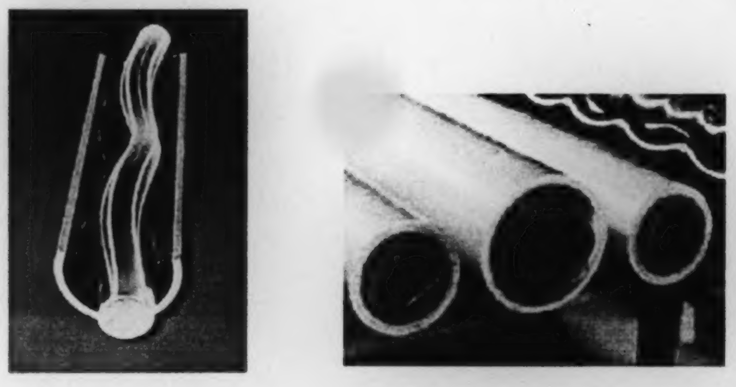

Figure 2.1. Photographs of single-lobe pump rotor with sectioned stator (left) and single-lobe stators (right).

2.1.1 Cross-sectional geometry

Cross-sections of mating rotor and stator components taken perpendicular to the longitudinal axis of PCPs and PDMs are normally based on the geometry of mating hypocycloids. A hypocycloid is the path traced by a point on the outside diameter of a small circle as it rolls inside of a larger circle. Example hypocycloids are shown in Figure 2.2. Each hypocycloid has a finite number of tips (or *lobes*), defined by the integer ratio of the diameters of the large and small circles. Figure 2.2(a) shows a two-lobe hypocycloid, which is formed by rolling a small circle inside a larger circle of twice the diameter. A fixed point on the small circle follows a linear path as the smaller circle rolls inside the larger circle. In Figure 2.2(b), the ratio of diameters of the large to small circles is 3:1. When the small circle rolls inside the larger circle, the fixed point on the small circle follows a path that creates a three-lobe hypocycloid. Similarly, the 4:1 diameter ratio in Figure 2.2(c) generates a four-lobe hypocycloid.

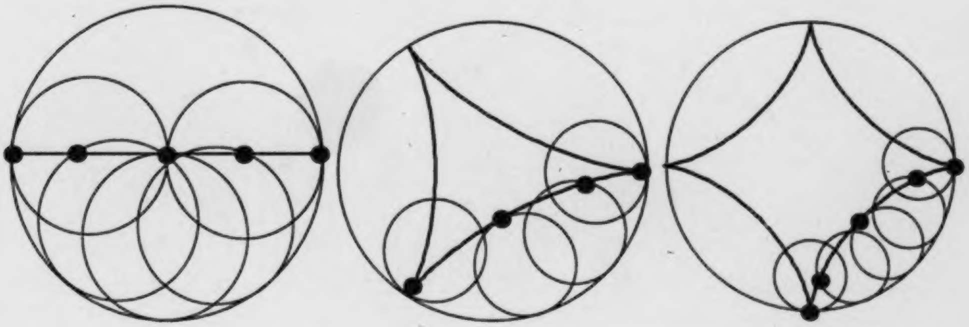
(a) (b) (c)

Figure 2.2. Sample two, three, and four-lobe hypocycloids.

The profile of a rotor or stator is generated from hypocycloid geometries by adding a radius R to the point on the circle that traces the hypocycloid path. For example, the two, three and four-lobe hypocycloid paths shown in Figure 2.2 generate profiles like those shown in Figure 2.3. The one-lobe hypocycloid path is a stationary point, making the profile a circle of radius R.

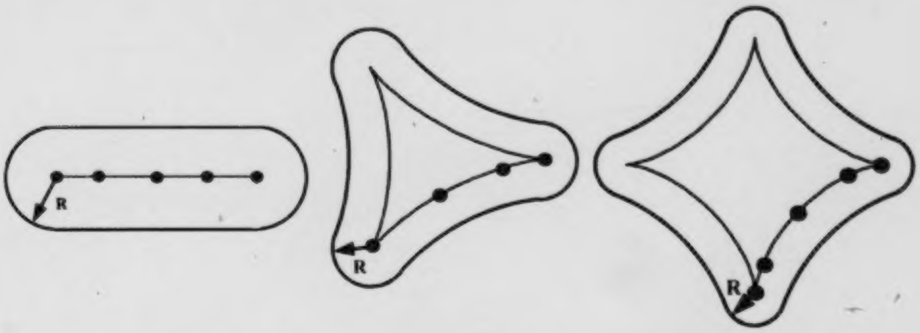

Figure 2.3. Two, three, and four-lobe profiles generated with hypocycloid paths.

The profiles generated by hypocycloids with consecutive lobe numbers (i.e., 1 and 2, 2 and 3, etc.) and equal point radii are compatible and form the geometrical basis for conventional PCPs and PDMs. The outer profile of the rotor is based on the hypocycloid with fewer lobes and the inner profile of the stator elastomer is based on the mating hypocycloid.

Figure 2.4 shows 1:2 and 2:3 lobe profiles with the rotor at a number of different positions in its rotational path within the stator. If machining tolerances are ignored, the rotor and stator geometry at all cross-sections in a stationary PCP or PDM is identical with the exception of the orientation of the rotor with respect to the stator.

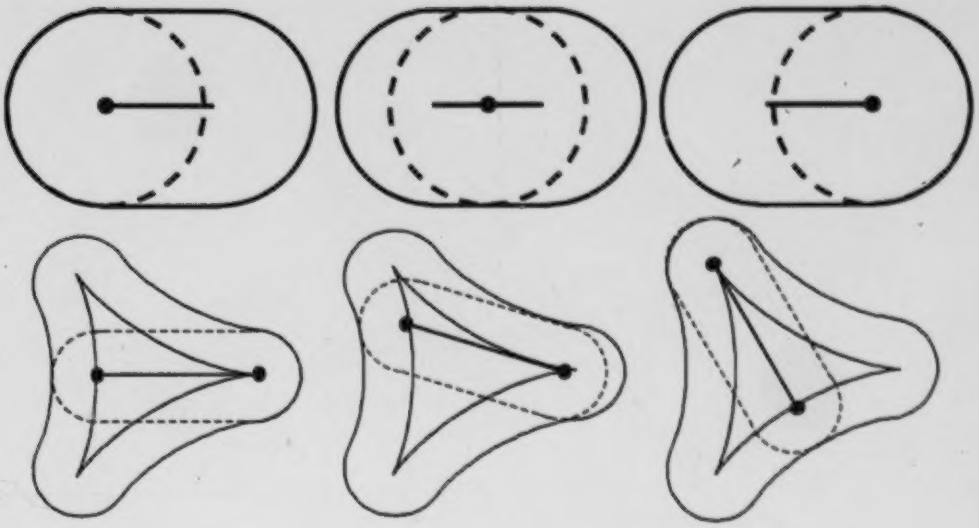

Figure 2.4 Rotor motion in stator profile for 1:2 lobe (top) and 2:3 lobe (bottom) geometries with compatible hypocycloids.

2.1.2 Axial geometry

The axial geometry of rotors and stators is helical in shape and thus may be described using a helical pitch length (frequently referred to as the pitch length). The rotor pitch length is shorter than the stator pitch length by a factor equal to the ratio of stator lobes to rotor lobes. The helical geometry and differing pitch lengths of the rotor and stator create a series of constant-volume cavities that move along the length of the stator as the rotor turns. These cavities carry fluid through the pump or motor.

The rotor and stator geometries are typically designed to interfere with one another during operation to generate a fluid seal between bordering cavities. This interference is accomplished by increasing the size of the rotor geometry from the hypocycloid definition in a manner that creates interference along the boundaries of all adjacent fluid cavities. The actual seal capacity is tied to a number of factors including the interference.

2.2 Single-lobe Progressing Cavity Pumps

While the findings presented in this study are applicable to any PCP or PDM that operates on the principles of the Moineau pump, the 1:2 lobe geometry (also called the single-lobe geometry) is used extensively in this work as an example. Further detail and nomenclature specific to the operating principles of single-lobe PCPs is provided in the following paragraphs.

The geometries of a compatible one-lobe rotor and two-lobe stator are shown from an end-view perspective in Figure 2.5. Note that the centre of the end section of the rotor is not coincident with the centre of mass of the rotor due to its helical nature. The cross-sectional rotor diameter is called the *rotor minor diameter*. The total size of the visible axial profile is defined by the radius of the helix that defines the rotor shape, which is equal to the distance between the centre of the cross-sectional geometry and the centre of mass. The diameter of the visible rotor profile is called the *rotor major diameter*. From the same viewpoint, the *stator minor diameter* is equal to the width of the cavity in any cross-section and the *stator major diameter* is the distance from one end of the cavity to the other. The orientation of the stator cross-section changes along the length of the pump to form a helix. Unlike the rotor, the centre of the stator cross-section remains the same in each cross-section. From an end view perspective, the visible inner profile through the stator is a circle equal to the stator minor diameter. The dashed "axial profile" line in Figure 2.5 represents the profile of the major diameter as it rotates along the length of the pump.

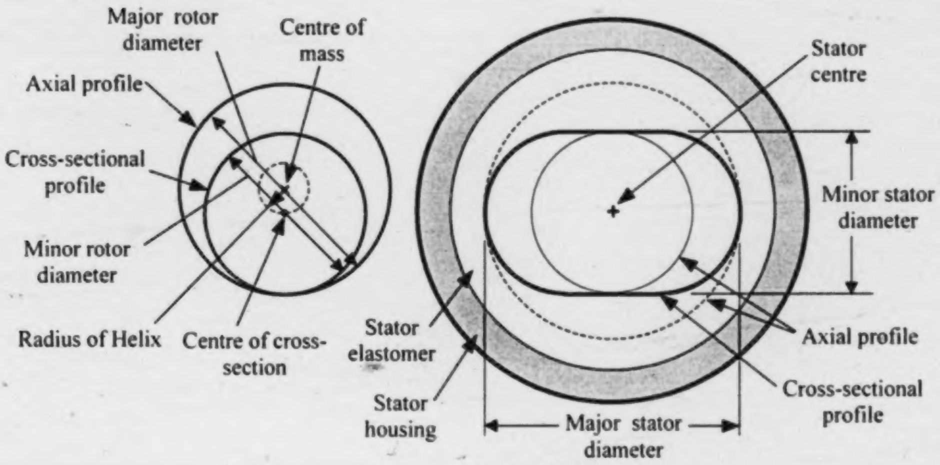

Figure 2.5. End views of rotor (left) and stator (right) components of a conventional single-lobe pump with associated nomenclature.

When the rotor moves within the stator, the rotor and stator are oriented in the manner shown in Figure 2.6. As the rotor rotates (shown clockwise in the figure), the centre of mass of the rotor rotates about the centre of the stator in the opposite direction along a circular path with radius *e*. The combination of these motions causes the rotor cross-section to translate within the stator cross-section.

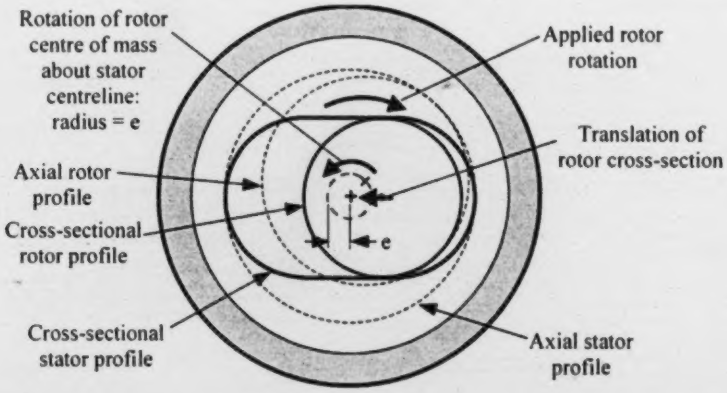
Rotation of rotor centre of mass about stator centreline: radius = e
Applied rotor rotation
Translation of rotor cross-section
Axial rotor profile
Cross-sectional rotor profile
e
Cross-sectional stator profile
Axial stator profile

Figure 2.6. End view of pump showing interaction between rotor and stator.

If the rotor and stator cross-sections were perfectly compatible hypocycloids, the point representing the rotor hypocycloid would translate along the line that defines the two-lobe hypocycloid of the stator. However, the interference fit between the rotor and stator means that it is incorrect to assume that the motion of the rotor cross-section within the stator is purely lateral. Discussions in Chapter 5 show that the actual path of the rotor in the cross-section in the presence of interference is elliptical in shape.

In a single-lobe pump, the seals formed between the rotor and the stator are frequently characterised according to their location in the stator cross-section. Figure 2.7 defines these seals graphically. The *minor seal* is created by the interaction between the rotor and stator cross-sections along the straight segment of the stator profile. The rotor/stator interference at the centre of the straight segment is referred to as the *minor interference* of the pump. The *major seal* is created by the interaction between rotor and stator cross-sections at the end of the oblong stator profile. The interference at this point is referred to as the *major interference*.

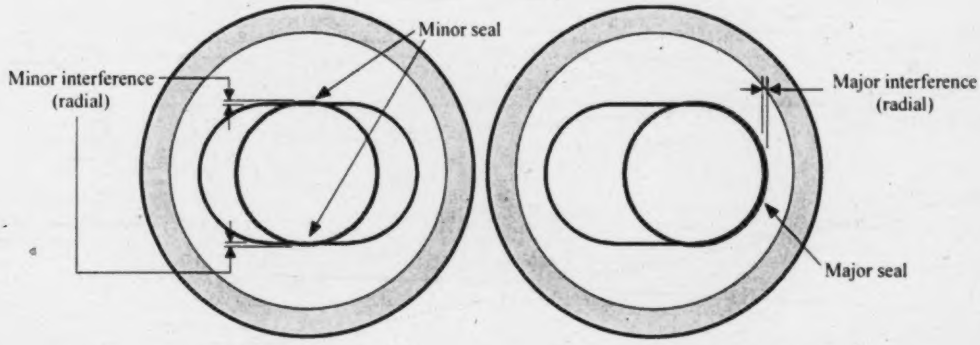

Figure 2.7. Major and minor seal definitions in a single-lobe progressing cavity pump.

The orientation of the rotor with respect to the stator in any one cross-section changes with time as a Moineau pump operates. The different axial pitch lengths of the rotor and stator also result in different rotor orientations along the length of the pump at any one point in time. For a single-lobe pump at rest, the rotor orientation with respect to the stator is periodic with the rotor pitch length. Figure 2.8 shows that if the rotor contacts the centre of the minor seal at an axial position X, the rotor will contact the centre of the major seal at an axial position ($X+½*P_{rotor}$) and will again contact the centre of the minor seal at an axial position ($X+P_{rotor}$). This represents one full rotor pitch, which is equal to exactly one-half stator pitch for a single-lobe pump as indicated previously. The open and closed dots on the stator profile in Figure 2.8 show the orientation of the profile with respect to the global Y and Z axes.

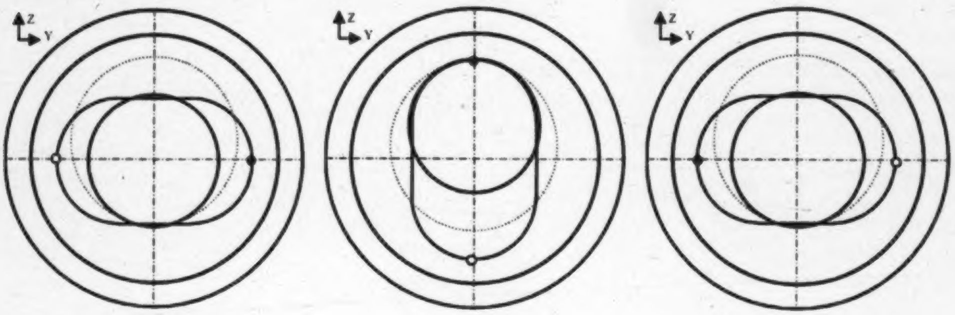

(a) Axial Position X (b) Axial Position ($X + ½*P_{rotor}$) (c) Axial Position ($X + P_{rotor}$)

Figure 2.8. Relative positions of rotor and stator cross-sections at different axial positions.

The structural modelling strategies described in Chapter 5 make use of the periodic nature of the rotor/stator orientation to optimise analysis time. A two-dimensional (2D) modelling strategy uses a number of static analyses to emulate the motion of the rotor within the stator in one cross-section. This series of static analyses also represents loading variations along the length of the pump at any one time. Similarly, three-dimensional (3D) modelling results at one point in time can be used to indicate the variations in response in one cross-section as the pump operates.

2.3 Applications of PCPs and PDMs

Typical downhole PCPs are placed at or near the production perforations in oil or water wells to pump production fluid to surface using shaft power. The pump lifts fluid against a differential pressure that is defined by the pressure in the reservoir, the height of the fluid columns above the pump inlet and discharge, and any flow losses associated with moving the fluid to surface. A typical installation is shown in Figure 2.9(a). Fluid is drawn from the reservoir at a flow rate Q that is defined by the speed, size, lobe configuration, and efficiency of the pump. Pumps typically rotate at speeds of between 100 RPM and 500 RPM and use 1:2 or 2:3 lobe geometry configurations. The pump is able to develop and sustain pressure through the interference fit between the rotor and stator. Depending on the geographical location and depth of the well, the temperature of the downhole fluid may be as high as 125 °C. Hysteretic heating of the elastomer causes the stator temperature to increase above that of the production fluid. Elastomer design and selection must be done with care because production fluids may not be compatible with the elastomer and may cause the stator to swell, further increasing the rotor/stator interference.

PDMs are used to provide shaft power to bits used for drilling oil wells. A sample PDM installation is shown in Figure 2.9(b). Applied fluid pressure at the motor inlet drives drilling fluid through the stator at flow rate Q, causing the rotor and drill bit to spin. PDM geometries may use lobe configurations ranging from 1:2 to 10:11. Stator loads include interference, swelling, and temperature increases due to hysteresis heating.

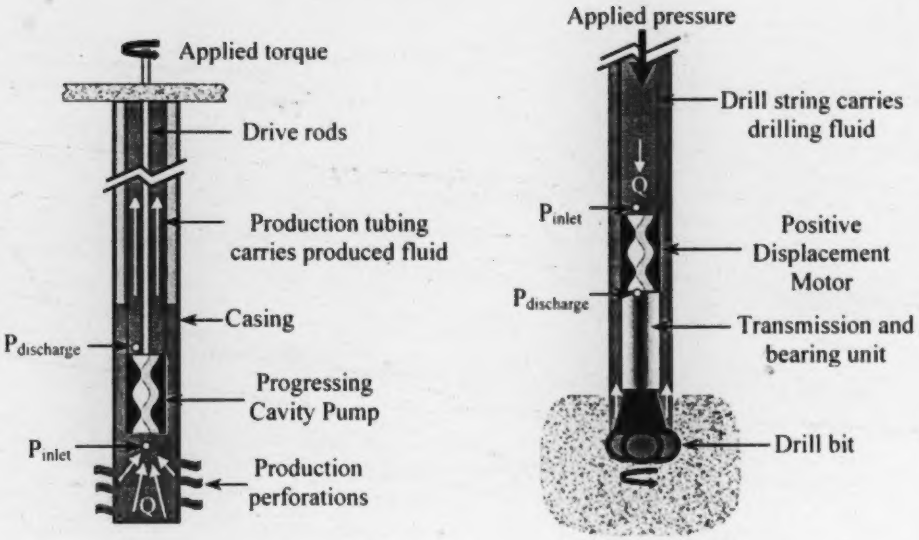

(a) PCP installation (b) PDM installation

Figure 2.9. PCP and PDM operating configurations.

The lobe configurations used in PCP and PDM applications range from 1:2 to 10:11. While the single-lobe configuration is used to illustrate the analysis strategies in the chapters that follow, the strategy may be easily adapted for use with higher lobe configurations.

3 LITERATURE REVIEW

This study focuses on structural, thermal, and heat generation modelling of the stator elastomer in Progressing Cavity Pumps (PCPs) and Positive Displacement Motors (PDMs). Literature obtained through the course of the investigation pertains to:

- static and dynamic elastomer material response, including elastomer hysteresis heat generation;
- finite element modelling of elastomeric components, including elastomer-specific material models and element formulations;
- thermomechanical modelling strategies; and
- modelling of PCPs and PDMs.

3.1 Response and Modelling of Elastomers

Characteristics of elastomers specifically required for this study include descriptions of typical static and dynamic responses. While descriptions of elastomer properties are plentiful, many investigations focus on the effects of elastomer formulations on material properties as attempts are made to optimise material response for specific applications. Effects of fillers and other additives to elastomer compounds are outside of the scope of this investigation.

Static structural material properties of elastomers are required for the finite element modelling conducted through the course of this investigation. The nature of static elastomer material properties in infinitesimal strain and finite strain regimes is summarised by Gent [3], among others. The use of hyperelastic formulations such as the Mooney-Rivlin and Ogden models to describe static elastomer response is explained by Charlton, Yang, and Teh.[4] Section 5.1 contains descriptions of the structural material descriptions used for this investigation. Dynamic structural material properties are required when analysis of dynamically loaded systems containing elastomeric components is to be conducted. Kramer and Ferry [5] provide a clear description of the viscoelastic response of typical elastomers, as do Lamba and Meinecke.[6] The dynamic material property model used for this investigation is described in Section 6.2.

Heat generation within elastomers has been a subject of great interest because of its implications for component design. Cyclic loading of an elastomeric part causes heat generation within the material because of the viscoelastic response of the material. Such heat generation causes an increase in component temperature that may affect the structural response significantly. Basic descriptions of the nature of heat generation in elastomers have been prepared by Medalia [7] and Reed [8,9], among others.

Much work has been documented on the use of finite element modelling techniques to characterise the behaviour of elastomeric materials. Mackerle[10] presents a comprehensive bibliography pertaining to finite element modelling of elastomers. While not providing a critical review of the cited work, the bibliography does provide an extensive list of references pertaining to elastomer finite element formulations, material descriptions, finite element studies of particular components, and other related information. The finite element formulations used for this investigation are consistent with those available in the finite element software used for the task, ADINA 7.3. These formulations are identified in Chapters 5 and 7 and are described in detail by Bathe.[11]

3.2 Thermomechanical Modelling of Elastomeric Components

Thermomechanical studies incorporate structural and thermal analyses of the same component. This is typically done when there is some degree of coupling between the structural and thermal responses that must be modelled to accurately portray component behaviour. Thermomechanical analyses of elastomeric components are common because the viscoelastic response of the elastomeric material generates heat and a subsequent temperature increase in the component. The elevated operating temperature may affect the structural material response significantly. For typical nitrile rubbers, increases in elastomer temperature result in a decrease in the elastic stiffness of the elastomer and may also increase the dynamic (viscous) loss coefficient. Relevant investigations of previous thermomechanical modelling pertain to components such as aircraft and automobile tires [12,13], tank track pads[14], dampers and bearings in helicopter rotors,[15] and antivibration mounts.[16] One published study involving thermomechanical modelling of PDMs has also been obtained.[17] In each study, the primary mechanism for elevated elastomer temperature is heating due to viscous losses within the elastomer as the component is cyclically loaded.

The most common method of calculating the viscous heating energy in an elastomeric component subject to cyclic loads is to use the predicted structural response of the component to construct a representative stress/strain hysteresis loop. The area within the loop at a given point in the material represents the heat energy generated at that point through the course of one load cycle. A variety of strategies have been used to construct the hysteresis loop, many making use of finite element methods. A simple method of quantifying viscous (hysteresis) energy over one load cycle involves estimating the area within the hysteresis loop by assuming that the stress and strain quantities vary sinusoidally as the component undergoes cyclic loading even if the load variations are not sinusoidal with time. If a linear viscoelastic material model is used in conjunction with this sinusoidal loading assumption, the hysteresis energy simplifies to the calculation of the area within an ellipse. This approach is used by Sridhar et al.[14], Sae-oui et al.[16], and Delpassand.[17] Charlton and Teh[13] model a non-linear viscoelastic material using a non-linear elastic material description in conjunction with dynamic properties that are dependent on strain energy. McAllen et al.[12] provide an alternate method of quantifying stress and strain history that may be used to account for non-sinusoidal load variations such as those seen in tires under the assumption of linear viscoelasticity. Further description of this method is presented in Section 6.3.

After quantifying the heat generation, the component temperature may be found by analysing the thermal response. This is typically done using steady-state or transient thermal finite element analyses, depending on the application.

The complexity of the overall thermomechanical solution process depends on the degree of coupling between thermal and structural models and the sensitivity of the material properties to temperature changes. McAllen et al.[12] conduct a structural analysis, quantify the heat generated, and then conduct a thermal analysis to determine the temperature distribution in an aircraft tire. Charlton and Teh[13], among others, use an iterative procedure to account for the effect of the temperature increase on the structural response of the elastomer. In PCPs and PDMs, the structural and thermal responses are coupled through both temperature-sensitive material response and temperature-sensitivity of the rotor/stator interference. The iterative thermomechanical solution procedure proposed for this modelling work is introduced in Chapter 4 and explained in detail in Chapter 8.

Delpassand[17] has performed the only documented investigation known to the author that is specific to positive displacement motors with the goal of predicting the temperature in the stator elastomer for design purposes. To obtain the temperature distribution, three-dimensional structural and thermal finite element models and a heat generation expression are combined in a thermomechanical solution procedure. This reference does not provide a complete description of the finite element modelling methods used. Structural loads modelled include uniform internal pressure, differential pressure between cavities, and rotor/stator interference. Rotor interference loads appear to be modelled using an initial strain condition rather than contact elements, implying that it is unlikely that the motion of the rotor within the stator is considered. Structural modelling accounts for inward thermal expansion of the stator elastomer profile and material property changes due to temperature increases in the stator. The importance of the structural response of the stator housing under internal pressure loading is ignored. Heat generation calculations are based on the assumption of a sinusoidal strain loading pattern and a linear viscoelastic material, but details of the procedure used to quantify this heat generation and apply it to thermal models are omitted from the discussion. Thermal modelling appears to have been done using a steady-state heat transfer assumption. A constant-temperature boundary condition is used to model convection at the inner stator profile, while constant-temperature and natural convection conditions are used to model convection in different operating modes at the outside diameter. No description of the efficiency of the iterative procedure is provided. Numerical results are compared against the results of a testing program. Estimates of the peak temperature in the stator are obtained through temperature measurements at the elastomer/housing interface and a simple conduction model. Delpassand[17] concludes that test results show an acceptable correlation with experimental data. No elaboration is given in the paper.

4 INTRODUCTION TO MODELLING STRATEGY

The primary goal of this investigation is to develop a modelling strategy for predicting the stabilised response of PCPs and PDMs in downhole operating environments. Pertinent results include the stress and strain fields and the operating temperature in the stator elastomer and the contact stress between the rotor and stator. Such results may be used for predicting fatigue failures and elastomer material property degradation and for determining optimal design configurations for specific scenarios.

In order to understand the downhole operating conditions in a PCP or PDM, a stabilised thermo-mechanical solution is required. In other words, the thermal and structural responses must be consistent with one another. The primary links between structural and thermal responses for this application exist in the form of viscous heat generation in the elastomer from cyclic structural loading, volumetric expansion of the elastomer from thermal expansion, and sensitivity of the structural elastomer material properties to temperature. The interdependence of structural and thermal responses necessitates an iterative solution strategy that provides a means of linking the structural and thermal problems while encouraging convergence to the stabilised operating point.

A finite element analysis (FEA) modelling strategy is used to model the structural and thermal responses of PCP and PDM stators. An analytical formulation is presented for quantifying the viscoelastic heat generation terms required to link the structural and thermal models. Figure 4.1 shows a flowchart that outlines the proposed iterative strategy for obtaining the stabilised temperature and loading distributions in a pump or motor.

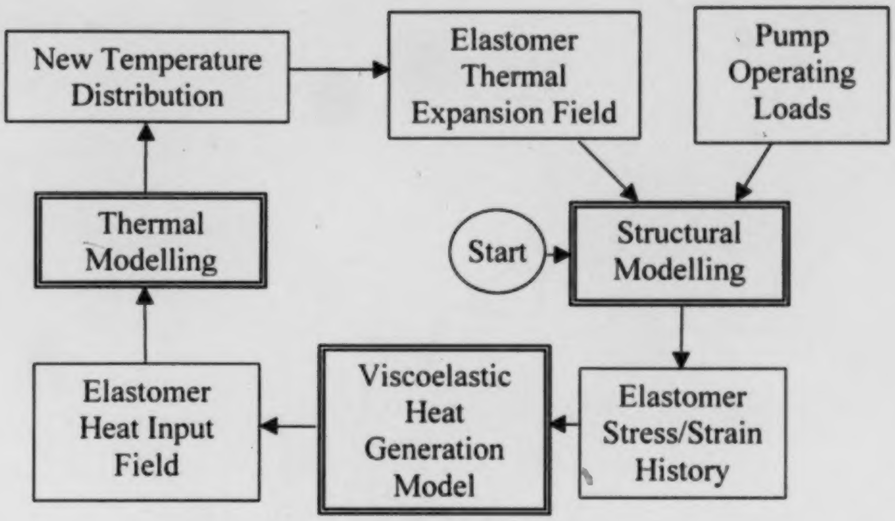
New Temperature Distribution
Elastomer Thermal Expansion Field
Pump Operating Loads
Thermal Modelling
Start
Structural Modelling
Elastomer Heat Input Field
Viscoelastic Heat Generation Model
Elastomer Stress/Strain History

Figure 4.1. Iterative thermomechanical solution strategy.

The iterative loop begins with a structural finite element analysis of the stator through a full rotor operating cycle under representative loads with the elastomer at the temperature of the produced fluid. The structural analysis results in a description of the stator loading history that may be used to calculate viscous heat losses within the elastomer using a viscoelastic heat generation model. The resulting elastomer heat input field is used in conjunction with a thermal finite element model to determine an average temperature distribution in the elastomer. This temperature distribution is then compared with the assumed temperature distribution as a convergence criterion for the procedure. If the temperature distributions differ, the newest temperature distribution is used as the applied temperature field for the structural analysis in the subsequent iteration. This iterative process continues until the temperature distribution remains the same from one iteration to the next. Strategies for the structural, thermal, and heat generation modelling modules shown in Figure 4.1 are described in detail in Chapters 5, 6, and 7 respectively. Detailed discussion of the coupled modelling strategy and related optimisation follows in Chapter 8.

5 STRUCTURAL MODELLING

Structural modelling is required in order to obtain an accurate representation of the stress and strain distribution within the stator as the pump or motor operates. Structural models provide a means of understanding the sensitivity of the stator to design changes and to variations in applied operating loads. The contribution of static structural modelling to the overall thermo-mechanical solution strategy is critical as it provides a method of quantifying the cyclic stress and strain response of the stator.

The following key factors influence the validity of the structural models:

- description of the elastomer material;
- suitability of the finite element formulations used for modelling;
- loading representative of that experienced in field operation; and
- boundary conditions applied to the various components of the model.

The two-dimensional (2D) structural modelling approach described in Section 5.3 provides an approximation to the response of the complex three-dimensional pump and motor geometries. A three-dimensional (3D) modelling strategy is described in Section 5.4. Results of selected three-dimensional analyses are used to calibrate two-dimensional models (Section 5.6). Version 7.3 of the ADINA finite element analysis software[18] is used for all finite element modelling.

5.1 Material Considerations (Structural Models)

Elastomers are frequently used in component design because of their ability to recover from large deformations. The approach used to describe elastomer material behaviour in this investigation is compatible with large-strain finite element analyses and accommodates temperature-sensitive response characteristics. The model uses a linear material description in terms of true (Hencky) strain and Cauchy stress measures to approximate a hyperelastic material model.

5.1.1 Hyperelastic material models

The static stress-strain behaviour of elastomeric components is discussed in detail by Gent.[3] As shown in Figure 5.1[19], this behaviour can be nonlinear, especially at high strains. The most common method of quantifying the structural response of elastomers is through one of a number of strain-energy functions that have been formulated that describe this behaviour in the context of the elongation and motion of cross-linked elastomer strands. Material models that use such strain energy functions to determine the stress state are termed *hyperelastic* models.

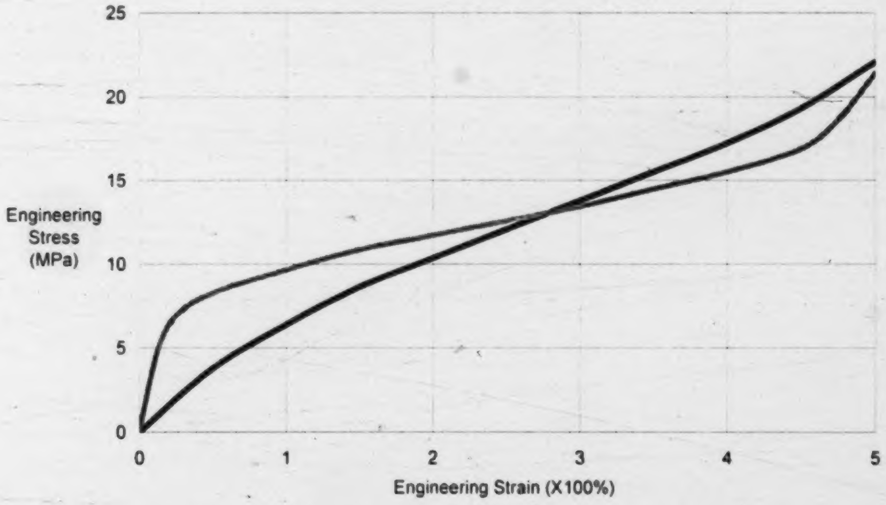

Figure 5.1 Sample uniaxial tension behaviour for two elastomers (adapted from Beatty and Studebaker[19]).

A commonly used strain-energy function for elastomers is called the Mooney-Rivlin function. For example, a first order Mooney-Rivlin function has the form

$$U = C_1(I_1 - 3) + C_2(I_2 - 3) \qquad [5.1]$$

where: U is the strain energy density;

C_1 and C_2 are constants; and

I_1 and I_2 are the first and second invariants of the Cauchy-Green deformation tensor.

Depending on the complexity of the material response and the strain range of interest, the number of coefficients used to describe the Mooney-Rivlin function usually ranges from two (first-order description) to nine (third-order description). Coefficients are typically found using shear, tensile, or biaxial test data and a least-squares curve fitting algorithm. Further description of the use of the Mooney-Rivlin function may be found in the literature.[4,11,20]

Equation 5.1 is based on the assumption that the third invariant of the Cauchy-Green deformation tensor is equal to unity, meaning the material description assumes incompressibility. However, elastomeric materials are slightly compressible. This compressibility may be incorporated into the material description by using a modified form of the Mooney-Rivlin expression and a set of reduced strain invariants, J_i $(i=1,2,3)$, which remove the incompressibility constraint imposed by setting I_3=1. The reduced invariants J_i are functions of the original strain invariants, I_i. The use of this method to account for compressibility is discussed by Bathe.[11]

While the Mooney-Rivlin hyperelastic elastomer description is well-suited to modelling the behaviour of the stator elastomer in this study, the finite element program in use is not equipped with hyperelastic material models that can be assigned temperature-sensitive responses or thermal expansion coefficients. The sensitivity of elastomer properties to changes in temperature and the nature of the applied temperature fields within the stator elastomer is critical to this investigation. As a result, a different formulation is required for use with ADINA 7.3.

5.1.2 Linear approximation to elastomer material response

In some instances, it becomes acceptable to make use of a linear stress-strain approximation to model the response of elastomers. Gent[3] indicates that a good approximation to the stress state in a component may be made using a linear material model for tensile engineering strains on the order of 25%. An appropriate linear approximation is used for all structural modelling in this study.

The selected linear material description is based on the hyperelastic material model at low strains. Given a material response curve in simple tension or pure shear, a Mooney-Rivlin model may be created using a curve fitting technique and its suitability checked against the material response curve. If the Mooney-Rivlin curve fit is acceptable, the slope of the curve at the origin provides an estimate of the small-strain elastic modulus (from tensile test) or shear modulus (from pure shear test) of the material. This modulus is used to relate the stress and strain quantities in the elastomer and represents a linear approximation to the material response.

The large-strain, large-displacement finite element analysis formulations used for modelling the structural response of PCPs and PDMs necessitate an understanding of the various stress and strain measures that are commonly used. In the case of small (infinitesimal) strains and deformations, engineering strain and engineering stress measures are used. Engineering strain is defined by the deformed length of a material element relative to the original length. Engineering stress is defined as the force per unit undeformed material area. However, when strains and deformations become large, the physical relevance of the original length and undeformed area in the strain and stress quantities is reduced. More appropriate measures such as the true (Hencky) strain and Cauchy stress may be used to characterise the strain and stress states in large-strain, large-deformation analyses. These measures account for changes in the geometry that are ignored in the case of infinitesimal strains. For instance, Cauchy stress refers to the force per unit deformed material area, which can be significantly different from the engineering stress if the area upon which the force acts has changed significantly through the course of the deformation. The true strain is the integral of the incremental strain over the entire deformation and provides a better representation of the extent of deformation relative to the actual length of the material element than does the engineering strain. If strains and deformations remain small, the true strain and Cauchy stress are effectively the same as the engineering strain and engineering stress.

Figure 5.2 shows a sample uniaxial tension test result and the associated first order (two-term) Mooney-Rivlin material curve obtained from a best-fit of the data points. The data is presented in terms of engineering stress and engineering strain. Also shown in the figure is a linear approximation to the Mooney-Rivlin curve. The slope of the linear approximation is assigned based on the small-strain slope (i.e., slope at the origin) of the hyperelastic curve and provides a direct relationship between the engineering stress and the engineering strain. The agreement between the hyperelastic curve and the linear approximation is only acceptable for engineering strains in the ±10% range.

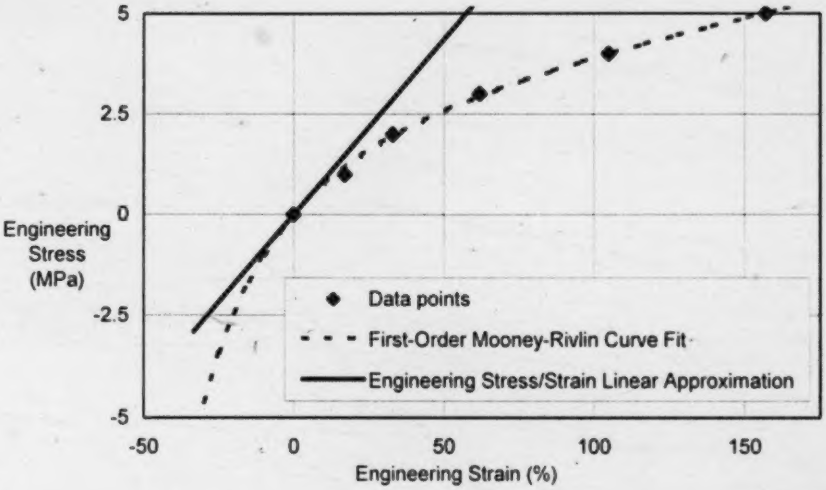

Figure 5.2. Sample uniaxial tension data with corresponding Mooney-Rivlin curve and associated linear approximation in terms of engineering stress and engineering strain.

An improved linear approximation to the hyperelastic model may be obtained by considering the hyperelastic response in terms of the Cauchy stress and the true strain. Figure 5.3 shows the test data and the hyperelastic description seen in Figure 5.2 in terms of these more appropriate stress and strain measures. A linear approximation relating the Cauchy stress to the true strain using the slope of the hyperelastic description at the origin is also shown. This "large-strain" linear description constructed in the context of Cauchy stresses and true strains provides a much closer approximation to the hyperelastic material curve than was achieved with engineering stress and engineering strain quantities.

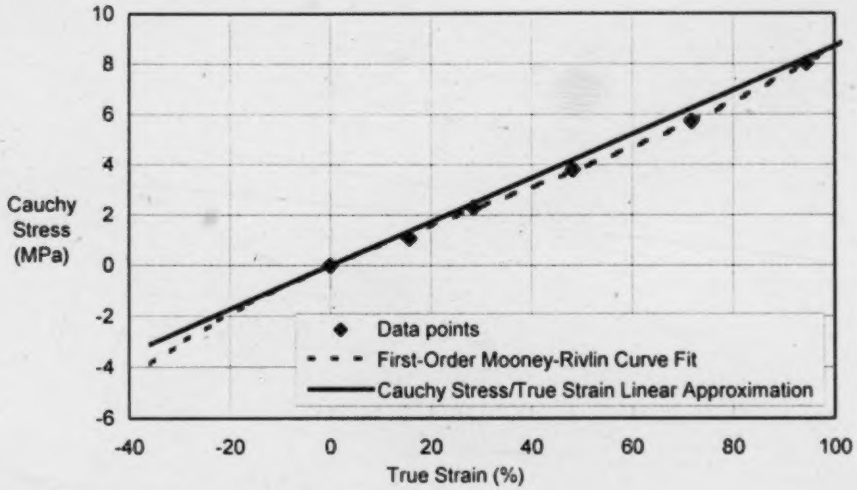

Figure 5.3. Sample uniaxial tension data with corresponding Mooney-Rivlin curve and associated linear approximation in terms of Cauchy stress and true strain.

The use of a linear approximation in Cauchy stress and true strain quantities may be implemented using a material model available in the ADINA finite element software. The elastic strain region of a thermo-elastic-plastic material model is used for all analyses described in this study. While the selected bilinear material model is generally used to describe stress-strain behaviour through a linear elastic and linear plastic range, the elastic component of the available material description provides enough flexibility to accurately portray the behaviour of the elastomer. The elastic strain range for the model is defined in terms of Cauchy stress and true strain. Hence, the Cauchy stress/true strain linear approximation of elastomer response described in the preceding paragraph is easily accommodated. The calculated slope of the hyperelastic curve at the origin (in terms of Cauchy stress and true strain) is used as the elastic modulus. The model is kept in the elastic strain range by setting the material yield strength equal to the elastic modulus, which corresponds to strains far higher than those encountered in PCP and PDM applications. As a result, all deformations of the elastomer are treated as elastic. The elastic modulus may be described as a function of temperature. The material model also includes a thermal expansion description, providing analysis functionality that is not available from hyperelastic material models in ADINA 7.3.

A comparative study provides an understanding of the limitations of making the large-strain linear approximation to the hyperelastic material curve in the context of the types of pumps and motors being analysed. Analyses of a high-interference conventional single-lobe pump using both the hyperelastic material model and the associated large-strain linear approximation form the basis for comparison. Errors in peak stresses and peak strains are on the order of 0.3% and 2.7% respectively. While the large-strain linear approximation does not provide an exact mapping of the hyperelastic material description, the errors incurred in this process are thought to be acceptable given the benefit they provide over the available isothermal hyperelastic material description.

5.1.3 Bulk modulus effects

The bulk modulus is a material property that describes the volumetric response of a material to uniform hydrostatic pressure. The bulk modulus for elastomers is typically much larger than the elastic modulus, as the material is nearly incompressible. The structural finite element formulation used for this investigation uses the bulk modulus to model the slight compressibility of the material.

Bathe[11] shows that the basic equations used for infinitesimal analyses may be used to describe large-strain analyses if the stress-strain response is described in terms of Cauchy stress and true strain. This includes the relationship between the mean stress, τ_{mean} and the mean strain, ε_{mean}:

$$\tau_{mean} = 3 \cdot \kappa \cdot \varepsilon_{mean} \qquad [5.2]$$

where: κ is the bulk modulus;

τ_{mean} is the mean Cauchy stress, $(\tau_{11}+\tau_{22}+\tau_{33})/3$, where τ_{ij} are the components of the Cauchy stress tensor; and

ε_{mean} is the mean true strain, $(\varepsilon_{11}+\varepsilon_{22}+\varepsilon_{33})/3$, where ε_{ij} are the components of the logarithmic (Hencky) strain tensor.

Equation 5.2 shows that for a given hydrostatic strain, the resulting stress in the material is directly proportional to the value of the bulk modulus.

As the bulk modulus is not typically investigated in standard elastomer tests, a study of the effects of variations in bulk modulus over the range described in the literature is required in order to understand the implications of variations in this material property. Analyses of a sample conventional single-lobe PCP using the two-dimensional modelling strategy described in Section 5.3 provide an indication of the sensitivity of the response to the bulk modulus property. Results of these analyses show that in the context of progressing cavity pumps, there is little variation in structural response when the bulk modulus is changed over a range of values from 150 ksi (1034 MPa) to 350 ksi (2413 MPa). Three-dimensional modelling using the strategy described in Section 5.4 confirms that the effect is minimal. This minimal sensitivity is also expected in other PCP and PDM configurations if the hydrostatic stress does not dominate the overall stress state in the material. Given the minimal effect that variations in bulk modulus have on structural modelling results, the bulk modulus is assumed to be constant at 250 ksi (1724 MPa) for the remainder of the investigation.

5.1.4 Temperature-sensitive material property considerations and thermal expansion considerations:

The temperature-dependent structural response of elastomers is critical in evaluating component response when elevated temperatures are present. In this study, temperature changes of up to 100°C were anticipated. In general, elastomers are always employed above the *glass transition* *temperature*, the point at which the material changes from a glassy state to a rubbery state.[21] It is assumed that the elastomer was operating above the glass-point temperature where deformations are largely recoverable.

Variations in structural elastomer properties with temperature are accommodated using the thermo-elastic-plastic material model available in ADINA 7.3.[11] This material model is designed to use linear interpolation between points specified at discrete temperatures to describe the variation in material properties over the range of specified temperatures.

5.1.5 Approximation to dynamic loading

The structural finite element modelling strategies described herein use a series of static structural analyses to emulate the motion of the rotor as it moves within the stator. This assumption means that the dynamic component of the viscoelastic elastomer response is not explicitly accounted for within the structural models. Instead, this dynamic component is incorporated into heat generation routines and is based on results of dynamic material testing, as described in Section 6.2. The effect of this approximation on structural results is closely related to the viscous loss modulus of the elastomer.

5.2 Structural Finite Element Formulations

An important part of this study is the selection of appropriate continuum and contact elements for modelling the response of the stator. Proper selection and usage of structural elements facilitates the convergence of finite element solutions and continuity of structural results. The stator elastomer and housing are modelled using continuum elements. The rotor is modelled as a rigid contact surface and the inner profile of the stator elastomer is discretised with contact segments. The ADINA 7.3 finite element analysis software is used for all structural analyses.

5.2.1 Continuum element formulations

Continuum elements used for structural modelling of the stator elastomer and housing are biquadratic isoparametric elements. These elements make use of quadratic shape functions to describe variations in field variables and the element geometry. In the case of two-dimensional (2D) modelling, 9-node elements are used. Analogous 27-node elements are used for three-dimensional (3D) modelling. Figure 5.4 shows schematics of these elements.

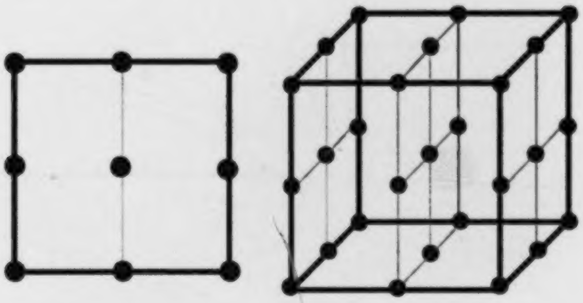

(a) 9-node 2D element (b) 27-node 3D element

Figure 5.4. Continuum elements used to model stator elastomer and housing.

The ADINA finite element software used for this study is equipped with structural solid elements that make use of independent displacement and pressure degrees of freedom. These elements, termed "mixed displacement/pressure interpolation elements" or "mixed u/p elements", provide significant computational advantages in analyses with near-incompressible materials such as elastomers. The small volumetric strains present in such analyses can produce discontinuous results and hamper solution convergence if the mixed formulation is not used. Based on a comparison of standard displacement-based elements and mixed displacement/pressure elements through representative two-dimensional stator analyses, it is apparent that the mixed formulation is superior for the purposes of this study. While the total number of degrees of freedom in the problem is increased by one-third, improved convergence makes the mixed u/p elements more efficient than displacement-based elements. Further descriptions of the mixed formulation elements may be found in the literature.[11, 22]

5.2.2 Contact element formulations

The continuous contact that is present between the rotor and stator components of progressing cavity pumps and positive displacement motors necessitates the use of contact elements in all structural finite element models. Two-node 2D contact elements provide a linear geometry description of the contacting surfaces in the modelling cross-section. Four-node 3D contact surfaces also use a linear description to describe the geometry of the inner surface of the elastomer and the outside profile of the rotor.

A constraint-function formulation in ADINA 7.3 is used to model contact in both the two-dimensional and three-dimensional finite element models. The formulation is based on two constraint equations, one governing normal contact and one governing frictional behaviour. The first equation enforces the condition that the product of the gap between the faces of two surfaces and the corresponding normal force must be zero. Hence, if the bodies are in contact (i.e., the gap is zero), the normal force may be non-zero, and vice-versa. The second equation is used to describe tangential motion between contacting surfaces and to detect whether two bodies in frictional contact will move relative to one another. This is done by comparing the tangential traction between two surfaces to the maximum available frictional force (i.e., the normal force multiplied by the friction factor). If the maximum frictional force is greater than the applied tangential traction, the relative tangential velocity at the point of contact must be zero; otherwise, the bodies must move relative to one another. A complete description of this contact formulation is presented by Bathe.[11]

5.2.3 Mesh density

The 9-node two-dimensional continuum element and 27-node three-dimensional continuum element require the use of mapped meshing to discretise the stator elastomer and housing components for finite element analyses. The quadratic element shape functions allow for the use of a lower mesh density than would be required if linear continuum elements were employed. The localised nature of the contact between the rotor and stator means that a fine mesh is required in the two-dimensional model to accurately capture the time-history of the structural response at each point in the elastomer. Figure 5.5 (a) through (c) present sample effective stress contours from two-dimensional models of a typical single-lobe PC pump with increasing mesh refinement.

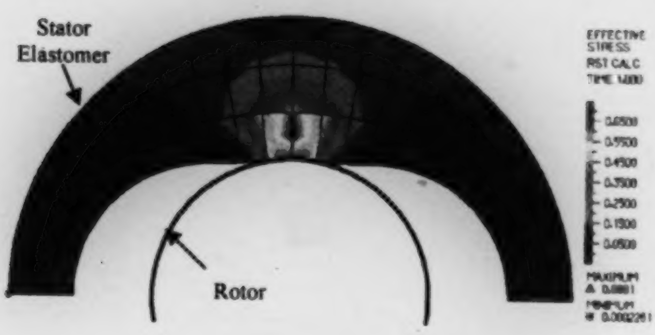

(a) 3 radial elements, 24 circumferential elements.

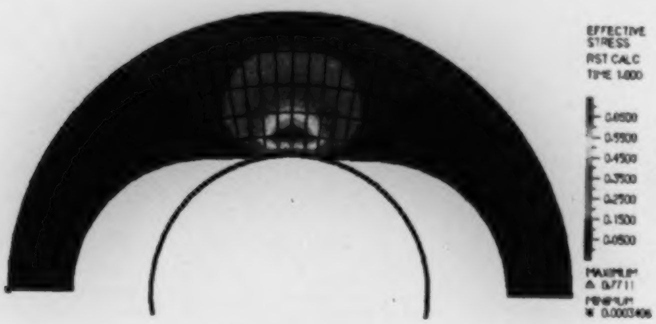

(b) 5 radial elements, 48 circumferential elements.

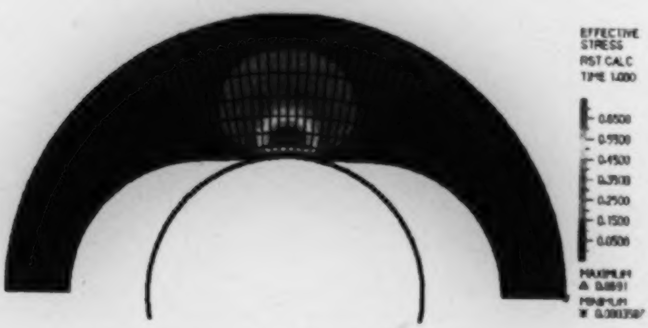

(c) 7 radial elements, 80 circumferential elements.

Figure 5.5. Improvement of elastomer effective stress contour results with mesh refinement. (Units in MPa)

The density of the two-node linear contact elements used to discretise the inner stator profile and rotor surface is largely dependent on the density of the continuum elements on the inner stator profile. Contact elements on the inner elastomer profile are assigned based on the locations of the edge nodes of the surface continuum elements. For each 3-node edge of a continuum element, a pair of two-node linear contact elements are assigned. Discretisation of the rotor into contact elements is fine enough to provide a smooth description of the circular rotor surface. Rotor element lengths are generally much smaller than the edge lengths of the continuum elements used to describe the inner stator profile, as shown in Figure 5.6. Each "1" shown on the surface of the rotor represents the midpoint of a two-node contact element. Similar contact elements exist on the surface of the stator; these were omitted from the figure for clarity.

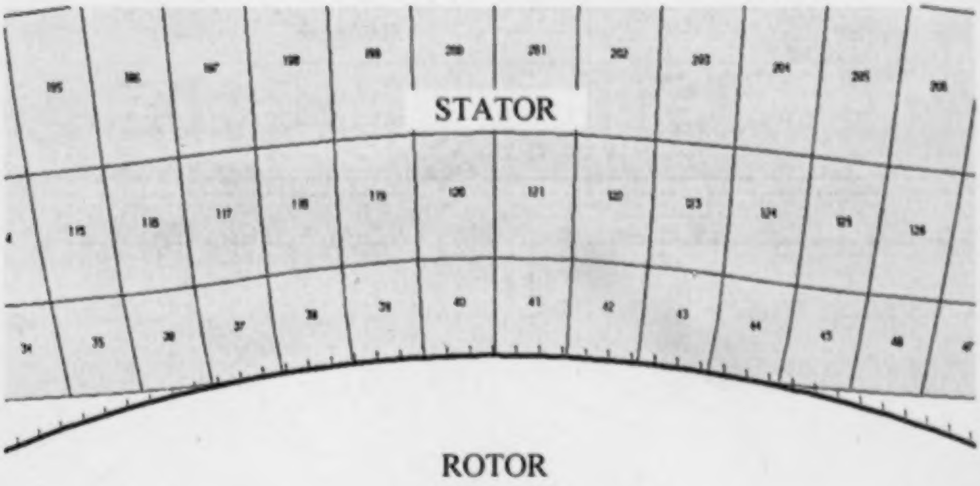

Figure 5.6. Rotor contact element discretisation at contact point in a single-lobe stator. Contact elements are marked with a "1"; continuum elements are numbered.

5.3 Two-dimensional Structural Modelling

5.3.1 General two-dimensional modelling considerations

The two-dimensional structural finite element modelling strategy is a computationally efficient way to analyse the structural response of the stator elastomer under representative loading. Errors resulting from the two-dimensional models lie primarily in the fact that the helical axial geometry of the stator and the associated contact lines formed with the rotor result in some elastomer deformations out of the selected cross-section. In addition, the equilibrium position of the rotor within the stator is not uniquely identifiable simply using the two-dimensional model. Sections 5.4 through 5.6 contain discussion regarding the three-dimensional modelling strategy, equilibrium considerations, and the results of comparisons between corresponding two and three-dimensional models.

5.3.2 Description of the models

Two-dimensional finite element models of the pump/motor units consist of cross-sections taken perpendicular to the longitudinal axis of the pump as illustrated in Figure 5.7. While the geometry of all cross-sections perpendicular to the longitudinal axis of the stator is identical, the orientation of the cross-section depends on the axial location relative to the stator pitch length. Similarly, all rotor cross-sections are identical with the exception of their orientations relative to the stator. Further details regarding rotor and stator geometries are presented in Chapter 2.

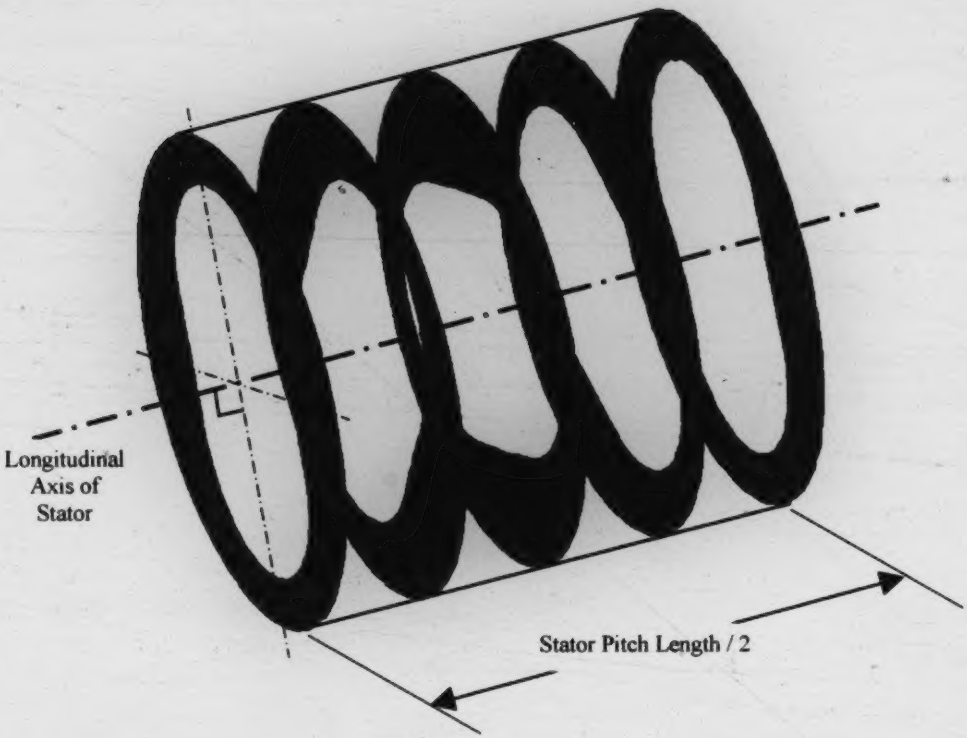

Figure 5.7. Sample stator cross-sections used for two-dimensional modelling.

Figure 5.8 shows sample cross-sections of a conventional single-lobe pump (Figure 5.8(a)), a uniform-thickness-elastomer single-lobe pump (Figure 5.8(b)), a conventional 2:3 multilobe pump (Figure 5.8(c)), and a modified 2:3 multilobe pump (Figure 5.8(d)). In this study, only conventional single-lobe pumps and motors like those shown in Figure 5.8(a) are considered. Extension of the modelling strategy to more complicated geometries is straightforward.

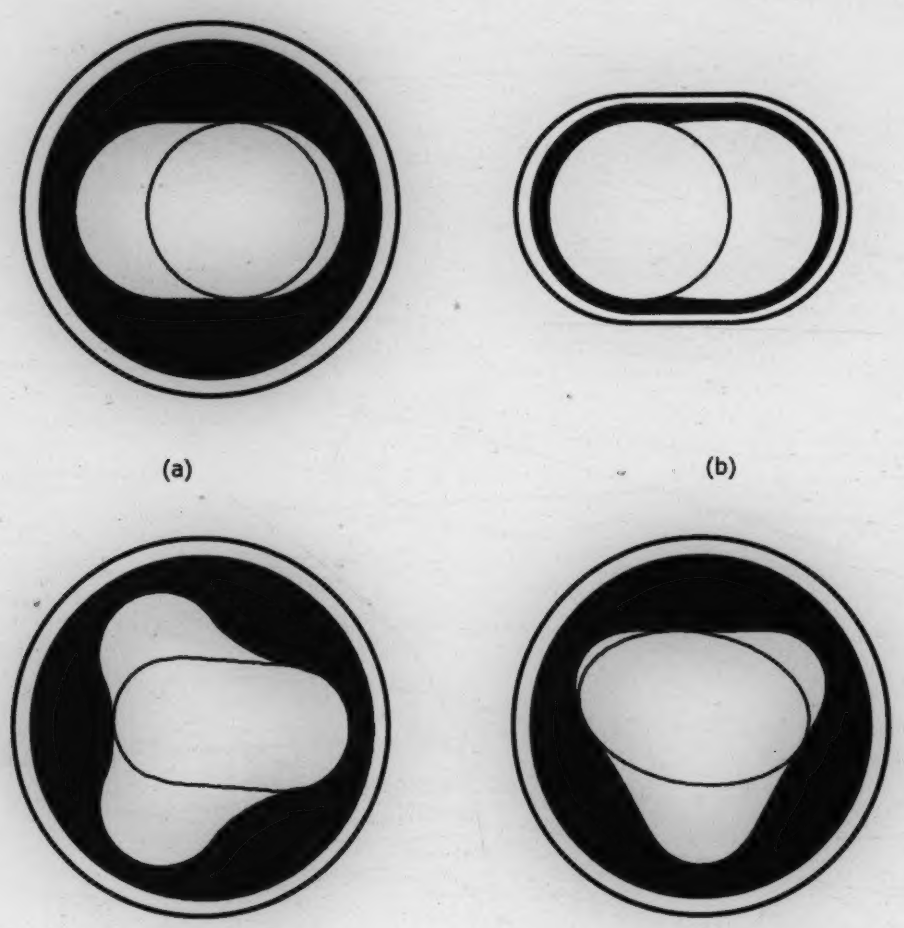

(a) (b)

(c) (d)

Figure 5.8. Cross-sections of common pump configurations: (a) Conventional single-lobe; (b) Uniform thickness single-lobe; (c) Conventional 2:3 multi-lobe; (d) Modified 2:3 multi-lobe.

The static structural response obtained through finite element analysis of the two-dimensional representation of the stator is dependent on the position of the rotor cross-section within the stator cross-section. The motion of the rotor as it progresses through its rotational cycle is modelled by incrementing the rotor position for a series of sequential static analyses. For the purposes of this study, the position of any single-lobe pump rotor with respect to the stator is described using the angular measure θ shown in Figure 5.9. When the rotor is in the 0° position, the rotor cross-section is positioned in the centre (laterally) of the stator cavity. As θ reaches 90° the rotor contacts the major seal at the end of the cavity.

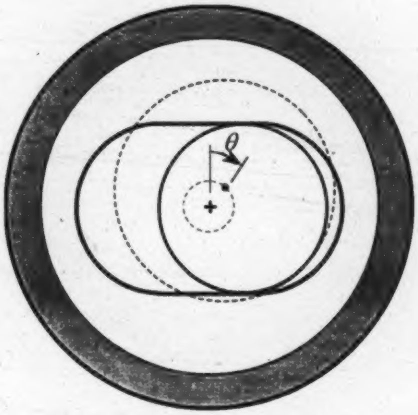

Figure 5.9. Definition of single-lobe rotor position angle θ.

The rotor cross-section is assumed to be rigid due to the large relative difference in stiffness between the elastomer and the rotor. The housing is included in the structural model, as hoop and bending stresses result from the various loads applied to the stator during operation. Structural modelling of the housing may provide some insight into the advantages and disadvantages of different types of housings currently being used in industry.

5.3.3 Generalised plane strain assumption

A generalised plane strain assumption is used for the analysis of two-dimensional pump and motor cross-sections. In operation, much of the elastomer material in cross-sections located away from the ends of the stator is confined from moving in the axial direction. Most out-of-plane elastomer displacements that occur in the stator are related to the helix angles of the stator and the rotor and the shape of the associated contact surfaces. These effects must be quantified using 3D models. Axial deformation may also result from volumetric expansion of the elastomer due to temperature increases and/or incompatibility with operating fluid. Using the generalised plane strain approach, out-of-plane deformations may be limited to uniform axial displacements of the entire cross-section. This provides a better 2D approximation to the stator response than a plane strain formulation that disallows all out-of-plane deformations.

5.3.4 Stator boundary conditions

For all two-dimensional models, the motion of the rotor within the stator may be modelled by incrementing the rotor position through a rotational path. Stator boundary conditions are chosen so that representative behaviour of the stator housing can be incorporated into the analysis. Previous modelling studies[17] assume that the perimeter of the elastomer in the cross-section is fixed as shown in Figure 5.10. While the tensile stiffness of the housing is on the order of 25,000 times that of the elastomer, small changes in the housing dimensions must be compared to the rotor/stator interference dimension before their significance may be discarded. In pump and motor units, internal pressure loading may induce significant reductions in rotor/stator interference through changes in the housing hoop dimension. In extreme cases, the hoop stress caused by the rotor/stator interference can also contribute to dimensional changes in the housing.

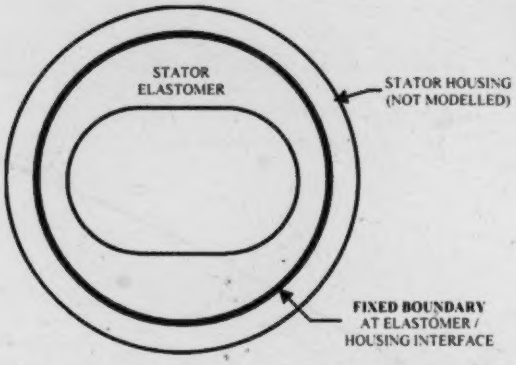

Figure 5.10. Fixed elastomer OD boundary condition used previously.[17]

For single-lobe stators, boundary conditions were applied to nodes on the outside diameter of the stator housing as shown in Figure 5.11. Nodes A and B were free to translate in the Y-direction and were fixed in the Z-direction. Likewise, nodes C and D were allowed to translate in the Z-direction and were fixed in the Y-direction. These degrees of freedom prevented rigid-body motions while incorporating stator housing behaviour.

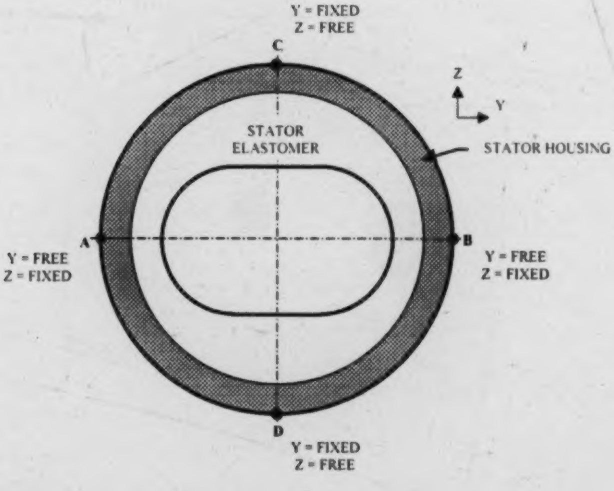

Figure 5.11. Single-lobe pump stator boundary conditions.

Limitations of the boundary conditions described above are only apparent when extreme conditions are present. For instance, if the rotor path is such that the rotor encounters a large amount of interference on the major diameter, the force generated by the ensuing confinement of the elastomer may be enough to create a significant stress concentration near the constrained nodes at positions C and D on the housing as shown in Figure 5.12. This scenario is generally not anticipated when rotor force equilibrium considerations (discussed in Sections 5.5 and 5.6) are taken into account.

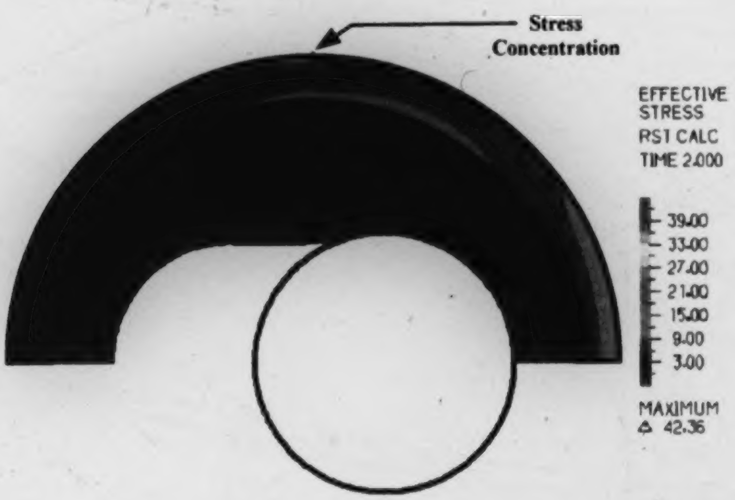

Figure 5.12. Stress concentration at constraint location on housing due to excessive interference at major seal (90° position). (Stress in MPa)

5.3.5 Loading

5.3.5.a Rotor/stator interference

The capability of progressing cavity pumps and positive displacement motors to generate pressure is created through interference between the rotor and stator elastomer. Rotors are designed so that a series of seal lines are formed with the stator, creating a number of constant-volume fluid cavities. The seals permit a pressure differential to exist between successive cavities as the pump or motor operates. The interference between the components may cause significant stresses to develop within the stator elastomer and housing. The following paragraphs discuss interference loading in the context of single-lobe progressing cavity pumps. The principles discussed may be applied to more complicated geometries.

Interference between the rotor and stator in single-lobe progressing cavity pumps creates between one and two seal locations in any cross-section perpendicular to the longitudinal axis. Figure 5.13 shows cross-sections of the stator with the rotor at various positions in its rotational path.

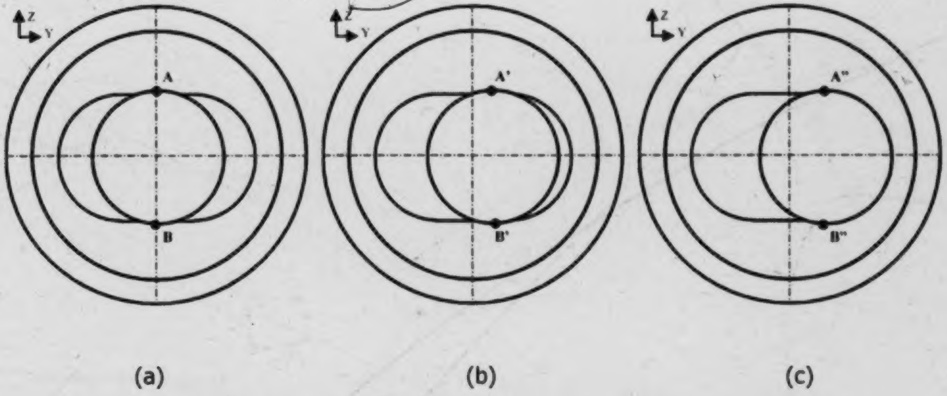

Figure 5.13. Position of seal location(s) in single-lobe cross-section.

It is incorrect to assume that the rotor motion in the single-lobe stator cross-section is purely lateral. The contact conditions at different points along the axial length of the stator cause the rotor to move in an elliptical path within the stator cross-section. The interference level at seals A and B in Figure 5.13 is therefore not typically the same. To illustrate this, Figure 5.14 shows the simultaneous rotor/stator contact conditions in two cross-sections spaced one-half rotor pitch apart. At axial position X, contact between the rotor profile and the stator cavity profile (shown in bold) is the same as that seen in Figure 5.13(a). At axial position $X + \frac{1}{2}P_{rotor}$, contact between the rotor and stator profiles is the same as shown in Figure 5.13(c). The net contact force on the rotor in each cross-section is dependent on the interference fit and the resistance (stiffness) of the stator to this interference. At axial position X, the net force in the Y direction is zero if interferences at seals A and B are the same. The interference at seal A must therefore be larger than the interference at seal B to counteract the out-of balance loads in the Y direction generated at axial position $X + \frac{1}{2}P_{rotor}$ in order for the rotor to maintain force equilibrium. The actual rotor equilibrium position is determined by rotor/stator interaction along the entire pump or motor length.

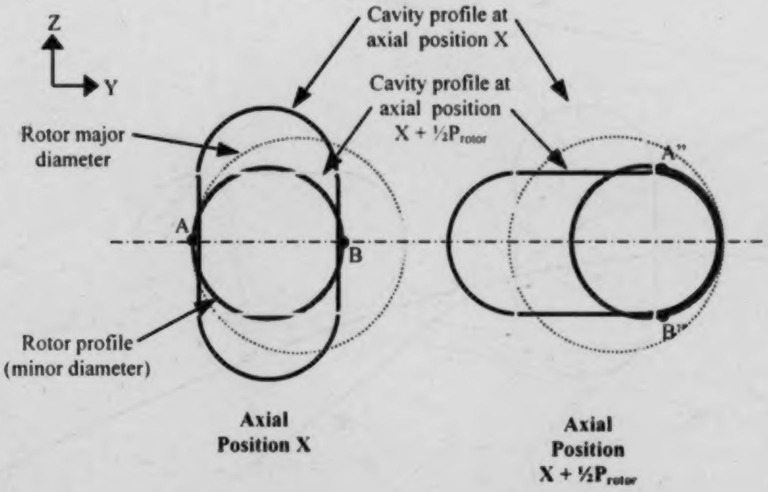
Z
Y
Cavity profile at axial position X
Cavity profile at axial position $X + \frac{1}{2}P_{rotor}$
Rotor major diameter
A
B
A''
B''
Rotor profile (minor diameter)
Axial Position X
Axial Position $X + \frac{1}{2}P_{rotor}$

Figure 5.14. Rotor interaction with inner stator profile at time *t* at pump cross-sections spaced one-half rotor pitch apart.

The rotational path of the centre of mass of the rotor within a single-lobe stator is circular. The radius of this circle is frequently referred to as the *pump eccentricity* or *radius of eccentricity*. Figure 5.15 shows that the radius of eccentricity obtained by the assumption of a lateral rotor path in the stator cross-section overestimates the actual radius of eccentricity (elliptical path). The difference δ between the two radii of eccentricity is equivalent to the distance between the assumed and equilibrium interferences at the major diameter.

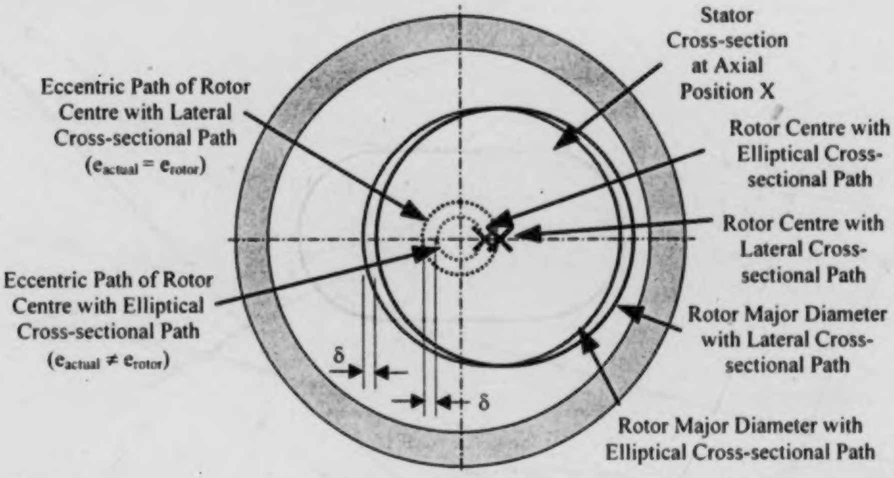
Stator Cross-section at Axial Position X
Eccentric Path of Rotor Centre with Lateral Cross-sectional Path
($e_{actual} = e_{rotor}$)
Rotor Centre with Elliptical Cross-sectional Path
Rotor Centre with Lateral Cross-sectional Path
Eccentric Path of Rotor Centre with Elliptical Cross-sectional Path
($e_{actual} \neq e_{rotor}$)
Rotor Major Diameter with Lateral Cross-sectional Path
δ
δ
Rotor Major Diameter with Elliptical Cross-sectional Path

Figure 5.15. Eccentric paths of rotor centre for assumed and equilibrium (elliptical) rotor paths.

For the purposes of this investigation, the actual eccentricity of the rotor path is designated as e_{actual} and is defined by

$$e_{actual} = e_{rotor} - e_{3D} \qquad [5.3]$$

where: e_{rotor} is the radius of eccentricity assuming the motion of the rotor cross-section is purely lateral and is defined solely by the rotor geometry; and

e_{3D} is defined as the eccentricity offset.

While a single two-dimensional finite element model cannot be used to determine the value of the actual eccentricity, two-dimensional analyses may be conducted if the actual eccentricity is known. Sections 5.4 and 5.5 discuss methods that may be used to obtain the eccentricity offset using three-dimensional models and an iterative strategy for finding the offset with two-dimensional models.

Given the rotor and stator geometries and the actual eccentricity, a series of sequential static two-dimensional structural models provides an indication of stator response at discrete points in the rotational path of the rotor. Figure 5.16 shows rotor positions used to model one-quarter of a rotor cycle.

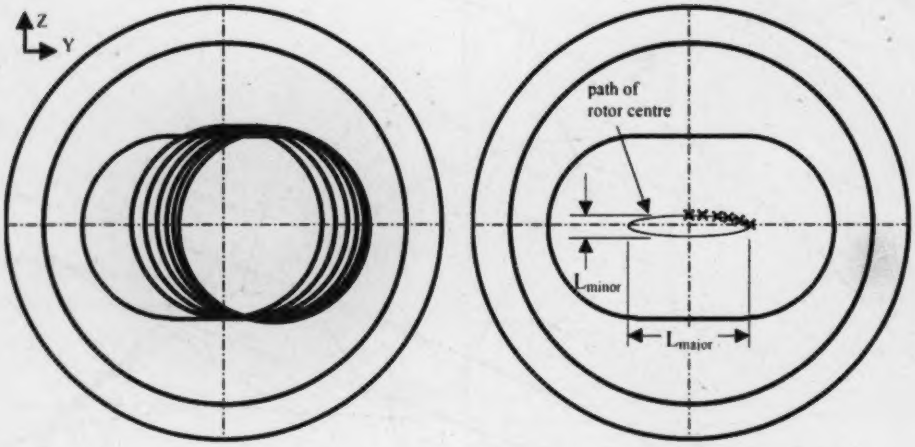

(a) (b)

Figure 5.16. Rotor positions used to model quarter rotor cycle.

The elliptical path of the rotor centre is defined by the rotor eccentricity, e_{rotor}, and the eccentricity offset, e_{3D}. The lengths of the major and minor axes of the ellipse, L_{major} and L_{minor}, are defined by

$$L_{major} = 2 \cdot (2 \cdot e_{rotor} - e_{3D}) \qquad [5.4]$$

$$L_{minor} = 2 \cdot e_{3D} \qquad [5.5]$$

and are shown in Figure 5.16(b). It should be noted that the predicted value of e_{3D} and the value of e_{rotor} are such that the ratio of major to minor axes is typically large. For the four pumps used in the verification testing program discussed in Chapter 9, this ratio is between 30 and 150.

The rotor trajectory shown in Figure 5.16 may be generated in a two-dimensional model using sinusoidal variations in rotor displacements in the Y and Z directions shown on the figure. The planar rotational degree of freedom may also be used to apply rotation about the rotor centre for modelling frictional loads. The position of each rotor node was assigned for each sequential static analysis step.

Figure 5.17 shows an example of the effective (von Mises) stresses that develop within the elastomer from the rotor/stator interference load. The stresses in the elastomer are different in the vicinity of the two rotor/stator contact points because of the different interference levels that result from the eccentricity offset, e_{3D}.

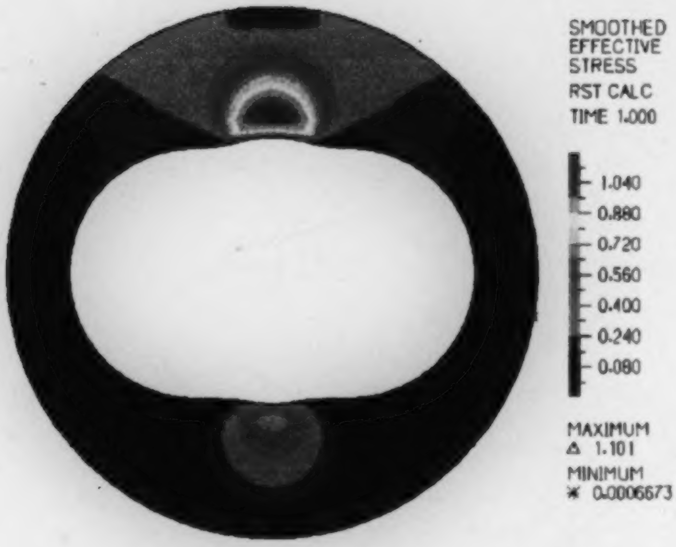

Figure 5.17. Sample elastomer effective stress profile with uneven interference on minor seal (i.e., $e_{3D}\neq 0$) with rotor at 0° position. (Units in MPa)

5.3.5.b Thermal expansion

The high thermal expansion coefficient of typical elastomers can result in changes in the stator geometry. The confinement induced by the stator housing results in an inward expansion of the elastomer. This changes the shape of the stator profile and can magnify the rotor/stator interference loads. Figure 5.18 shows an elastomer temperature profile that could be encountered during pump operation.

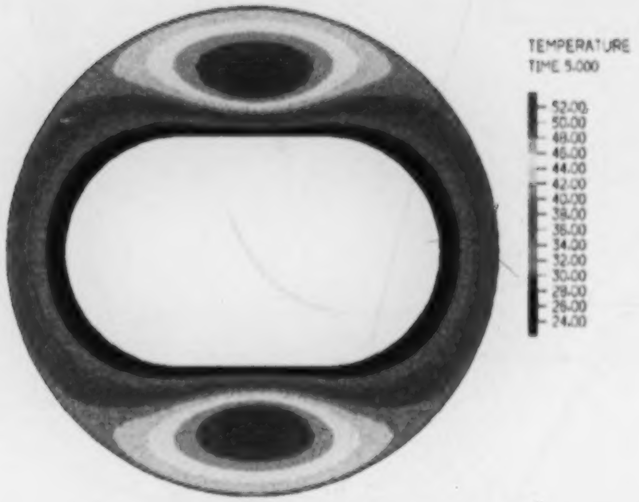

Figure 5.18. Sample elastomer temperature profile. (Units in °C)

Elastomer thermal expansion properties are assumed to be isotropic. The thermal expansion of the material is governed by the relationship

$$\varepsilon_{thermal} = \alpha \cdot (T_{elastomer} - T_{ref}), \qquad [5.6]$$

where: $\varepsilon_{thermal}$ is the thermal strain in each of the three normal directions;

α is the linear coefficient of thermal expansion (1/°C);

$T_{elastomer}$ is the applied temperature (°C); and

T_{ref} is the ambient (reference) temperature (i.e., temperature at which no thermal expansion occurs) (°C).

Thermal expansion is induced in finite element models by assigning a temperature field, thermal expansion coefficient, and reference temperature to the continuum elements that form the stator elastomer and housing.

Sample two-dimensional generalised plane-strain models show that the bulk of the thermal expansion imposed on the elastomer is absorbed through planar deformations within the modelling cross-section. The axial deformation is minimal because of the small thermal expansion coefficient of the stator housing material and the relative stiffnesses of the elastomer and housing. Figure 5.19 shows this concept graphically. The elastomer would extend much farther under a uniform thermal expansion load than the steel would if the materials were not bonded together. However, the overall extension of the two materials with the bond is closer to the free-expanded length of the housing because the housing is so much stiffer than the elastomer. It was assumed that the helix angle of the stator did not cause out-of plane elastomer deformations under this type of load for all 2D analyses.

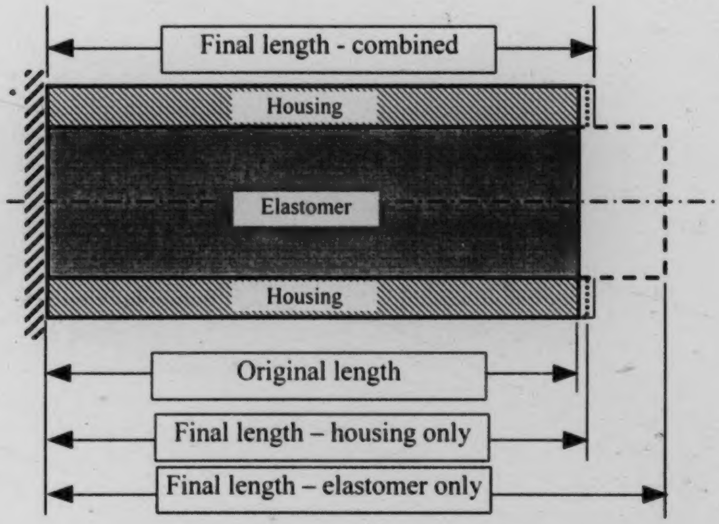

Figure 5.19. Thermal expansion schematic.

5.3.5.c Volumetric swell

Fluid incompatibility can cause elastomers to expand volumetrically during downhole operation. Uniform volumetric swelling loads may be imposed with the method used for modelling thermal expansion loads because both types of loads cause bulk expansions of the elastomer material. The simplest way of inducing a volumetric strain in the elastomer is to apply a temperature increase that will generate the desired amount of volumetric swell. Care must be taken to do this without taking away the capability to model thermal expansion loads.

In Section 5.3.5.b, the reference temperature, T_{ref}, is introduced as the temperature at which no thermal expansion occurs. The thermal strain is obtained by comparing the actual elastomer temperature, $T_{elastomer}$, to the reference temperature as shown in Equation 5.6. Swelling loads may be applied in conjunction with thermal expansion loads by lowering the reference temperature of the elastomer. The reference temperature of the elastomer is lowered by an effective temperature increase, ΔT_{swell}, to a new reference temperature, $T_{ref}'_{(elastomer)}$. The effective temperature increase may be approximated using

$$\Delta T_{swell} = \frac{swell}{300 \cdot \alpha}, \qquad [5.7]$$

where: *swell* is the volumetric expansion of the elastomer due to factors other than temperature changes (%).

This causes a volumetric expansion in the elastomer that accounts for the swelling load. The reference temperature of the housing material remains equal to T_{ref}, as swelling affects only the elastomer. This strategy is used so that the capability to model thermal expansion effects independently is maintained. Figure 5.20 shows a graphical representation of this load application strategy along a sample profile at the thickest part of a single-lobe stator cross-section.

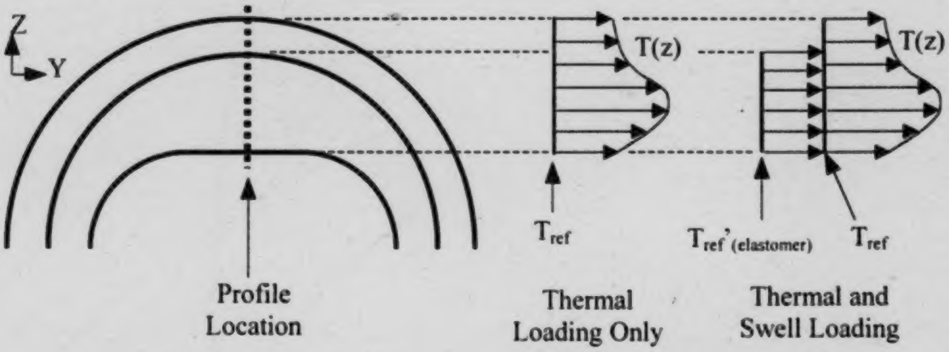

Figure 5.20. Combined thermal/swell loading application strategy for 2D modelling.

The applied temperature profile, $T(z)$, creates the same amount of thermal expansion in both thermal and combined thermal/swell loading scenarios. Changing the elastomer reference temperature from T_{ref} to $T_{ref}'_{(elastomer)}$ imposes the elastomer swelling load.

An assumption made with this method of loading is that the axial elongation resulting from the swelling load does not appreciably affect the structural results. The capability to model spatial gradients in swelling loads has not been developed.

5.3.5.d Uniform internal pressure

Internal pressure loads are usually present when progressing cavity pumps or positive displacement motors operate. The near-incompressibility of the stator elastomer means that there is very little compliance within the elastomer itself to such loads. Hoop stress induced in the stator housing may also contribute to changes in shape of the inner elastomer profile. Pressure loads may be applied directly to the edges of the finite elements that border the fluid cavity. Figure 5.21 shows an example of the imposed pressure loading on a single-lobe progressing cavity pump.

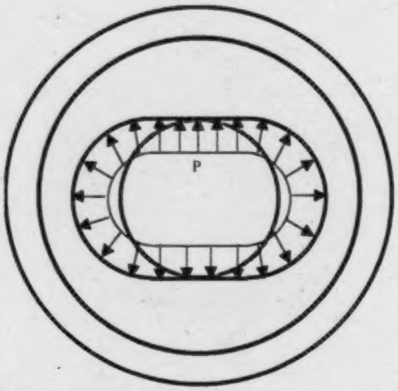

Figure 5.21. Applied uniform internal pressure loading for 2D model.

5.3.5.e Differential pressure

Pressure differences between adjacent fluid cavities can have a much more significant effect on stator structural response than uniform pressure loads. While a strategy for modelling uniform internal pressure for two-dimensional models is simple, a method for modelling variations in the applied internal pressure is more complicated. Figure 5.22 shows the cross-section of a single-lobe pump with an applied internal pressure distribution representative of what might be seen during operation.

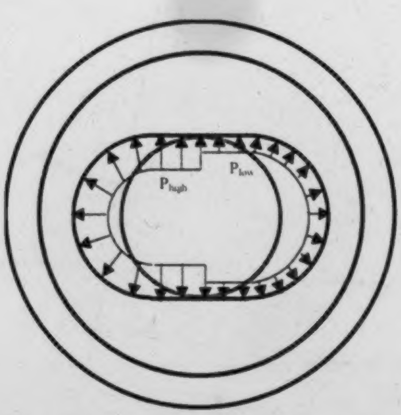

Figure 5.22. Sample pressure distribution in a single-lobe pump.

While the position of the rotor dictates the location of the change in pressure, the application of the pressure load in a finite element model will change the location of rotor/stator contact. Initial investigations of differential pressure response show that modelling results are not sensitive to the distribution of pressure near the rotor/stator contact patch. It is therefore assumed that the results will be insensitive to the pressure distribution in the immediate vicinity of the contact point. Figure 5.23 shows the pressure distribution for a single-lobe pump model where only the differential pressure is modelled. The applied internal pressure is constant to the left of the centre of the rotor/stator contact patch. The pressure then decreases linearly to zero over a short interval.

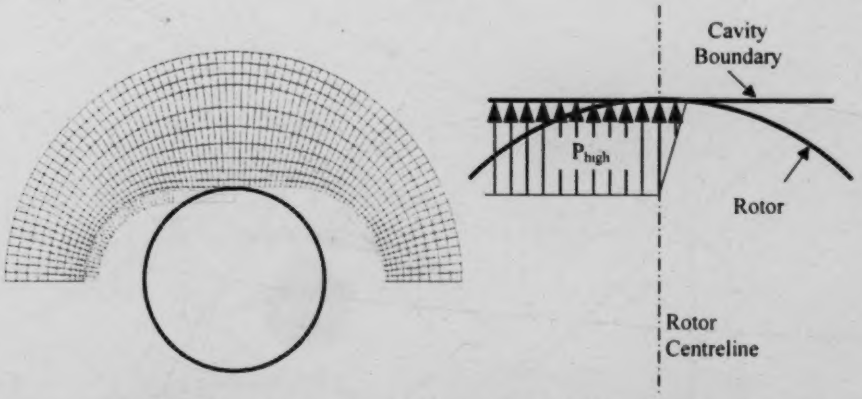

Figure 5.23. Applied differential pressure profile for 2D half pump model (rotor at 0°).

Use of the differential pressure modelling strategy is possible by varying the spatial function that describes the internal pump pressure at each static rotor position analysed. Figure 5.24 shows the applied internal pressure distribution at four points in the rotor's rotational path. Combined uniform internal pressure and differential pressure may be applied by adding a uniform pressure load such as that seen in Figure 5.21 to the applied internal pressure distribution.

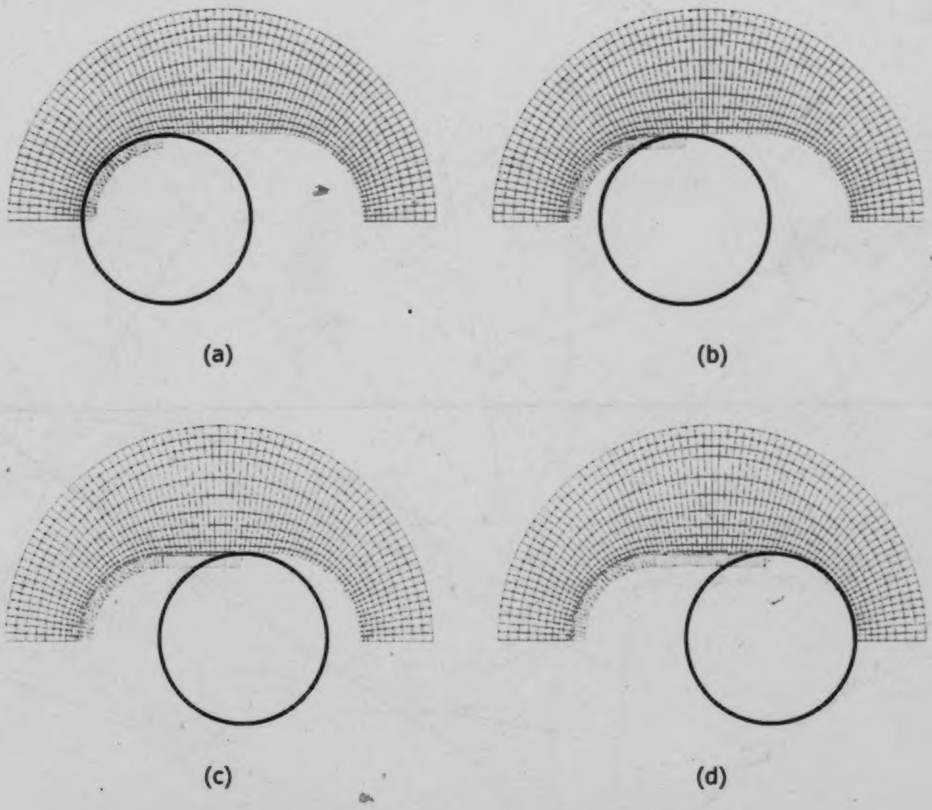

(a) (b)

(c) (d)

Figure 5.24. Applied differential pressure profile for 2D half pump model at -90°, -22.5°, 22.5°, and 90° rotor positions ((a) through (d) respectively).

5.3.5.f Friction

The interaction between a rotor and stator likely consists of a combination of rolling and sliding friction and hydrodynamic lubrication. For the purposes of this investigation, it is assumed that hydrodynamic effects are not present and that a single friction coefficient, μ, exists between the rotor and stator. The frictional force is related to the normal force using this coefficient:

$$F_f = \mu \cdot F_N \qquad [5.8]$$

where: F_N is the force normal to the contact surface;

μ is the coefficient of friction; and

F_f is the maximum frictional force.

By incrementing the rigid rotor surface through a rotational cycle and conducting static analyses at each point, the structural response of the stator to frictional loading may be approximated. Successive static analysis steps provide the program with an indication of the direction of the applied friction. The resulting frictional forces are applied in the direction tangential to the inner profile of the elastomer in its deformed configuration.

5.3.6 *Results interpretation*

Key results of structural analyses include specific stress quantities in the elastomer and housing and contact stresses between the rotor and stator. While the primary incentive for creating the structural modelling strategy for this study is the quantification of hysteresis heating energy, models developed using these strategies may be used for the design and optimisation of pumps and motors. Specifically, structural models may be used to characterise responses pertinent to elastomer fatigue failure and as tools for conducting parametric studies for design optimisation.

All six components of Cauchy stress and true strain are required for hysteresis heat energy calculations. However, for two-dimensional generalised plane-strain models, only the planar strain components ε_{22}, ε_{23}, and ε_{33} fluctuate noticeably as the rotor cycles within the stator. Non-zero values of the out-of-plane strain component ε_{11} are primarily a result of volumetric expansions due to swelling or thermal expansion. Comparisons between two-dimensional and three-dimensional models involving a strain energy criterion make use of all six stress and strain components for the three-dimensional models.

From a design standpoint, quantities such as the effective stress provide a good indication of the severity of the distortional stress state in the elastomer. The spherical stress component (pressure) also provides an indication of the amount of bulk compression that occurs. The pressure relates directly to the rotor/stator contact stress, one of the key quantities from a design standpoint. Another design criterion is the peak planar shear stress at the bond between the elastomer and stator housing. This bond transfers the torque applied to the elastomer by the rotor to the housing and may cause stator failure if improper bonding is present.

5.4 Three-dimensional Structural Modelling

5.4.1 General three-dimensional modelling considerations

The three-dimensional structural modelling work provides an indication of the accuracy and limitations of the two-dimensional modelling strategy described in Section 5.3. The helical geometry of Moineau rotors and stators and the associated orientation of differential pressure forces within the stator cavities encourage deformations out of the planes perpendicular to the pump longitudinal axis. These effects are not accounted for in the two-dimensional modelling work, where it is assumed that all deformations remained planar.

For 3D analyses, the stator is modelled using continuum elements while the rotor is assumed to be rigid as it is in the 2D analysis. Contact between the rotor and stator is assumed to be frictionless for all 3D models.

5.4.2 *Model length*

The helical nature of rotor and stator geometries in PCPs and PDMs means that symmetry conditions may be used to limit the size of three-dimensional models. The minimum model length is dictated by the axial distance between identical rotor/stator contact orientations. This minimum model length is

$$L_{min} = \frac{P_{rotor}}{N_{rotor}} = \frac{P_{stator}}{N_{stator}} \qquad [5.9]$$

where: P_{rotor} and P_{stator} are the rotor and stator pitch lengths; and

N_{rotor} and N_{stator} are the number of rotor and stator lobes.

Figure 5.32 (later in this Chapter) shows single-lobe rotor orientations as a function of pitch length.

In terms of overall model size, the reduction in the number of axial elements required to portray the behaviour of multi-lobe pumps tends to be counteracted by an increase in the required mesh density in cross-sections perpendicular to the pump axis.

5.4.3 *Model creation*

The development of functional models that provide useful results while maintaining an acceptable finite element problem size is an important step in the 3D modelling process. For 2D models, 64 static analyses describing a complete rotor cycle can be conducted in approximately 10 minutes. On the same computer (a Pentium III 333 MHz computer with 1 GB of RAM), a single static analysis using an efficient 3D model may take anywhere from 1 hour to 4 hours.

The helical geometry of rotors and stators may be difficult to generate if the capability to perform helical extrusions of a two-dimensional cross-section is not available in the pre-processing component of the finite element package. One alternative is to import the geometry from a separate solid-modelling software package that is capable of performing a helical extrusion. However, mapped meshing with brick elements may not be possible in this case. A second alternative is to add the helical component of the axial geometry after creating the finite element mesh. The geometry of any axial rotor or stator cross-section is identical to all other such cross-sections with the exception of the orientation. The 3D models used for this investigation are first created without a helical rotation as shown in Figure 5.25. The models are meshed in this orientation so that an accurate depiction of the housing and elastomer profiles is achieved and so that a series of uniformly spaced axial node layers is created.

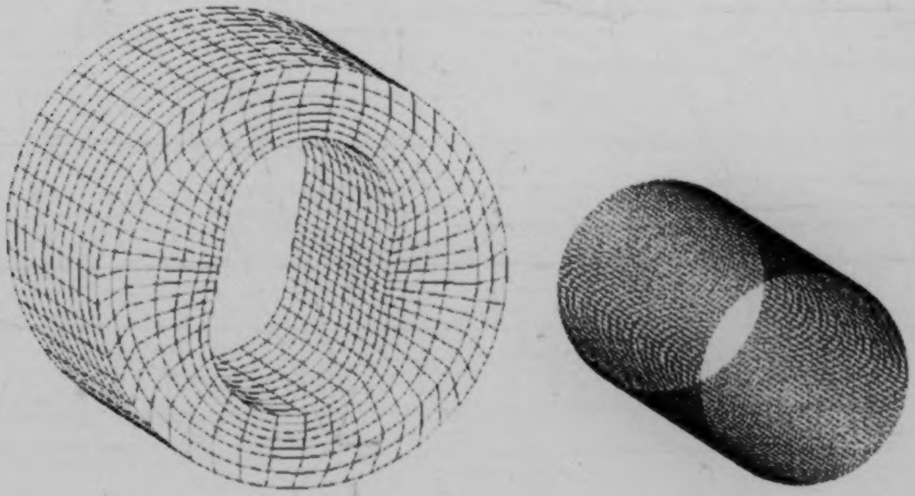

(a) Stator (b) Rotor

Figure 5.25. Unrotated 3D stator and rotor meshes.

The helical component of the stator geometry is introduced by rotating the orientation of each axial node layer through a coordinate transformation to create a helix. This produces a three-dimensional finite element model that consists of identical, equally spaced layers of nodes with the appropriate orientations as shown in Figure 5.26. A surface depiction of the rotor geometry is created using a similar procedure.

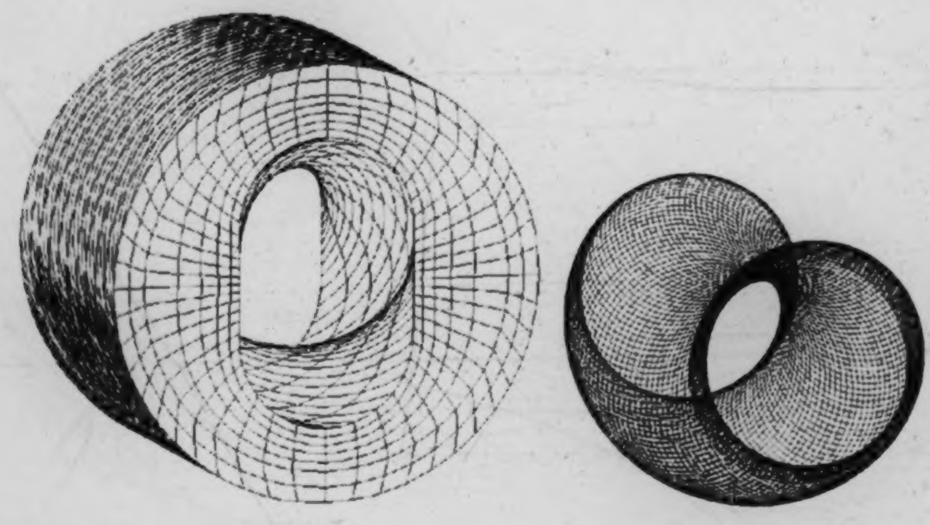

(a) Stator

(b) Rotor

Figure 5.26. Rotated 3D stator and rotor meshes

5.4.4 Boundary conditions

The equilibrium position of the rotor within the stator may be found using 3D models with appropriate boundary conditions. To achieve this, the position of the rotor is held fixed in the global coordinate system while the stator is allowed to move in directions perpendicular to the longitudinal axis of the rotor. This approach is more convenient than fixing the position of the stator and allowing the rotor to move because it facilitates the use of cyclic-symmetric boundary conditions on the end faces of the stator.

A combination of constraint equations and linear spring elements is used to allow the stator to find its equilibrium position while maintaining convergence stability. Only the three translational degrees of freedom are active at each node in the stator. Rigid-body translations in directions perpendicular to the pump axis are avoided by constraining four nodes on the outside diameter of the stator to move with an auxiliary node connected to a static ground position using soft springs as shown in Figure 5.27. Rigid-body translations in the axial (X) direction are prevented by connecting a very stiff spring element between the auxiliary node and static ground position.

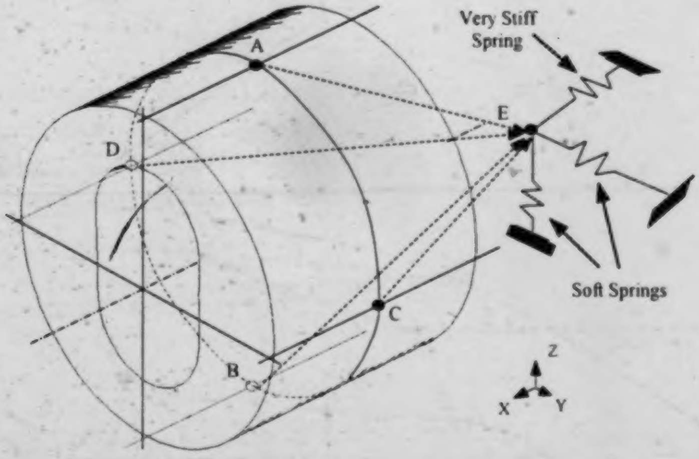

Figure 5.27. Nodes used to prevent rigid-body translations of the stator. Nodes A through D are spaced at 90° increments on the outside diameter of the stator housing; node E is an auxiliary node connected to ground through springs.

Constraint equations at the node pairs A-B and C-D are used to define the displacement at node E. These constraints are designed to allow the stator housing to deform from the applied interference loading while providing some resistance to rigid-body translations and rotations. The constraint equations used to generate this behaviour are:

$$u_X^C = -u_X^D + u_X^E; \qquad [5.10]$$

$$u_{radial}^A = u_{radial}^B + u_Z^E; \qquad [5.11]$$

$$u^{C}_{radial} = u^{D}_{radial} + u^{E}_{Y} \text{ ; and} \qquad [5.12]$$

$$u^{C}_{circumferential} = -u^{D}_{circumferential} \qquad [5.13]$$

where: u^{Q}_{i} is the displacement of node Q in direction i;

A through *E* are node labels;

circumferential and *radial* directions are defined in planes perpendicular to the pump longitudinal axis and are relative to the axis; and

X, *Y*, and *Z* are the global coordinate axes defined in Figure 5.27.

Equation 5.10 prevents rigid-body translations in the X direction by providing some resistance to the average X-translation of nodes C and D through the use of a spring. Equations 5.11 and 5.12 prevent rigid-body translations in the Y and Z directions in a similar fashion. Rigid-body rotations about the X axis are prevented by constraining the circumferential displacement of nodes C and D, as shown in Equation 5.13. Rigid-body rotations about the Y and Z axes are prevented using the constraint system discussed in the next paragraph.

The cyclic axial symmetry of the 3D models is achieved using constraint equations to equate the displacements at either end of the model as shown in Figure 5.28. By assuming the deformed shape of the stator at one end of the model was the same as the other, axial expansion due to end effects does not affect modelling results. Each face node at the constrained cross-section is assigned displacements that correspond to a matching face node at a cross-section one rotor pitch length away.

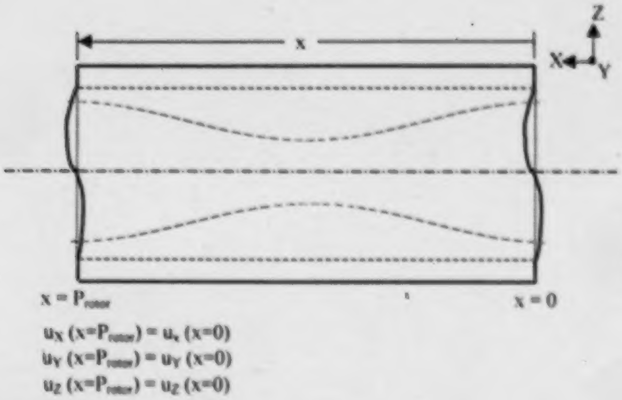
x
Z
X
Y
$x = P_{rotor}$
$x = 0$
$u_X(x=P_{rotor}) = u_x(x=0)$
$u_Y(x=P_{rotor}) = u_Y(x=0)$
$u_Z(x=P_{rotor}) = u_Z(x=0)$

Figure 5.28. End constraints (applied to all face nodes at $x = P_{rotor}$).

The primary limitation of the above method of modelling the stator is that a global elongation of the stator is not permitted. Axial displacements at both end faces of the model are the same, meaning that the overall length of the model is maintained. This has the greatest implication for analyses with applied uniform internal pressure loads or temperature changes that would encourage changes in the overall length of the stator. Such loads are not applied in 3D models used for benchmarking 2D models in this study.

5.4.5 Loading

Loads applied to 3D pump and motor models include the applied rotor/stator interference and differential pressure. The response of 3D models to interference loading can be used to understand the factors that control the equilibrium rotor position. Differential pressure loads are of interest because they act out of the plane of the two-dimensional models and can contribute to discrepancies between 2D and 3D modelling results.

Interference loads are applied to 3D models by changing the geometry of the rigid rotor through a series of static analysis steps. When the single-lobe 3D model is created, the rotor geometry is defined with a minor diameter smaller than the actual rotor diameter. The minor diameter is then increased incrementally in a series of analysis steps to guarantee convergence of the finite element solution. A static 3D structural solution is obtained for each step. The eccentricity of the rotor is held constant as the minor diameter is increased. The uniform expansion of the minor diameter is achieved by applying a radial expansion to each rotor node using a cylindrical skew coordinate system. The axial dimension of the rotor remains constant as the cross-sectional geometry changes.

Differential pressure loads for 3D models are applied using a method similar to that used for 2D models (see Section 5.3). The use of a spatial function to describe the pressure distribution is extended to include the two-dimensional surface that defines the inner profile of the stator elastomer. Figure 5.29 shows a schematic of the pressure distribution on the inside profile of an "unwrapped" single-lobe stator. The location of the pressure difference corresponds to the seal line formed between the rotor and stator.

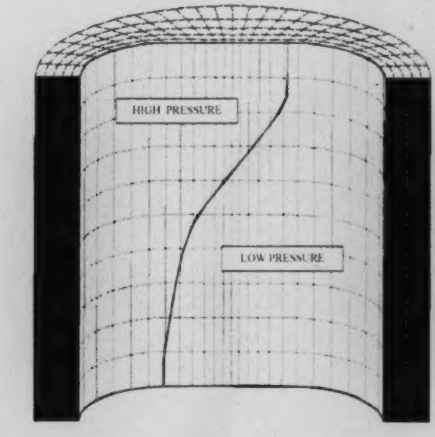

Figure 5.29. Pressure profile in a cross-section of "unwrapped" single-lobe pump stator.

Figure 5.30 shows the 3D pressure distribution after the helical component of the geometry is introduced. The shape of the pressure distribution is more complex because of the different pitch lengths of the rotor and stator.

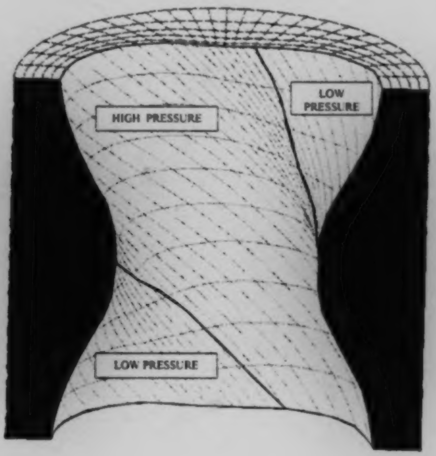

Figure 5.30. Pressure profile in a cross-section of single-lobe pump stator.

5.5 2D Equilibrium Position Procedure

The discussion in Section 5.3 indicates that two-dimensional structural models do not provide a simple means of determining the equilibrium position of the rotor within the stator. An iterative solution strategy for predicting the equilibrium rotor position using 2D models is presented in this section. The procedure is explained in the context of single-lobe progressing cavity pumps. Its application may be extended to any pump or motor configuration.

The approximate path of the centre of the rotor within a typical single-lobe stator cross section is shown in Figure 5.31. The motion consists primarily of a sinusoidal lateral translation of amplitude L_{major}. The equilibrium force balance also induces a translation L_{minor} perpendicular to the lateral translation. The resulting path is elliptical in shape. Further description of the rotor path may be found in the loading discussion in Section 5.3.

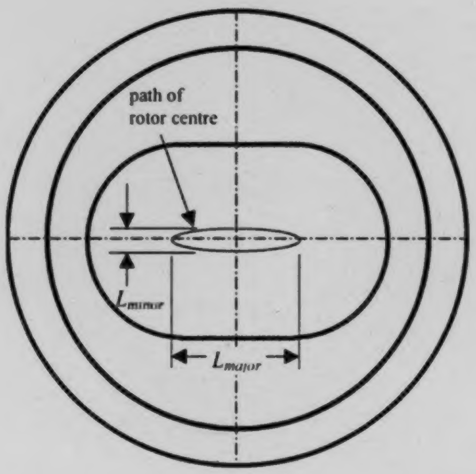

Figure 5.31. Path of rotor centre in 2D cross-section of single-lobe pump.

The position of the rotor at rest within the stator is such that the relative position of the rotor and stator in cross-sections along the axial length of the pump follow the elliptical path shown in Figure 5.31. Figure 5.32 shows sequential cross-sections spaced at one-quarter of the rotor pitch. Note that the sum of the lateral and perpendicular translations, L_{major} and L_{minor}, is equal to the major diameter of the rotor.

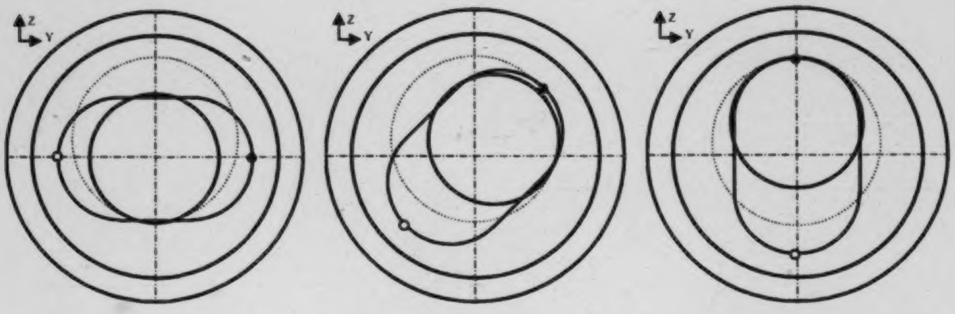

(a) Axial position = 0 (b) Axial position = ¼*P_{rotor} (c) Axial position = ½*P_{rotor}

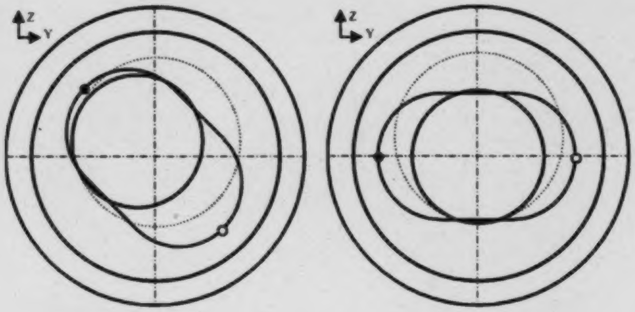

(d) Axial position = ¾*P_{rotor} (e) Axial position = P_{rotor}

Figure 5.32. Cross-sections of single-lobe pump taken at various points along the length of the pump, shown relative to the global Y and Z axes. P_{rotor} is the rotor pitch.

An approximation to the orientation of forces in the 3D geometry can be obtained by performing a rotation and summation of the forces applied to the rotor by the stator obtained using the standard 2D analysis technique. The calculated out-of-balance force from a representative length of rotor is used as a convergence criterion for the iterative solution procedure described below.

Figure 5.33 describes the iterative loop for obtaining the equilibrium rotor position using 2D generalised plane strain models. The initial structural analysis is conducted without an eccentricity offset. The net force applied to the rotor at each rotor position is extracted from FEA results and is rotated to a global axis system. The sum of the forces at each rotor position in this global axis system is used as the convergence criterion for the loop. For the first loop, the out-of-balance force is much greater than the tolerance. An eccentricity offset is introduced and modified with each successive iteration until the out-of-balance force on the rotor is less than the tolerance value. The final eccentricity offset provides a description of the equilibrium rotor path.

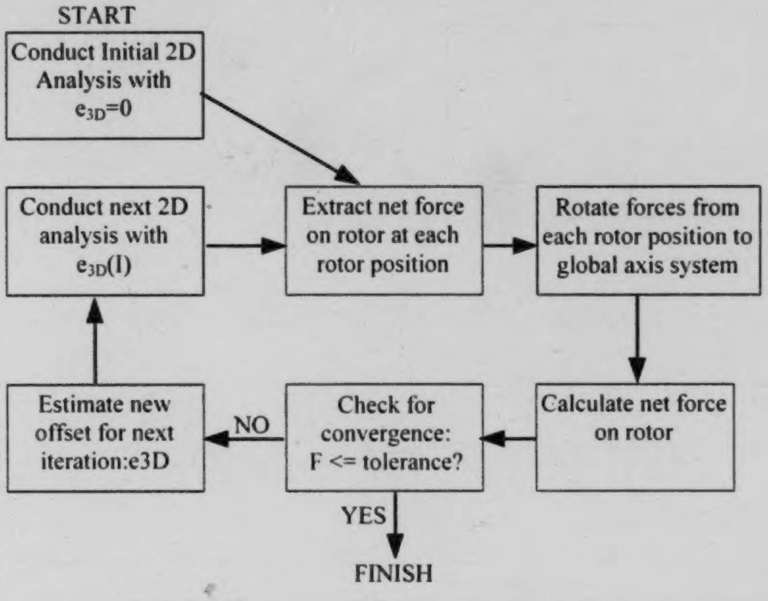
START
Conduct Initial 2D Analysis with e_{3D}=0
Conduct next 2D analysis with $e_{3D}(I)$
Extract net force on rotor at each rotor position
Rotate forces from each rotor position to global axis system
Estimate new offset for next iteration:e3D
NO
Check for convergence: F <= tolerance?
Calculate net force on rotor
YES
FINISH

Figure 5.33. Flowchart of iterative procedure used for determining equilibrium rotor position using 2D models.

Comparisons between the rotor positions determined using the 2D iterative procedure and those from corresponding 3D models are discussed in Section 5.6.

5.6 Structural Analysis Comparisons

Comparison of results obtained from two-dimensional models with those obtained from three-dimensional models is an important verification step of the 2D modelling strategy. While the 3D models provide a more accurate representation of the stator and rotor geometries and the relevant structural analysis results, the computational power required to conduct extensive parametric 3D analyses is prohibitive. As a result, the 3D models are most useful for benchmarking 2D models for thermomechanical analyses.

Ideally, a satisfactory two-dimensional model provides results that match those from the three-dimensional model at the source of the 2D approximation. It was expected that it would be difficult to obtain this type of agreement between the 2D and 3D stator analyses for the following reasons:

1. The helical contact surfaces formed by the rotor and stator geometry create out-of-plane deformation in the vicinity of the contact region; and
2. Differential pressure loads do not act in the plane of the cross-section, but rather at an angle associated with the helix angle of the stator.

Specific goals of the comparison process are to:

1. Quantify errors in the heat generation field created by the existing 2D modelling approximation; and
2. Formulate a modified method of using the 2D models to provide as close an approximation as possible to three-dimensional behaviour.

Comparisons between 2D and 3D models are performed so that the effect of the two-dimensional approximation to the 3D geometry may be quantified for heat generation results. The development of a general method of relating 2D structural results to 3D models is a complex process and is not thought to be critical to the study at hand if an energy criterion provides a suitable comparison criterion.

5.6.1 Energy comparison criterion

Comparisons of the distortional strain energy present in static 3D models and corresponding 2D models are used as an indication of how well the hysteresis energy generation fields correlate. In most cases, the hydrostatic component of the strain energy is negligible compared to the distortional component. The hydrostatic strain energy is somewhat sensitive to errors in field variables created by discretisation of the stator geometry. The near-incompressibility of the elastomer means that small errors in the calculated hydrostatic strain can translate into large errors in hydrostatic strain energy. Hence, only the distortional component of the energy is used for comparison purposes.

While the distortional strain energy does not vary directly with the hysteresis energy (Section 6.1), it is calculated from the same parameters (deviatoric stresses and strains). The rate-dependent (dynamic) component of the total strain energy defines the hysteresis energy losses. It is assumed that if the static strain energies obtained from 2D and 3D models correlate, the energies lost to rate-dependent effects will also correlate. The distortional (deviatoric) stresses τ_{ij}^{dev} and the components of Cauchy stress τ_{ij} are defined by

$$\tau_{ij}^{dev} = \tau_{ij} - \delta_{ij} \cdot \frac{\tau_{kk}}{3} \qquad [5.14]$$

at any point in the elastomer. The total static distortional strain energy density, U'', is calculated from the deviatoric components of the Cauchy stress and true strain (τ_{ij}^{dev} and ε_{ij}) as

$$\begin{aligned} U'' &= \frac{1}{2} \cdot (\tau_{11}^{dev} \cdot \varepsilon_{11} + \tau_{12}^{dev} \cdot \varepsilon_{12} + \ldots + \tau_{33}^{dev} \cdot \varepsilon_{33}) \\ &= \frac{1}{2} \tau_{ij}^{dev} \cdot \varepsilon_{ij} \end{aligned} \qquad [5.15]$$

The strain energy from static structural FEA models is the best available indicator of the dynamic hysteresis energy in the elastomer aside from a full three-dimensional heat generation analysis.

The hysteresis energy tools developed for this investigation are not designed for the three-dimensional model and cannot be easily modified to perform this task.

5.6.2 Comparison cases

Two sets of comparisons are presented so errors due to rotor/stator interference and errors due to differential pressure loading can be assessed separately. A conventional single-lobe pump with representative rotor and stator geometries is used for interference comparisons. Differential pressure comparisons are conducted without the rotor.

The pitch length associated with the helical geometry may be varied in an attempt to relate 2D and 3D analysis results. Two parameters are used to characterise the helix in this discussion. The helix angle relates the pitch length of the helix to the eccentricity and is defined by

$$Helix\ Angle(^\circ) = \arctan\left[\frac{\pi \cdot (D_{rotor}^{major} - D_{rotor}^{minor})}{P_{rotor}}\right] \cdot \frac{360}{2\pi} \qquad [5.16]$$

where: D_{rotor}^{major} is the major diameter of the rotor;

D_{rotor}^{minor} is the minor diameter of the rotor; and

P_{rotor} is the rotor pitch length.

The pitch-to-diameter ratio (p/d ratio) provides a similar nondimensional parameter and is defined by

$$p/d\ ratio = \frac{P_{rotor}}{D_{rotor}^{minor}} \qquad [5.17]$$

Table 5.1 shows a list of the analyses conducted for this comparison task. The 3D models all have the same cross-sectional geometry as the 2D model. By varying the p/d ratio parametrically over a representative range of 1.85 to 5.56 for PCPs, the effect of the helix angle on the structural response of the stator may be observed. An interference analysis with a p/d ratio of 0.93 is also included. Each 3D geometry is used for an interference analysis and a differential pressure analysis. For differential pressure analyses, the applied cavity pressure is 0.31 MPa (45 psi).

Case Number	Model Type	Stator Major Diameter (mm)	Stator Half Pitch Length (mm)	Helix Angle (degrees)	p/d ratio	Applied Differential Pressure (MPa)
1	2D plane strain	60.91	N/A	N/A	N/A	0
2						0.31
3	3D		35.00	44.50	0.93	0
4	3D		70.00	26.17	1.85	0
5	3D		70.00	26.17	1.85	0.31
6	3D		140.00	13.80	3.71	0
7	3D		140.00	13.80	3.71	0.31
8	3D		210.01	9.30	5.56	0
9	3D		210.01	9.30	5.56	0.31

Table 5.1. Comparison analysis cases.

5.6.3 Rotor position for rotor/stator interference cases

For 3D models, the equilibrium position of the rotor within the stator is found using the boundary condition strategy described in Section 5.4.4. Figure 5.34 shows the eccentricity offset (e_{3D}) obtained for each 3D analysis case. The eccentricity offset value used for the 2D analysis scenario is based on the equilibrium rotor position determined from the equilibrium position procedure for 2D models described in Section 5.5. In this section, the planar (i.e., 2D) rotor path defined by this eccentricity offset value is referred to as the "forcebalance" path.

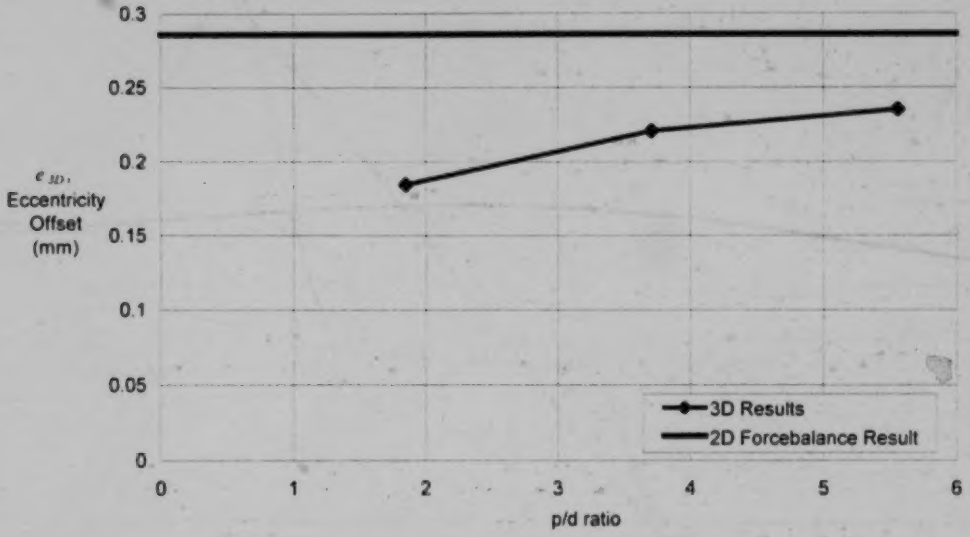

Figure 5.34. Equilibrium position variations with pitch length.

Figure 5.34 shows that the eccentricity offset, e_{3D}, is dependent on the pitch length of the stator. As the pitch length increases, the eccentricity offsets observed in the 3D models approach the 2D plane strain result. This trend is encouraging because the plane strain case corresponds to a stator with infinite pitch length.

The rotor path represented by the eccentricity offset values discussed above is elliptical in shape. For this reason, the rotor/stator interference changes as the eccentricity offset changes. Figure 5.35 shows the rotor/stator interference that occurs at the 0° rotor position (minor seal) and the 90° rotor position (major seal) for each of the 3D analyses and the 2D plane strain analysis. The figure shows that for the major seal and both the high and low-interference sides of the minor seal, the interference from 3D models approaches that obtained from the 2D equilibrium position procedure as the p/d ratio of the pump increases. The error in using the predicted equilibrium position (from the 2D models) to estimate the minor interference is as much as 22% for the short-pitch pump. This maximum error decreases to approximately 12% for the pump with the highest p/d ratio considered.

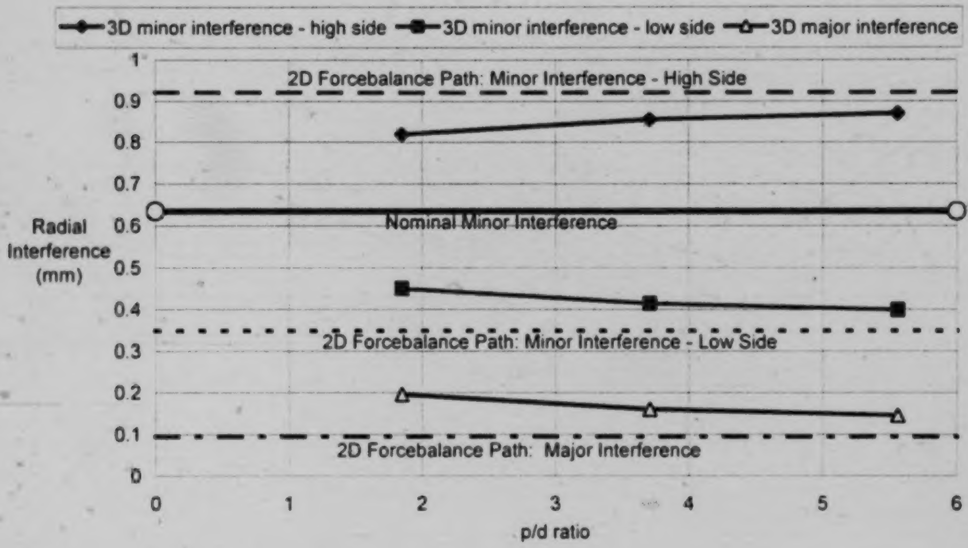

Figure 5.35. Rotor/stator interference at the 0° and 90° rotor position for interference comparison models.

5.6.4 Energy comparisons for rotor/stator interference cases

Significant differences exist between strain energy results for 2D and 3D models of single-lobe pumps under rotor/stator interference loads. Comparisons of strain energy in the various models are conducted using two methods: the strain energy density at specific points in the stator cross-section, and the total strain energy in the cross-section.

5.6.4.a Pointwise energy comparisons

Pointwise strain energy comparisons are conducted at points A and B in the elastomer shown in Figure 5.36. These points are used because they are in the vicinity of the stress concentration caused by rotor/stator interference when the rotor is at the 0° position. Figure 5.5 shows an example of the stress distribution in a single-lobe pump.

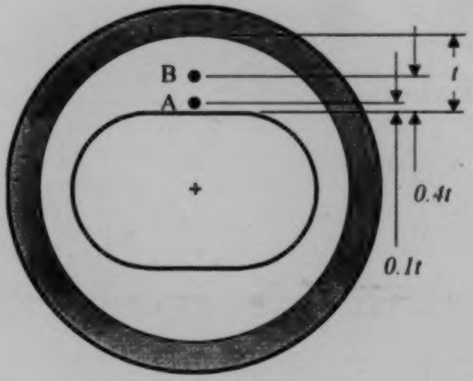

Figure 5.36. Points used for pointwise energy comparisons.

It is helpful to quantify the contributions of different components of stress and strain to the strain energy density. The contribution of strain energy density from stresses and strains acting in the global X direction is

$$U_{XX}'' = \frac{1}{2} \cdot (\tau_{XX}^{dev} \cdot \varepsilon_{XX}) . \qquad [5.18]$$

The contributions of distortional strain energy density at point A with the rotor positioned at 0° are shown as a function of p/d ratio in Figure 5.37. Also shown are the total distortional strain energy density at this point from the 3D models and the total distortional strain energy density for the 2D plane-strain model. The error in the distortional strain energy from the 2D model is approximately 40% at a p/d ratio of 1.5, which is considered to be a practical lower p/d ratio limit for single-lobe pumps. As the p/d ratio increases, the energy density from the 3D model approaches that of the 2D plane-strain model. The axial contribution of strain energy density (U_{XX}'') shows a strong correlation with the error in total strain energy density between 2D and

3D models. This is not surprising given the absence of axial strain energy present in the 2D plane strain results.

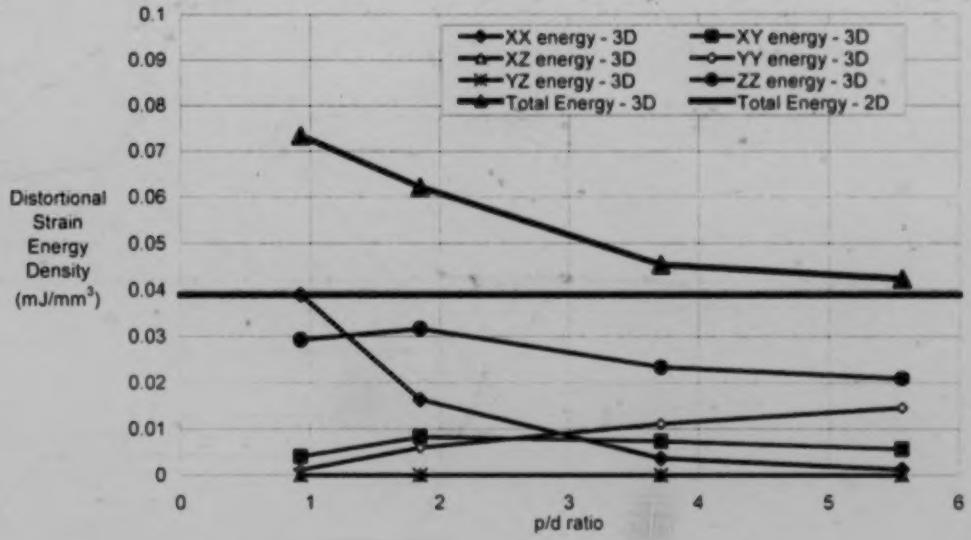

Figure 5.37. Contributions of distortional strain energy at point A as a function of p/d ratio with the rotor positioned at 0°.

A more complete understanding of the variations in pointwise strain energy density may be obtained by tabulating the strain energy density at points A and B for a number of axial positions in the 3D models. This provides an indication of how the energy at each point varies as the rotor rotates within the stator. Figure 5.38 and Figure 5.39 show the strain energy density at points A and B as a function of the rotor position within the cross-section. While the magnitude of the energy density observed at both points decreases significantly as the rotor moves from the 0° position (minor seal) to the 90° position (major seal), the error in the 2D strain energy density remains significant. The variations in energy density with p/d ratio observed at point A are opposite to those at point B. This suggests that the strain energy distribution changes with the p/d ratio.

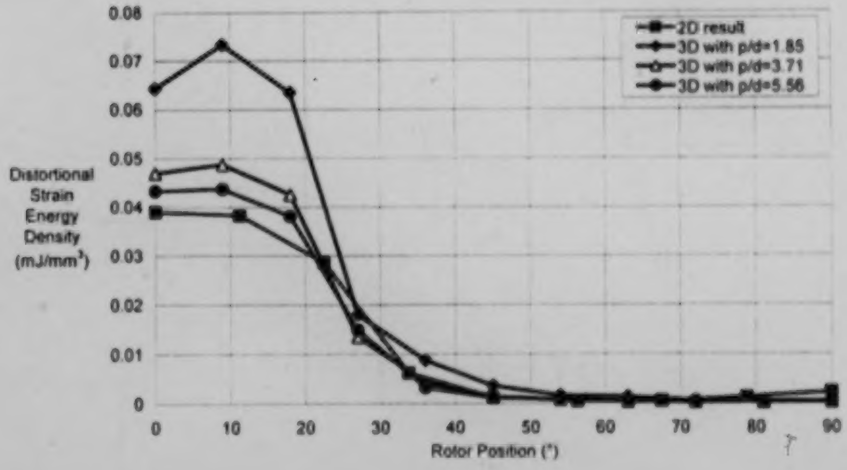

Figure 5.38. Distortional strain energy density comparison at point A as a function of rotor position.

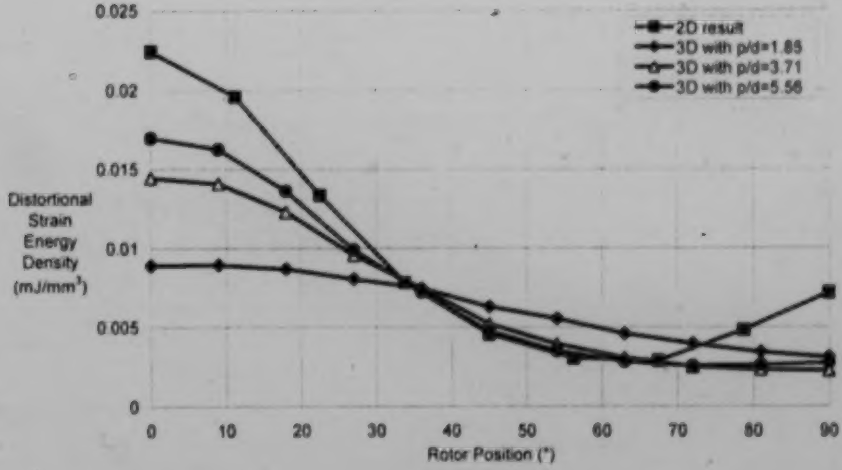

Figure 5.39. Distortional strain energy density comparison at point B as a function of rotor position.

5.6.4.b Planar energy comparisons

The second method of comparing strain energy in the stator provides a better indication of the overall strain energy response of the stator than do the pointwise comparisons. The strain energy density is integrated over the area of the cross-section to find the total strain energy per unit length of stator. The total distortional strain energy per unit length with the rotor at the 0° position for three 3D models and the two-dimensional plane strain model is shown in Figure 5.40.

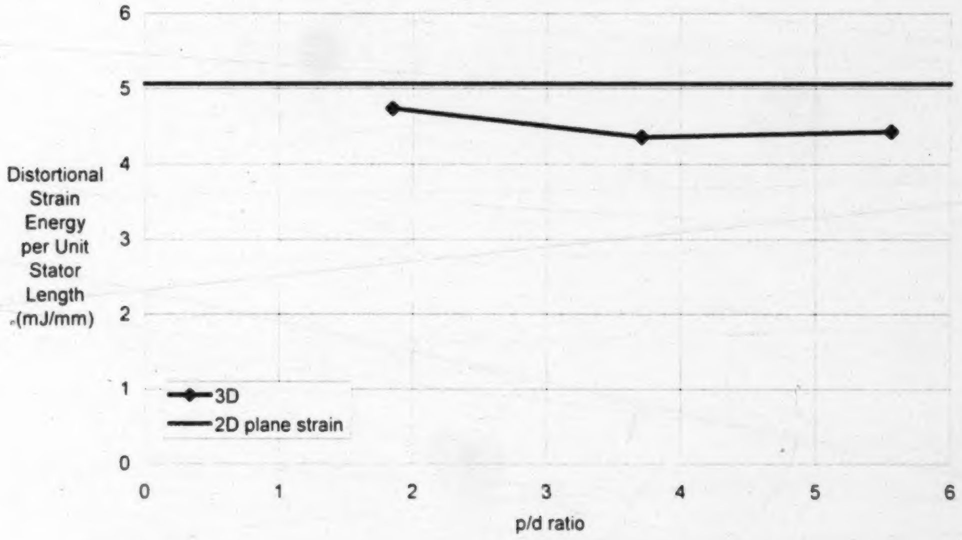

Figure 5.40. Cross-sectional energy density integral with rotor at 0° position.

The planar strain energy generated with the rotor at 0° for the 2D plane strain model overestimates the strain energy in all three three-dimensional models. This result is opposite to the results of the pointwise comparisons discussed in the preceding paragraphs. Results at the 0° rotor position did not provide any obvious relationship between p/d ratio and planar energy. Like the pointwise energy calculations, the planar energy calculations may be done with the rotor at a number of different positions in its rotational path. Figure 5.41 shows the planar strain energy values as a function of rotor position for the three-dimensional models and for two-dimensional models with and without the eccentricity offset determined using the 2D equilibrium procedure discussed in Section 5.5. Results from the 2D analysis without the eccentricity offset (i.e., e_{3D}=0) show peak errors in excess of 400%. Energies obtained from the 2D equilibrium plane strain model are on the order of 20% more than the 3D results when the rotor is not in contact with the major diameter of the stator (i.e., rotor position 0° to 70°). As the rotor approaches the stator major diameter (90° position), the cross-sectional energy from the 2D model is up to twice that observed from 3D results. The 3D models show that the cross-sectional strain energy is greater for longer pitch pumps (i.e., higher p/d ratio) when the rotor approaches the major diameter (90 degrees). No strong trend with p/d ratio is apparent with the rotor at the minor diameter.

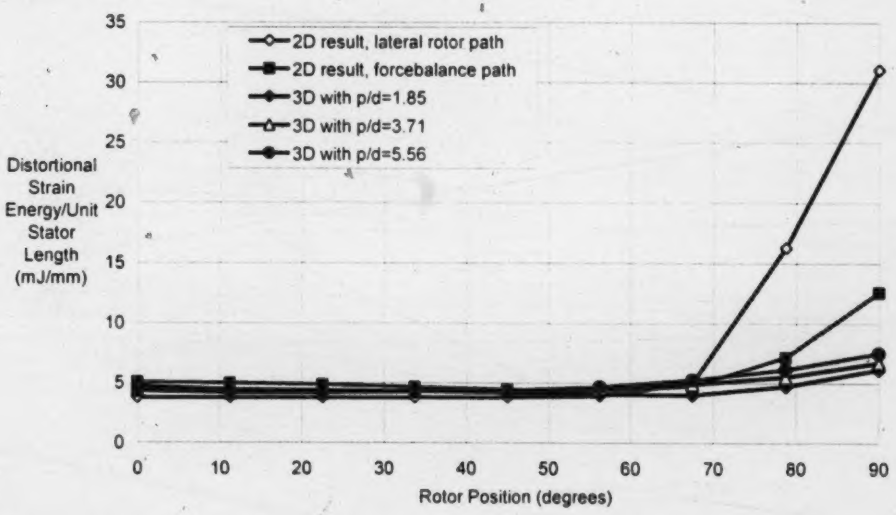

Figure 5.41. Planar energy comparison for 2D and 3D models for interference loading case.

The above comparison provides an indication of the validity of the existing two-dimensional plane strain analysis approach. By accounting for the eccentricity offset in the path of the rotor, a conservative approximation to the heat generation may be achieved. This is the second of three goals outlined for the 2D/3D model comparisons.

The variability observed in the pointwise and planar energy comparisons prompted a more detailed investigation of the factors that govern the stator response in three-dimensional models. The primary finding of this investigation is that the stiffness of the stator elastomer in the 2D models was substantially higher than the 3D stiffness. Approximate stiffness may be determined by dividing the rotor reaction force by the net rotor/stator interference. Figure 5.42 shows the approximate stiffness at the 90 degree and 0 degree locations (major and minor seal locations, respectively) as a function of p/d ratio. The net rotor/stator interference at the 0° position is equal to twice the eccentricity offset, e_{3D}. The 2D model overestimates the stiffness by as much as 86% at this point. The stiffness at the 90° position is overestimated by between 250% and 450%. These results show that the 2D plane strain approximation generates more confinement within the elastomer than is actually present.

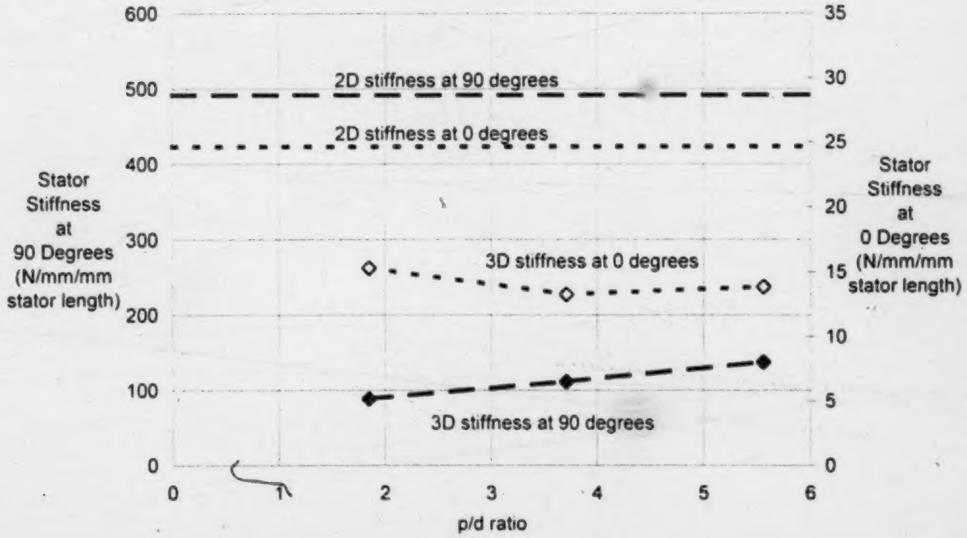

Figure 5.42. Stator stiffness comparison at major diameter.

5.6.5 Modified 2D analysis approach

The errors in stiffness observed in Figure 5.42 form the basis for a modified two-dimensional structural analysis approach. The goal of this approach is to generate 2D analysis results that are more representative of those that occur in the three-dimensional models than those obtained from the existing 2D analysis procedure. The analysis approach requires characteristic stiffness curves (such as the one shown in Figure 5.42) from at least two three-dimensional stator models.

The improved two-dimensional analysis technique consists of creating a modified rotor path for two-dimensional plane strain analyses based on stiffness comparisons at two rotor/stator contact points. The net interference at the 0° rotor position is reduced so the overall rotor/stator contact force is comparable to that seen in the 3D models. Since the net interference at the 0° rotor position is equal to twice the eccentricity offset (e_{3D}), the applied eccentricity offset is multiplied by a factor corresponding to the ratio of the 3D stiffness to the 2D stiffness. A similar approach is taken at the 90° rotor position. The interference at the 90° position (major seal) is reduced so the net reaction corresponds to the 3D reaction force. Figure 5.43 compares the cross-sectional strain energy integral of the modified 2D model with the 3D results and the original 2D analysis result. The modified rotor path is determined from the stiffness comparison between the 2D model and the 3D model of the short pitch pump (p/d=1.85). While there is still a discrepancy between the 2D modified path result and 3D result, the modified path provides a better approximation than the forcebalance path.

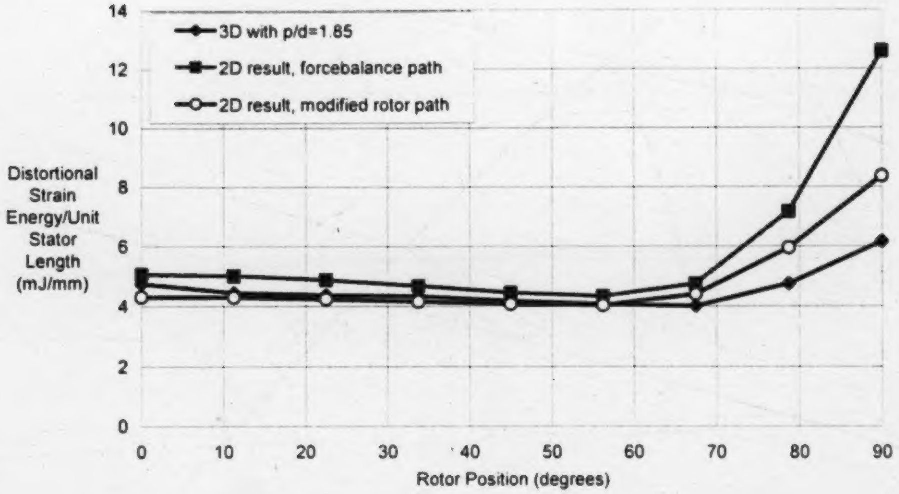

Figure 5.43. Planar energy comparison for modified rotor path model for interference loading case.

Figure 5.44 shows contour plots of distortional strain energy for the modified 2D model and the 3D model with p/d ratio of 1.85 at the 0° rotor position. The distribution of strain energy density is clearly concentrated nearer to the inner elastomer profile for the short pitch (p/d=1.85) pump than for the 2D model. The long-pitch pump and 2D model show much closer agreement as might be expected.

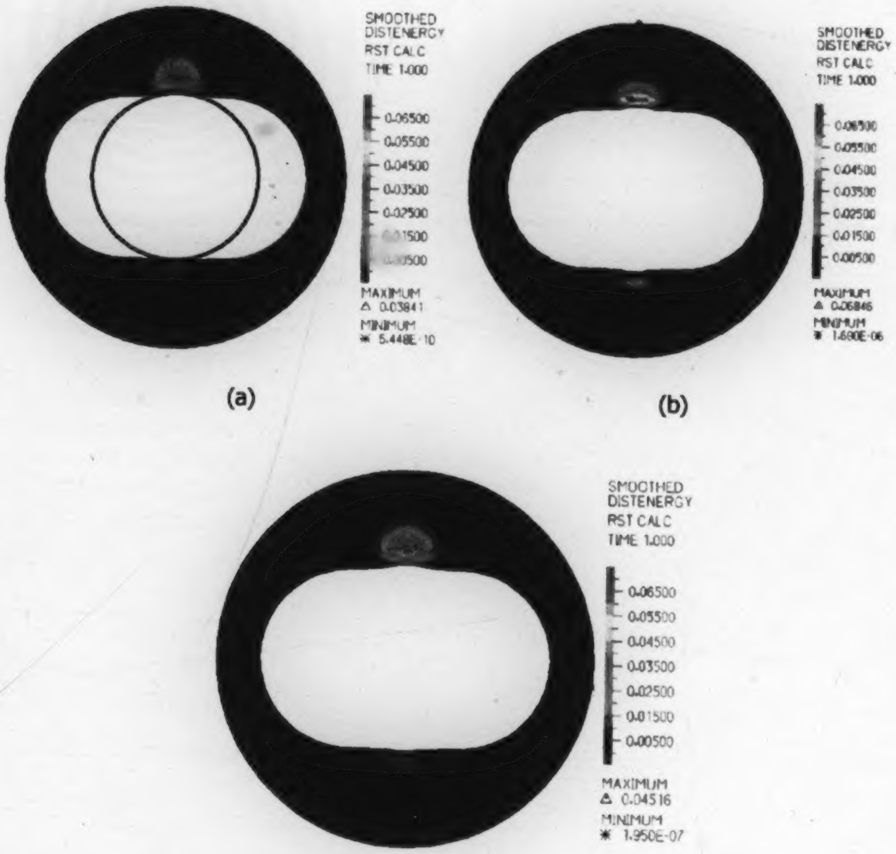

(a) (b)

(c)

Figure 5.44. Contour plots of distortional strain energy density for (a) modified 2D model, (b) 3D model with p/d=1.85, and (c) 3D model with p/d=5.56 at rotor position 0°. (All units in mJ/mm³)

Figure 5.45 shows the planar strain energy density distribution for the modified 2D model and 3D models with the rotor at the 90° position. While significant differences exist in the energy distribution, the bulk of the strain energy is concentrated in the vicinity of the top and bottom of the rotor in all cases.

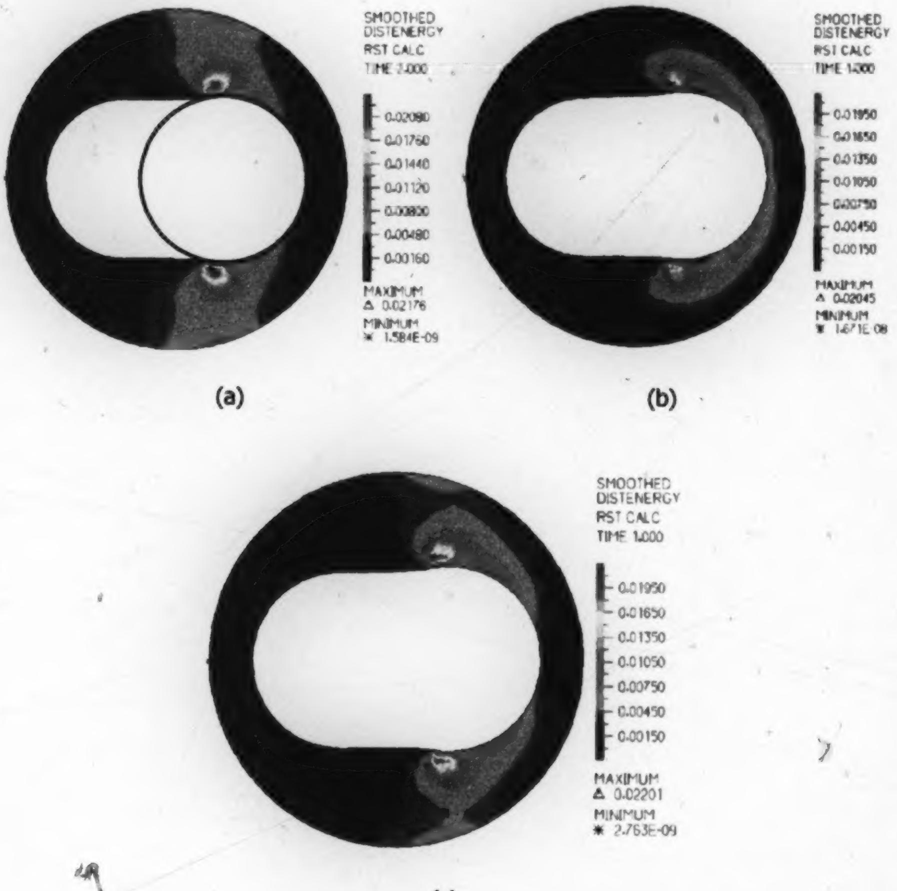

(a)

(b)

(c)

Figure 5.45. Contour plots of distortional strain energy density for (a) modified 2D model, (b) 3D model with p/d=1.85, and (c) 3D model with p/d=5.56 at rotor position 90°. (All units in mJ/mm³)

The 2D model with the modified rotor path provides better agreement with 3D results than the original 2D model. The modified 2D method of analysis requires the use of 3D models to provide a relative stiffness comparison so the rotor path may be adjusted accordingly. Depending on the level of accuracy required from the analysis, the errors in results obtained from the original 2D model (using the equilibrium position procedure described in Section 5.5) may be acceptable. 2D results provide a better approximation to 3D results for long-pitch pumps.

A more global understanding of the errors in the 2D strain energy approximation can be obtained by averaging the strain energy from equally spaced cross-sections through one rotor pitch. Table 5.2 lists the results of these comparisons. The 2D analysis with the modified rotor provides total strain energy values within 7% for all three three-dimensional pump models.

Analysis Model	Average Energy (mJ/mm)	2D errors (%)	
		forcebalance path	modified rotor
2D forcebalance path	5.883	N/A	N/A
2D modified rotor	4.870	N/A	N/A
3D, p/d=1.85	4.563	28.9	6.7
3D, p/d=3.71	4.803	22.5	1.4
3D, p/d=5.56	5.038	16.8	-3.3

Table 5.2. Errors in average strain energy for 2D approximations to 3D models.

5.6.6 Results of differential pressure comparisons

Differential pressure comparisons are conducted using the same approach used for the interference comparisons. Analyses are conducted at representative differential pressures for a single-lobe pump geometry with p/d values ranging from 1.85 to 5.56. Significant differences can be observed between the responses of the 2D and 3D models.

Figure 5.46 and Figure 5.47 show the distortional strain energy density at points A and B in the stator elastomer (see Figure 5.36) as a function of the rotor position (θ) for three 3D models and the 2D plane strain model. The applied differential pressure for these cases was 0.31 MPa.

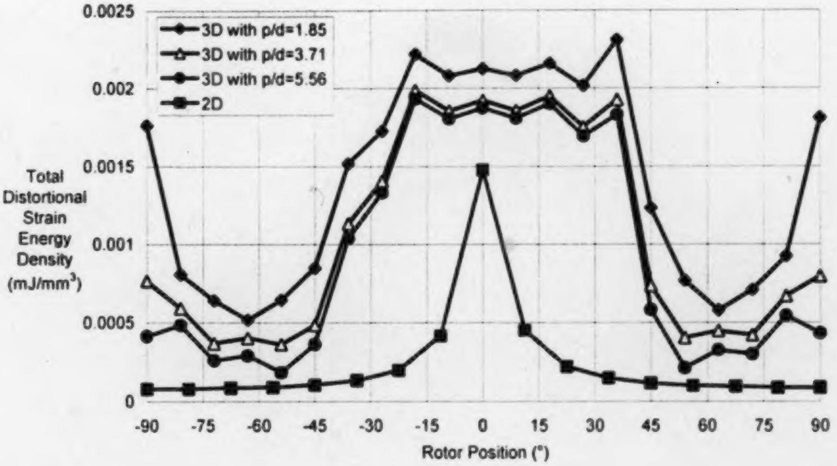

Figure 5.46. Strain energy density at point A with 0.31 MPa differential cavity pressure.

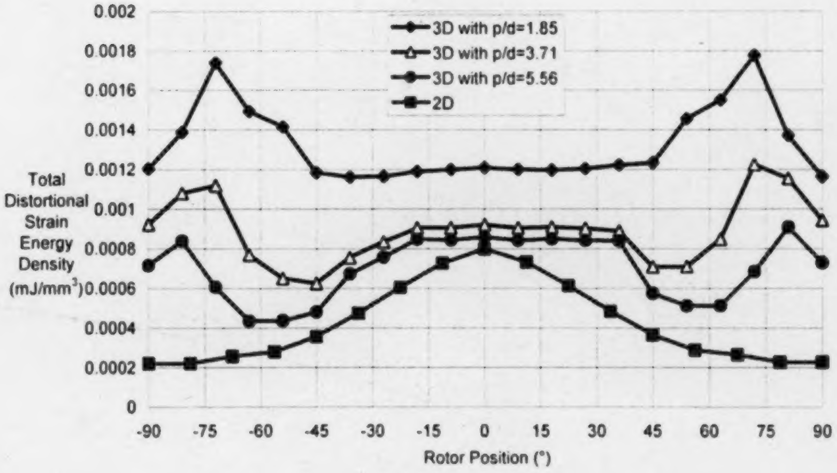

Figure 5.47. Strain energy density at point B with 0.31 MPa differential cavity pressure.

The pointwise energy comparisons indicate that there is a discrepancy between the response of the 2D approximation to the pump and the 3D models for all p/d ratios analysed. The long pitch 3D model (high p/d ratio) provides results that were closest to the 2D models.

Planar energy comparisons are performed to get an indication of the global response of the models to differential pressure loading. Figure 5.48 shows that the distortional strain energy per unit axial length of stator is underestimated by the 2D model at all rotor positions for all three pitch lengths analysed.

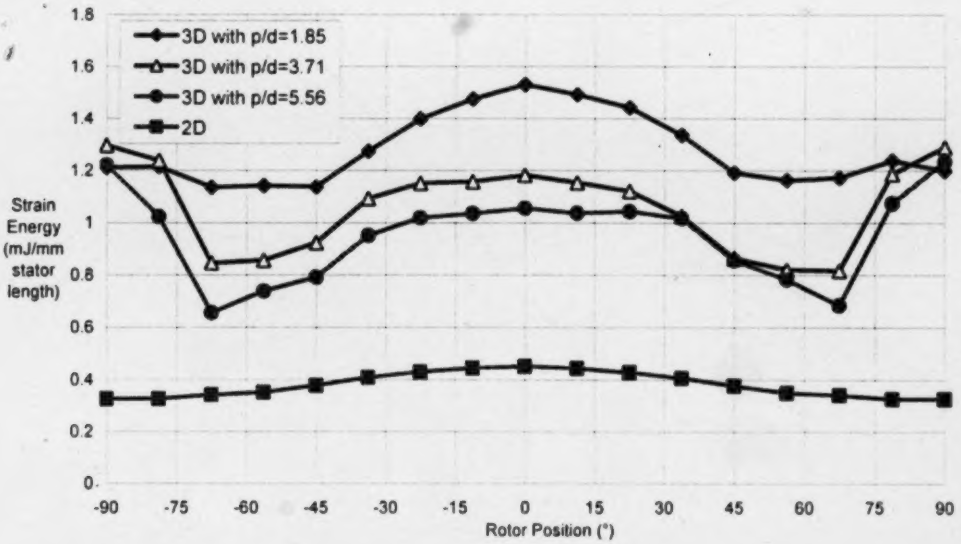

Figure 5.48. Planar energy comparison for 2D and 3D models for differential pressure loading case.

The 2D model clearly underestimates the strain energy generated by the applied differential pressure load. The planar energy from the 2D approximation is an average of 60% of the energy in the long-pitch pump model. This error increases to about 70% for the short pitch pump model.

Figure 5.49 and Figure 5.50 show contour plots of distortional strain energy for the various 3D models and the 2D model at a differential pressure of 0.31 MPa. While the magnitude of the strain energy is drastically different, the cross-sectional energy distribution is similar. A general method of relating 3D results to the associated 2D model may be possible given the results of representative 3D analyses.

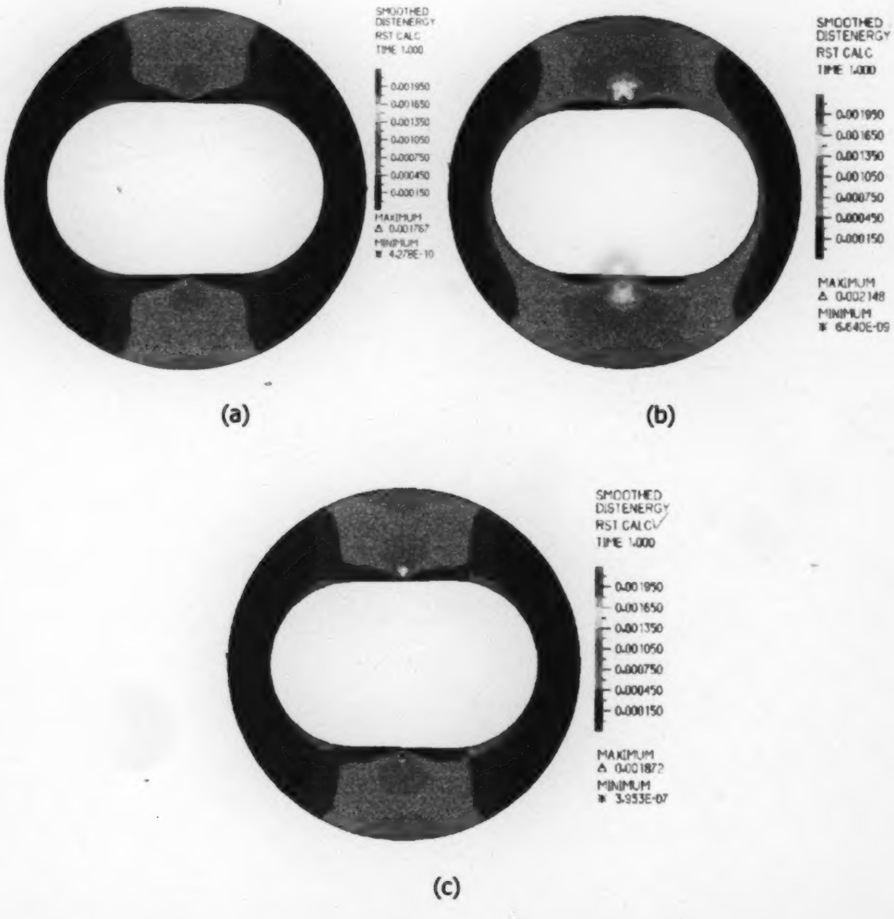

(a) (b)

(c)

Figure 5.49. Contour plots of distortional strain energy density for (a) 2D model, (b) 3D model with p/d=1.85, and (c) 3D model with p/d=5.56 with rotor at 0° position, differential pressure 0.31 MPa. (All units in mJ/mm³)

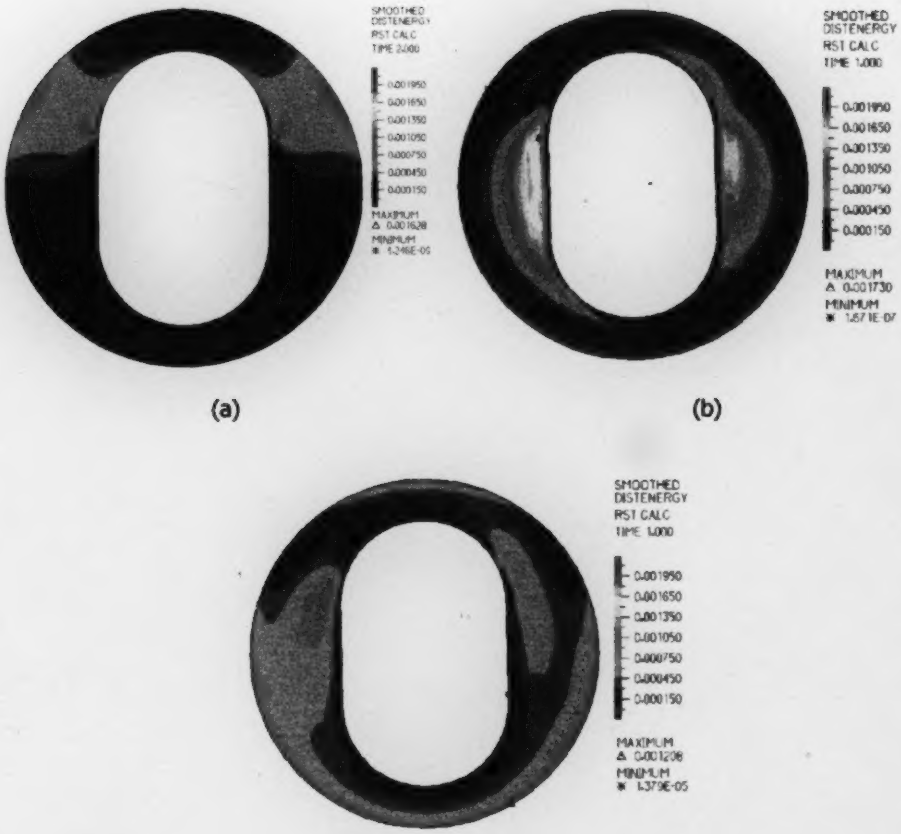

(a) (b)

(c)

Figure 5.50. Contour plots of distortional strain energy density for (a) 2D model, (b) 3D model with p/d=1.85, and (c) 3D model with p/d=5.56 with rotor at 90° position, differential pressure 0.31 MPa. (All units in mJ/mm^3)

The energy generated by differential pressure loads increases approximately quadratically with the magnitude of the applied pressure. The strain energy varies linearly with the stress and the strain, both of which appear to increase linearly with pressure. Figure 5.51 shows a comparison of the planar strain energy at differential pressures of 0.155 MPa and 0.310 MPa for the short pitch (p/d 1.85) pump model. The increase in strain energy with a doubling of the applied differential pressure is a factor of between 3.98 and 4.02.

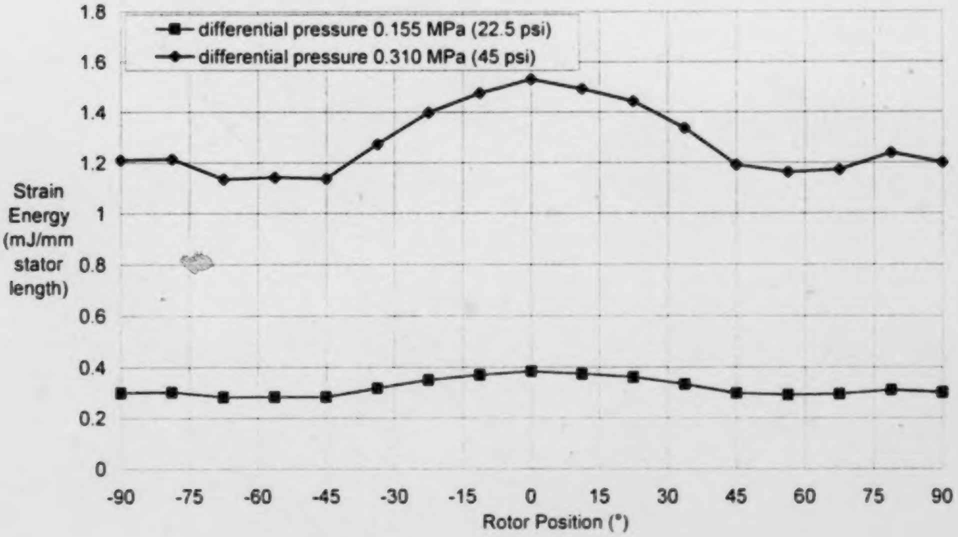

Figure 5.51. Planar strain energy comparison for short-pitch 3D model at differential pressures of 0.155 MPa and 0.31 MPa.

The 0.31 MPa (45 psi) differential pressure used for comparisons is on the high end of the range of differential cavity pressures that are typically seen in a conventional single-lobe PC pump. The magnitude of the total strain energy resulting from this differential pressure is between 20% and 30% of the strain energy generated by typical rotor/stator interferences for the pump model analysed. A lower pressure will reduce the magnitude of this contribution because the strain energy contributed by the pressure load varies with the square of the applied pressure. Figure 5.52 shows the ratio of pressure strain energy to interference strain energy for a range of differential pressures for the short pitch pump with a standard interference rotor.

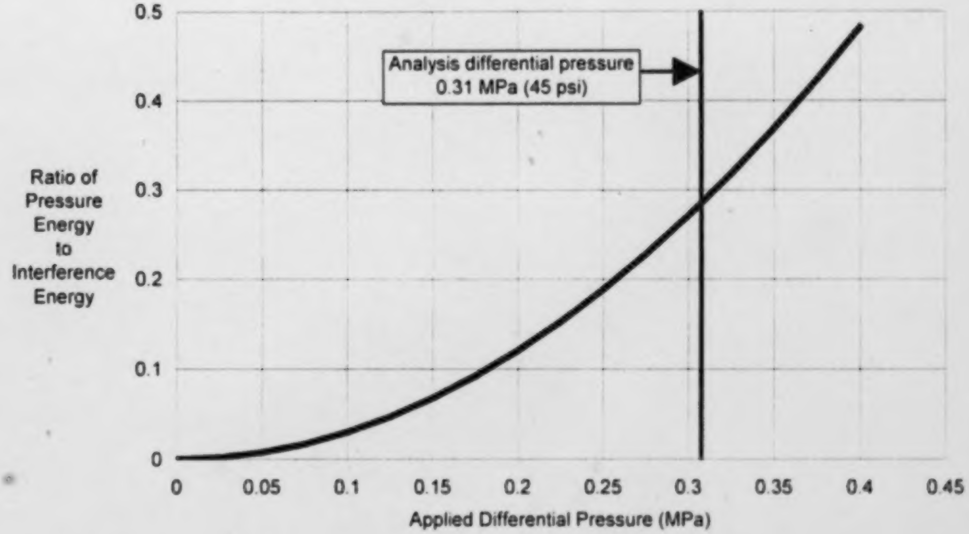

Figure 5.52. Relative contributions of pressure and interference energy as a function of applied differential pressure for 3D model with p/d=1.85.

A combined 3D analysis with interference and pressure loading provides an opportunity to investigate the effect of applying the two loading types simultaneously. Figure 5.53 shows the variation in the planar energy integral for the interference, pressure, and combined loading scenarios. Also shown on the figure is the sum of the pressure and interference energies. For one half of the rotor's cycle, it appears that analysing the two loading cases separately provides an overestimate of the strain energy seen in the combined loading case. For the other half, a sum of energies from the individual cases underestimates the combined load energy. The interference and pressure loads likely act together to deform the elastomer for one part of the cycle and oppose each other for the other part of the cycle. The average energy input for the entire rotor cycle in the combined loading case is overestimated by approximately 5% by adding the energy components from pressure and interference loads.

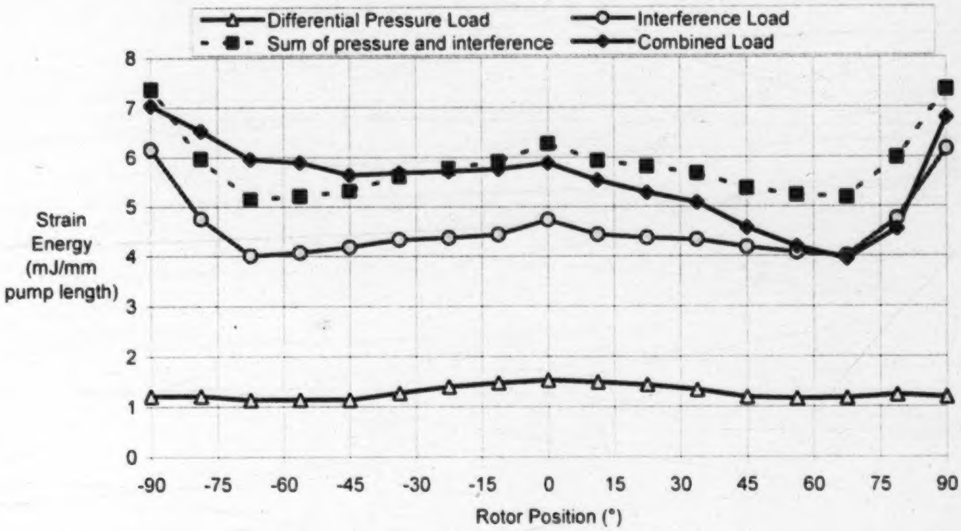

Figure 5.53. Planar energy comparison for pressure, interference and combined load 3D analysis cases.

The errors observed in the response of 2D and 3D models to differential pressure loads point to a need for further work to identify how a better estimate of the response to differential pressure can be obtained from 2D models for heat generation purposes. The errors in strain energy due to differential pressure loads do not affect the discussion or sample results presented in the remainder of this document. Verification testing (discussed in Chapter 9) was conducted without differential pressure loads. An improved 2D differential pressure modelling strategy could be used in conjunction with the thermomechanical modelling strategy described herein to understand the contribution of differential pressure loads to hysteresis heat generation within the elastomer.

5.6.7 Summary of comparisons

The use of two-dimensional models to approximate the 3D geometry of single-lobe pumps is an efficient method of understanding the response of PCPs and PDMs in the context of heat

5.6.7 Summary of comparisons

The use of two-dimensional models to approximate the 3D geometry of single-lobe pumps is an efficient method of understanding the response of PCPs and PDMs in the context of heat generation. These efficient models constitute an important part of the thermomechanical solution procedure outlined in Chapter 8, which requires several structural finite element solutions to find the stabilised operating temperature of the pump or motor.

Errors introduced by the 2D approximation to the 3D geometry under rotor/stator interference and differential pressure loads appear to be dependent on the p/d ratio of the stator. In general, 2D models of long-pitch stators show better agreement with 3D models than do 2D models of short-pitch stators. The generalised plane-strain assumption used in 2D modelling prevents localised out-of-plane deformations and tends to increase the apparent stiffness of the stator to indentation by the rotor.

A modified rotor path may be used for 2D models to ensure better agreement with 3D response to rotor/stator interference loads. The elliptical rotor path defined by the equilibrium position procedure described in Section 5.5 provides better agreement with 3D results than a purely lateral path but may still result in errors of over 20% in the planar strain energy. An alternate rotor path based on a comparison of the stiffness of the stator in 2D and 3D models improves the agreement between 2D and 3D total strain energy results to within 7% for short-pitch stators.

Two-dimensional models significantly underestimate the amount of strain energy induced in the elastomer by differential pressure, largely because the out-of-plane component of displacement is not accounted for. In most cases, the heat generated in the elastomer from differential pressure loads will be small compared to the heat generated through interference loads. Further work is required in order to formulate a method of obtaining accurate differential modelling results for short-pitch pumps using 2D models.

6 HEAT GENERATION MODELLING

One of the key elements of the thermomechanical solution strategy outlined in Chapter 4 is a method of quantifying the heat generated within the stator elastomer. This heat results from viscous losses in the elastomer as the stator is cyclically loaded by the rotor. The amount and distribution of heat generated depends on the stress and strain fields in the elastomer, speed and lobe configuration of the pump or motor, and dynamic elastomer properties. The selected heat generation modelling strategy uses results of incremental static structural analyses and available dynamic material properties to produce results that are compatible with the thermal modelling strategy described in Chapter 7.

6.1 General Heat Generation Considerations

The viscoelastic response of elastomers in dynamic loading situations is well documented.[3,7,21,23] Their response includes an elastic component similar to the pre-yielding behaviour of metals and a viscous component that can be compared to the flow losses generated by viscous fluids. Viscoelastic material models typically represent response as a combination of spring and dashpot elements to describe the elastic and viscous components of the elastomer response. The viscous component of this response results in a loss of energy within the elastomer as the elastomer is cyclically loaded. The thermo-mechanical analysis strategy created for this study assumes that all energy generated due to viscous losses within the elastomer is released to the elastomer in the form of heat.

6.2 Material Considerations (Heat Generation)

Dynamic elastomer material properties that relate the viscous response to the elastic response are required in order to quantify the viscoelastic response of a material. The behaviour of rubber compounds has been shown to vary greatly with the various fillers that are typically used to modify the response of rubber compounds. Given that a wide range of elastomers are used in PCP and PDM applications, a general approach to quantifying elastomer response based on available material testing techniques was taken.

6.2.1 Viscoelastic response

Figure 6.1 illustrates the stress response of a linear viscoelastic material to a sinusoidally applied cyclic strain loading. This response is typical of what is obtained from cyclic elastomer tests in pure shear or uniaxial tension. The total dynamic stress response of the material is the vector sum of the elastic and viscous (dynamic) stresses. This response is also sinusoidal and leads the applied strain load by an angle *δ*, the viscous loss angle.

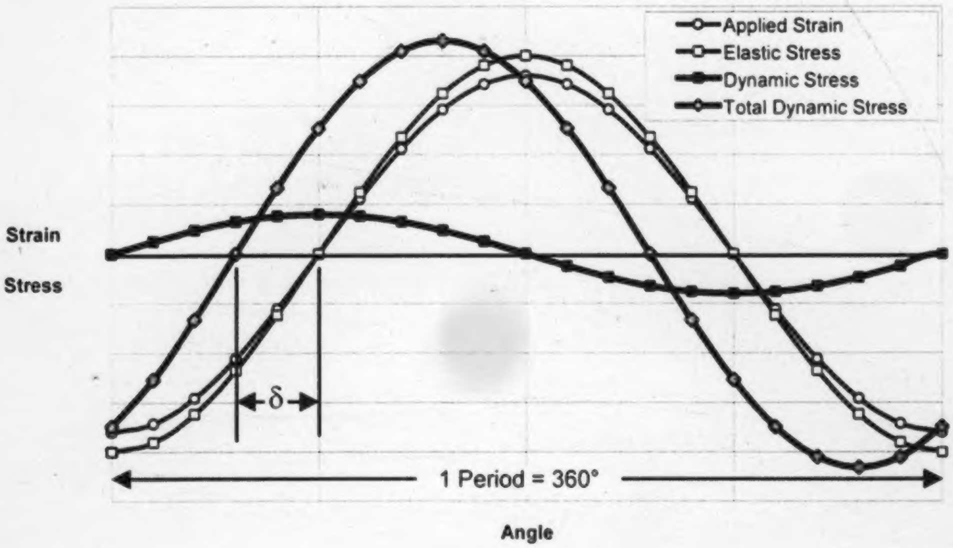

Figure 6.1. Dynamic response of elastomer to applied sinusoidal strain.

The elastic stress response is in phase with the applied strain and can be predicted from results of static material tests. The viscous stress response varies with the *rate* of applied strain and is hence 90 degrees out of phase with the elastic strain (and elastic stress). The components of total stress may be related to the components of elastic and viscous stresses using

$$\tau_{total} = \sqrt{\tau^2_{elastic} + \tau^2_{viscous}} \qquad [6.1]$$

where: τ_{total} is the total dynamic stress;

$\tau_{elastic}$ is the elastic stress; and

$\tau_{viscous}$ is the viscous stress.

The phase angle δ is a result of the combination of the elastic and viscous stress responses of the elastomer. The tangent of the phase angle, *tan* δ, is referred to as the loss tangent of the material. If the applied strain is

$$\varepsilon = \varepsilon_{\max} \cdot \sin(\omega t)\,. \qquad [6.2]$$

Then the stress response will be

$$\tau = \tau_{\max} \cdot \sin(\omega t + \delta) \qquad [6.3]$$

Whereas the stress-strain response of a linear elastic material in simple tension may be described by an elastic modulus, E, linear viscoelastic stress-strain response in tension is typically characterised by an elastic (storage) modulus, E', a viscous (loss) modulus, E'', and a complex modulus, E^*. The viscous tensile modulus, E'', is defined as the viscous stress generated per unit strain rate. The vector diagram shown in Figure 6.2 relates these moduli.

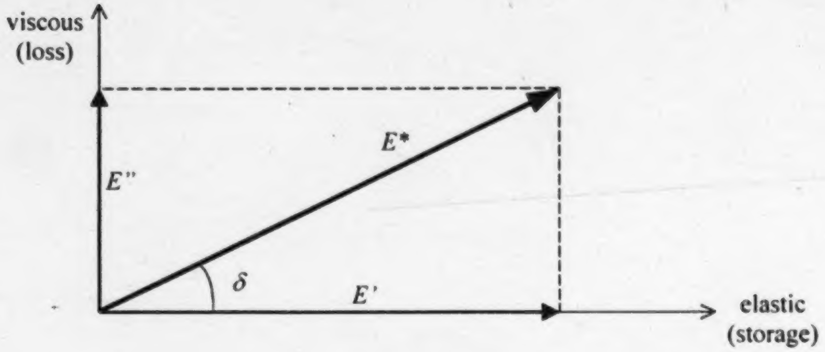

Figure 6.2. Vector diagram relating elastic, viscous, and complex moduli.

The complex tensile modulus, E^*, is the vector sum of the elastic and viscous moduli:

$$E^* = E' + iE'' \qquad [6.4]$$

where $i = \sqrt{-1}$.

The magnitude of the complex modulus may be determined with

$$|E^*| = \sqrt{|E'|^2 + |E''|^2} \qquad [6.5]$$

or may be determined using the phase angle and the elastic modulus:

$$|E^*| = \frac{|E'|}{\cos\delta}. \qquad [6.6]$$

Other descriptions for elastomer response are frequently used. Shear behaviour is described using the elastic shear modulus, G', the viscous shear modulus, G'', and the complex shear modulus, G^*. The near-incompressibility of the elastomer means that the shear moduli are on the order of three times smaller than the corresponding tensile moduli. Compliance, the inverse of the modulus value, may also be used to characterise viscoelastic material response.

6.2.2 *Available dynamic test results*

The heat generation modelling strategy uses elastomer properties available through standard dynamic testing techniques along with the elastic response used in the structural analysis as the basis for the material description. Commonly available tensile test results include the loss tangent, $\tan \delta$, and the magnitude of the complex tensile modulus, $|E^*|$, or complex tensile compliance, $|D^*|$ $(=1/|E^*|)$. Alternately, shear test results include the loss tangent and the complex shear modulus, $|G^*|$ or complex shear compliance, $|J^*|$ $(=1/|G^*|)$. Dynamic elastomer tests are typically conducted over a range of temperatures, frequencies, and strain amplitudes to characterise the sensitivity of the elastomer properties to these quantities.

6.2.3 *Application of dynamic test results*

The static finite element results are based on a description of the elastic stress response of the elastomer. While this approach provides an accurate description of the static response of the stator, it introduces error in all structural results because the effect of the viscous component is not characterised. For heat generation modelling, an approximation to the total stress field is made by modifying the static stress field using the loss tangent $(\tan \delta)$ determined from material testing. Figure 6.1 shows the in-phase, out-of-phase, and total stress responses to a sinusoidally applied strain. The in-phase (elastic) stress component may be related to the total stress component by the loss tangent using

$$\tau_{total} = \tau_{elastic} \cdot \sqrt{1 + \tan^2 \delta} \qquad [6.7]$$

This relationship provides a simple method of obtaining the total dynamic stress response from readily available test results. These quantities are used to determine the amount of energy lost at specific points in the elastomer as the rotor cycles within the stator. This procedure is described in detail in Section 6.3.

6.2.4 Frequency, temperature, and amplitude dependence of dynamic material properties

The literature[3,23] and experimental data for elastomers designed for PCP and PDM applications show that loading frequency and amplitude and elastomer temperature may have an effect on *tan δ*. Figure 6.3 through Figure 6.5 show sample sinusoidal dynamic test results with variations in temperature, frequency, and amplitude. The primary sensitivity of the dynamic response is clearly to temperature. Over the temperature range of 0°C to 120°C, the elastic shear modulus and the magnitude of the complex shear modulus decrease by a factor of four and the loss tangent increases by more than a factor of two. Frequency variations also have a marked effect on the moduli and loss tangent, with variations on the order of 25% for the frequency range of 1 Hz to 33 Hz. The strain amplitude has a less obvious effect on the properties. Some of the nonlinearity in the modulus values on the strain sensitivity curve is likely due to the nonlinearity of the stress-strain response at elevated strains. The loss tangent does not show significant changes with strain amplitude in this strain range.

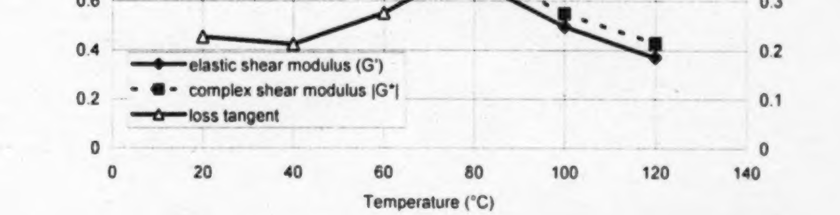

Figure 6.3. Sample variations in dynamic elastomer properties with temperature at an engineering strain amplitude of 12% and frequency of 20 Hz.

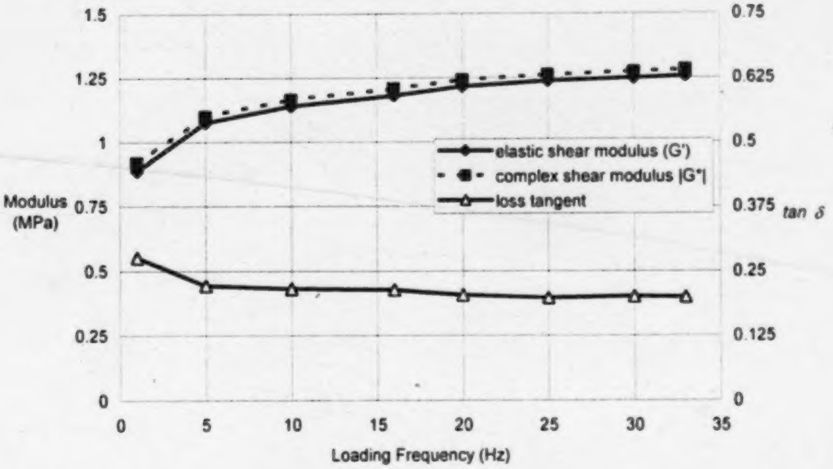

Figure 6.4. Sample variations in dynamic elastomer properties with frequency at an engineering strain amplitude of 12% and temperature of 30°C.

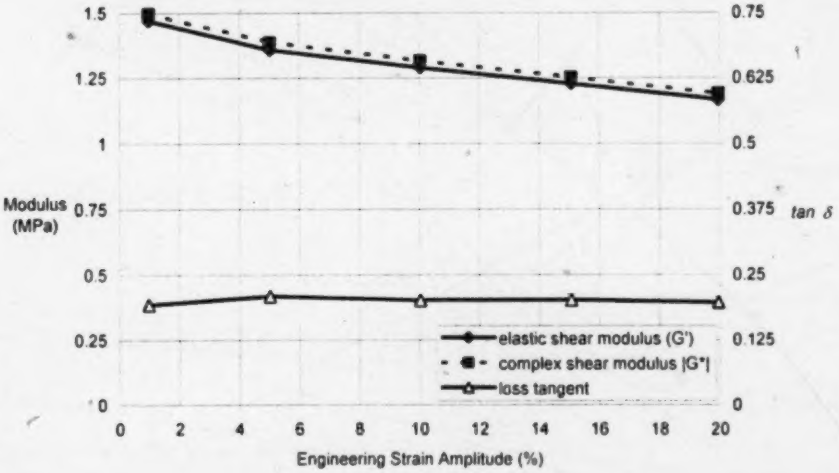

Figure 6.5. Sample variations in dynamic elastomer properties with strain amplitude at a frequency of 20 Hz and temperature of 30°C.

It is recommended that the stator elastomer be tested over a range of temperatures and frequencies that are anticipated in the PCP or PDM application in order to accurately quantify the material parameters used in the finite element analysis.

6.3 Modelling Strategy

6.3.1 Stress and strain history characterisation

The heat generation modelling strategy is designed for the specific purpose of determining the viscous energy lost to the elastomer. The variation in stress and strain loading at different points in the elastomer makes this task computationally demanding.

The hysteresis energy from bulk deformations of the elastomer is negligible compared to distortional deformations because of the near-incompressibility of the material. The errors resulting from discontinuities in the strain field reported by the structural FEA models are also much more significant if a hydrostatic strain energy component is calculated. All heat generation calculations are therefore based on variations in distortional stresses. Distortional stress components are defined in Equation 5.14.

Other thermo-mechanical studies simplify the stress response history to a single sinusoid per load cycle, permitting a simple calculation of the viscous heat generated within the elastomer. McAllen et al.[12] showed that more accurate descriptions of the stress and strain histories change the area of the hysteresis loop and provide a better description of the actual heat generated within the elastomer in a non-sinusoidal loading cycle. Figure 6.6 shows sample variations in the Y-component of normal strain, ε_{YY}, at four different positions within a single-lobe stator elastomer over a complete load cycle. The elements used for these comparisons are shown in Figure 6.7. It is clear that the observed variations in loading are far from sinusoidal and vary considerably according to position within the elastomer.

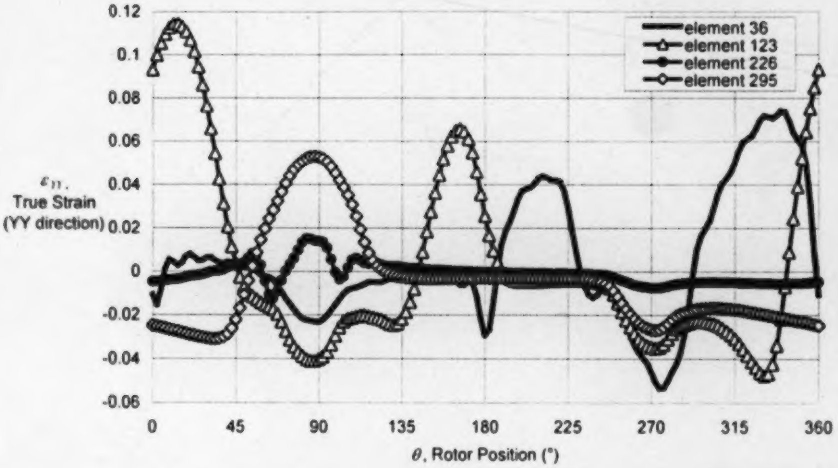

Figure 6.6. Sample variations in normal strain (ε_{YY}) in a single-lobe pump.

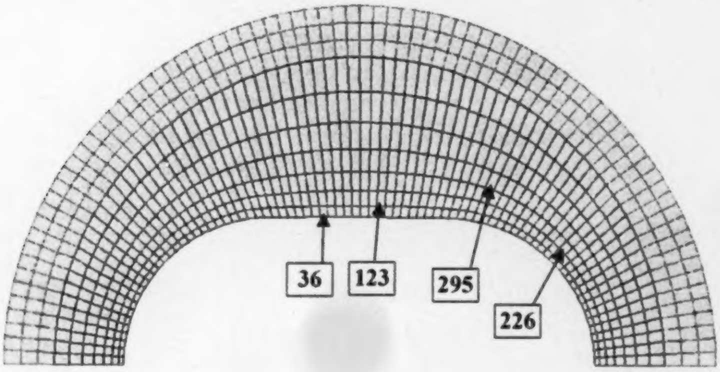

Figure 6.7. Element locations for strain histories shown in Figure 6.6.

McAllen et al.[12] use harmonic cosine Fourier series to describe the time history of effective stress and strain obtained from static structural FEA models of aircraft tire loading. This method of quantifying the structural response creates an accurate description of non-sinusoidal stress and strain histories with analytical expressions that can be determined from simple regressions. An important benefit of fitting a harmonic series to the data is that the viscoelastic phase shift between stress and strain responses can be applied without changing the coefficients of the

Fourier series terms. This allows for examination of the stress-strain hysteresis loop at each model point and a simple integration to provide the heat generation at the node in question.

The general methodology for quantifying heat generation developed by McAllen et al.[12] is adopted for use in this study. Symmetry considerations provided McAllen et al.[12] with the opportunity to use only harmonic cosine series to stress and strain responses. For this study, the scope of the expressions used to describe the stress and strain histories is widened to include both cosine and sine series because the pointwise response in the elastomer in a typical PCP or PDM is not guaranteed to be symmetric. The Fourier series expressions used to describe the cyclic variation in static deviatoric stress and deviatoric strain components from static FEA results are

$$\varepsilon_{ij} = \sum_{k=0}^{M} [{}^{ij}E_k^{\cos} \cdot \cos(2\pi k\eta) + {}^{ij}E_k^{\sin} \cdot \sin(2\pi k\eta)] \qquad [6.8]$$

for strain variations and

$$\tau_{ij}^{static} = \sum_{m=0}^{M} [{}_{static}^{ij}S_m^{\cos} \cdot \cos(2\pi m\eta) + {}_{static}^{ij}S_m^{\sin} \cdot \sin(2\pi m\eta)] \qquad [6.9]$$

for stress variations,

where: ε_{ij} and τ_{ij}^{static} are component *ij* of the total strain and static deviatoric stress respectively;

M is the order of the Fourier series;

$\eta = \frac{t}{T}$ is a non-dimensional description of the time with respect to the cycle length, where t is the time and T is the period of the cycle;

${}^{ij}E^{cos}{}_k$ and ${}^{ij}E^{sin}{}_k$ are the k^{th}-order cosine and sine Fourier series coefficients for component *ij* of the static total strain; and

${}^{ij}_{static}S^{cos}_m$ and ${}^{ij}_{static}S^{sin}_m$ are the m^{th}-order cosine and sine Fourier series coefficients for component *ij* of the static deviatoric stress.

The contribution of the viscous stress response to the total dynamic stress is not accounted for in the work conducted by McAllen et al.[12] While it is expected that the viscous stress component will not contribute significantly to the total dynamic stress, the procedure developed for this study incorporates this quantity into the expression.

Each Fourier coefficient describing the variation in static stress τ_{static} is modified to incorporate the associated dynamic stress component using the factor $\sqrt{1+\tan^2(\delta)}$ from Equation 6.7 as follows:

$$ {}^{ij}S^{cos}_m = \sqrt{1+\tan^2(\delta_m)}\cdot {}^{ij}_{static}S^{cos}_m \text{ and } {}^{ij}S^{sin}_m = \sqrt{1+\tan^2(\delta_m)}\cdot {}^{ij}_{static}S^{sin}_m . \qquad [6.10]$$

Note that each frequency has an associated value of δ.

McAllen et al.[12] quantify viscous energy loss in the elastomer by using the known material-specific phase angle δ to apply a phase shift to the static strain history. This approach is also used for this investigation. The phase angle δ was varied for each term of the Fourier series according to the results of dynamic property testing in order to capture frequency-dependent material response. The harmonic series used to describe strain and stress variations after the application of a phase shift by the viscous loss angle are:

$$\varepsilon_{ij} = \sum_{k=0}^{M}[{}^{ij}E^{cos}_k \cdot \cos(2\pi k\eta - \delta_k) + {}^{ij}E^{sin}_k \cdot \sin(2\pi k\eta - \delta_k)] \qquad [6.11]$$

for strain variations and

$$\tau_{ij} = \sum_{m=0}^{M}[{}^{ij}S^{cos}_m \cdot \cos(2\pi m\eta) + {}^{ij}S^{sin}_m \cdot \sin(2\pi m\eta)] \qquad [6.12]$$

for stress variations, where δ_k is the viscous lag angle for the k^{th} term of the Fourier series.

The nodal stress and strain histories shown in Figure 6.8 are taken from a structural analysis of a sample single-lobe stator. Also shown in the figure are the analytical functions developed through regressions with harmonic sine and cosine series. The stress and strain variations obtained from 64 static finite element analyses (one rotation of the rotor) are described with Fourier sine and cosine series of order 32.

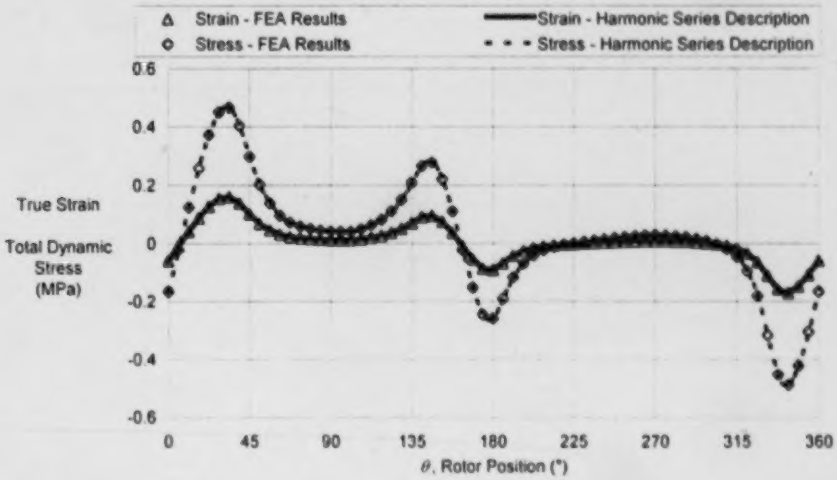

Figure 6.8. Sample correlation between FEA results and Fourier series approximations to static stress and strain.

The viscous lag angle is introduced after the stress and strain series are characterised with Fourier sine and cosine series. Figure 6.9 shows a phase shift of 20° applied to 1 Hz and 2 Hz sinusoidal strain variations over one period. It is important to note that the offset in the global time scale that corresponds to the phase angle is dependent on the frequency of loading. This is different than simply shifting each strain value along the time axis by a fraction of the period (20°/360°). Figure 6.10 shows the loading history from Figure 6.8 with a phase shift of 20°

applied to the strain history. The phase shift is incorporated at each frequency described by the Fourier series, resulting in an average phase shift that is weighted based on the frequency of strain fluctuations.

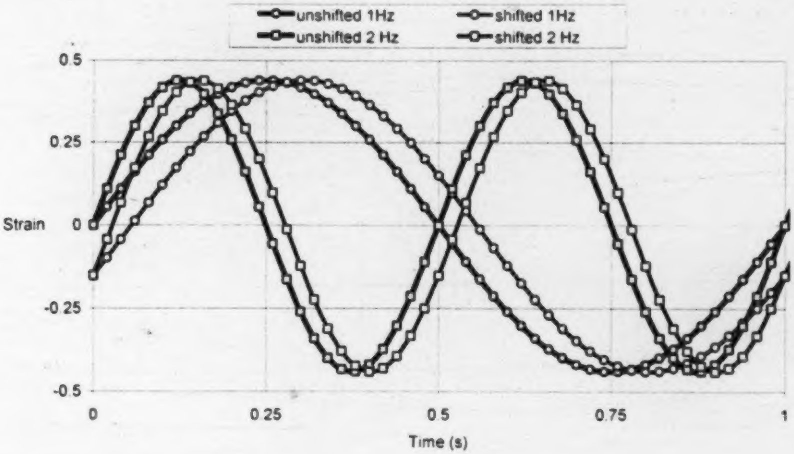

Figure 6.9. Sinusoids showing 20 degree phase shift at 1 and 2 Hz over a one-second interval.

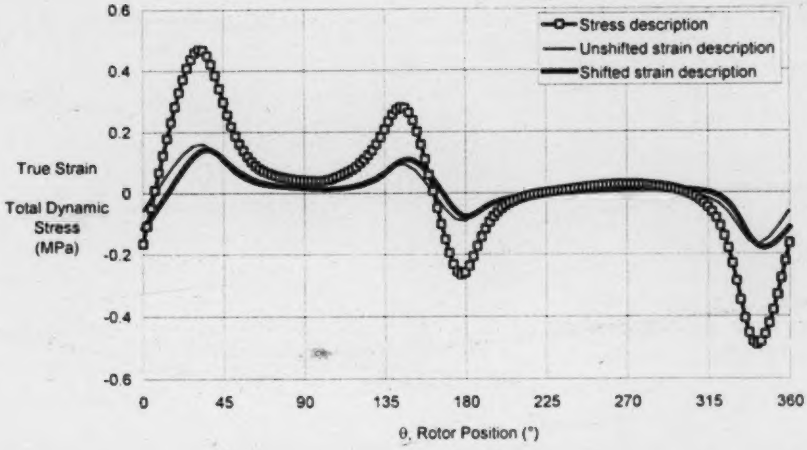

Figure 6.10. Sample stress and strain descriptions (from Fourier series) before and after a phase shift of 20° was applied to the strain series.

Figure 6.11 shows the hysteresis loop that corresponds to the loading history shown in Figure 6.10 and a similar loop obtained through the assumption of a sinusoidal loading pattern between peak and minimum stress and strain values.

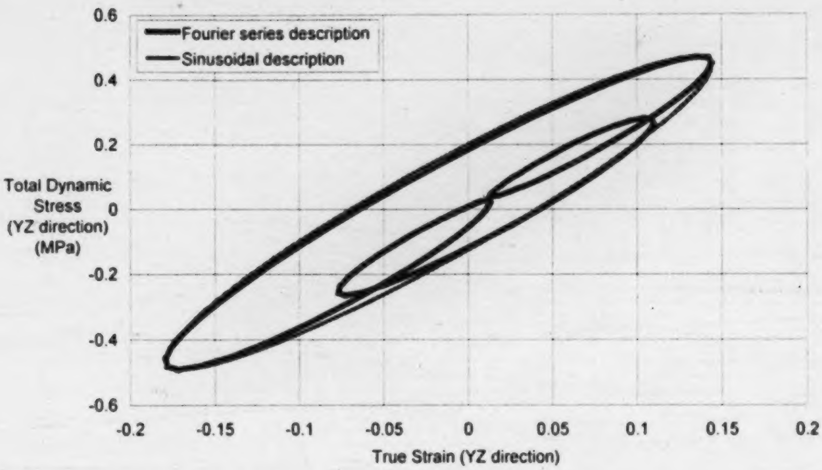

Figure 6.11. Hysteresis loops from Fourier series and sinusoidal descriptions of shear stress/strain history over one cycle at a single point in a two-dimensional model.

The harmonic series description provides an efficient method of characterising any hysteresis loop with any number of load fluctuations, regardless of how non-sinusoidal the loading history is. Previous hysteresis modelling of positive displacement motors[17] used an expression of the form

$$U'' = C \cdot G' \cdot \tan(\delta) * \varepsilon^2 \cdot f \qquad [6.13]$$

to characterise the hysteresis heating energy in the elastomer based on assumed sinusoidal stress and strain variations between the peak and minimum stress and strain values. The accuracy of the approximation shown in the above equation is dependent on the response at each integration point. For instance, in Figure 6.11 the hysteresis loop formed from Fourier series description has an area that is approximately 10% larger than the corresponding sinusoidal loop. The harmonic series description ensures that the entire area inside the hysteresis loop is accounted for in the heat generation calculation, and that variations in dynamic properties with operating frequency are not ignored. The following section describes a method of performing hysteresis energy calculations using Fourier series descriptions of the stress and strain fields.

6.3.2 Heat generation calculations

The energy loss density in a material undergoing a load cycle may be quantified by integrating the strain energy density over the cycle:

$$U'' = \sum_{i=1}^{i=3}\sum_{j=1}^{j=3} U''_{ij} = \int_{t=0}^{t=T} \tau_{ij}(t) \cdot d\varepsilon_{ij} = \int_{\eta=0}^{\eta=1} \tau_{ij}(\eta) \cdot \frac{d\varepsilon_{ij}(\eta)}{d\eta} \cdot d\eta \,. \qquad [6.14]$$

This integral is equivalent to the area within the hysteresis loop.

While a perfectly elastic material will show no energy loss throughout the cycle, the energy lost in a viscoelastic material is closely related to the viscous loss angle δ. The hysteresis energy loss at any point in the elastomer is defined using the coefficients of the Fourier series defined for the static strain and total stress variations and the loss angle δ. The contribution of the hysteresis energy loss density in direction *ij* is defined by

$$\begin{aligned} U''_{ij} = {} & \pi \cdot \sin(\delta) \cdot \sum_{m=0}^{M} m \cdot {}^{ij}E_m^{\cos} \cdot {}^{ij}S_m^{\cos} + \pi \cdot \sin(\frac{\pi}{2} + \delta) \cdot \sum_{m=0}^{M} m \cdot {}^{ij}E_m^{\sin} \cdot {}^{ij}S_m^{\cos} + \\ & - \pi \cdot \cos^2(\delta) \cdot \sum_{m=0}^{M} m \cdot {}^{ij}E_m^{\cos} \cdot {}^{ij}S_m^{\sin} - \pi \cdot \cos(\frac{\pi}{2} + \delta) \cdot \sum_{m=0}^{M} m \cdot {}^{ij}E_m^{\sin} \cdot {}^{ij}S_m^{\sin} \end{aligned} \qquad [6.15]$$

which is derived from Equation 6.14 and the Fourier series descriptions shown in Equations 6.11 and 6.12.

The calculations used to determine the heat generation in the elastomer are computationally intensive. Each planar component of the stress and strain matrices is fitted with a sine/cosine harmonic series pair using a least-squares regression. Six harmonic series of order 32 are generated from 64 stress and strain history points per cycle at each element integration point.

6.3.3 Element heat generation summation

Heat generation calculations performed at each integration point in the stator elastomer provide heat input quantity per rotational cycle per unit volume (i.e., heat input density) at each point. The total heat generated in a finite volume section of the elastomer in a single cycle is the integral of this heat input density over the volume. Heat input is applied to thermal models in the form of an average heat input density for each finite element in the model as described in Chapter 7. An element-by-element approach provides an efficient method of applying heat generation loads to the thermal finite element model while maintaining a relatively fine volume discretisation. The average heat input density per cycle is multiplied by the rotational frequency of the rotor to provide a heat input quantity per unit time.

The heat input integration over each element is conducted using energy density results at each integration point, the associated weighting factors α_i and α_j, and the value of the determinant of the Jacobian matrix at each integration point. The weighting factors are based on the location of integration points in a 9-node element with 3 X 3 integration order.[11] Figure 6.12 shows the integration points in a 2D isoparametric element with the associated weighting factors.

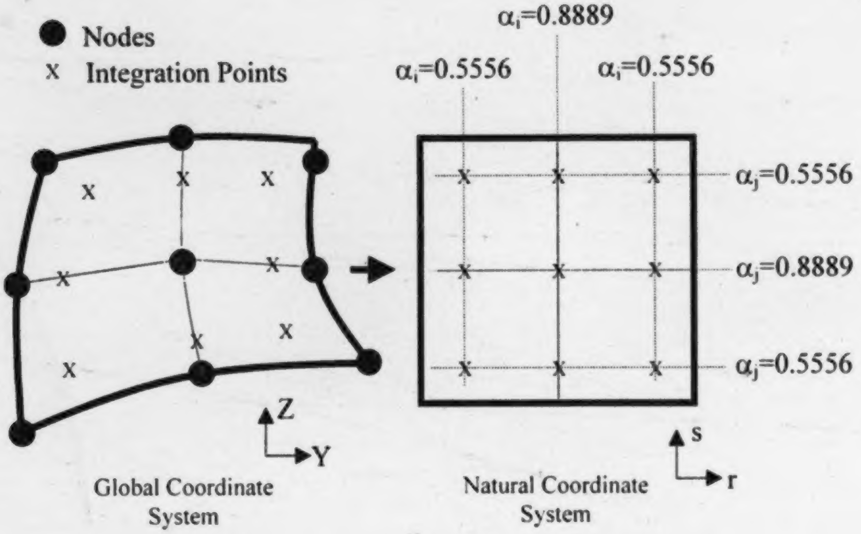

Figure 6.12. Integration points for a single 9-node element with 3 X 3 integration in global and natural coordinate systems and the associated weighting factors α_i and α_j.

The Jacobian matrix relates the natural coordinate derivatives to global coordinate derivatives. In a two-dimensional element, the Jacobian is

$$J = \begin{bmatrix} \dfrac{\partial Y}{\partial r} & \dfrac{\partial Z}{\partial r} \\ \dfrac{\partial Y}{\partial s} & \dfrac{\partial Z}{\partial s} \end{bmatrix} \qquad [6.16]$$

where: Y and Z are the global coordinate directions; and

r and s are the natural coordinate directions.

The individual components of the Jacobian matrix may be evaluated using element shape (i.e., interpolation) functions. For instance, the first component of the matrix may be found using:

$$\frac{\partial Y}{\partial r} = \frac{\partial}{\partial r}\sum_{i=1}^{9} h_i Y_i = \sum_{i=1}^{9} Y_i \cdot \frac{\partial h_i}{\partial r} \qquad [6.17]$$

where: h_i is the i^{th} shape function; and

Y_i is the Y-coordinate of node i.

The other three components of the Jacobian matrix are calculated in a similar fashion. Since the shape functions (h_1 to h_9) are known in terms of the natural coordinates (r and s), calculating the four components of the Jacobian matrix is a relatively simple task.

The determinant of the Jacobian matrix, ($det\ J$), is a useful parameter in relating the value of an integral of a field variable over the natural coordinates to the corresponding integral value in the global coordinate system. In general, the Jacobian determinant is not the same at all positions in the element. For integration purposes, each component of the Jacobian matrix must be quantified at each element integration point.

The heat input density at each element integration point ij is converted to an overall element heat input density using the Jacobian determinant and the weighting factors α_i and α_j at that point:

$$E_{area}^{total} = \int E^{density}\, dA = \iint E^{density} \cdot dy \cdot dz = \iint E^{density} \cdot \det J \cdot dr \cdot ds = \sum_{i,j} \alpha_i \cdot \alpha_j \cdot (\det J)_{i,j} \cdot E_{ij}^{density} . \tag{6.18}$$

Similarly,

$$A_{element} = \iint dy \cdot dz = \iint \det J \cdot dr \cdot ds = \sum_{i,j} \alpha_i \cdot \alpha_j \cdot (\det J)_{i,j} . \tag{6.19}$$

Hence,

$$E_{area}^{density} = \frac{\sum_{i,j} \alpha_i \cdot \alpha_j \cdot (\det J)_{i,j} \cdot E_{ij}^{density}}{\sum_{i,j} \alpha_i \cdot \alpha_j \cdot (\det J)_{i,j}}. \qquad [6.20]$$

Calculated element heat generation densities are written to a text file for input to the thermal finite element models described in Chapter 7.

7 THERMAL MODELLING

A thermal finite element modelling strategy for Progressing Cavity Pumps (PCPs) and Positive Displacement Motors (PDMs) is presented in this Chapter. Thermal models provide a method of predicting the stator temperature distribution that results from elastomer hysteresis heating. A method for accounting for frictional heating between the rotor and stator is also included.

7.1 General Thermal Modelling Considerations

Thermal modelling is limited to steady-state (i.e., non-transient) analyses of PCPs and PDMs. The primary purpose of the thermal modelling work is to describe the elastomer temperature profile that results from elastomer hysteresis and friction heating. Figure 7.1 shows a schematic of the heat transfer conditions in a cross-section of a conventional single-lobe PCP.

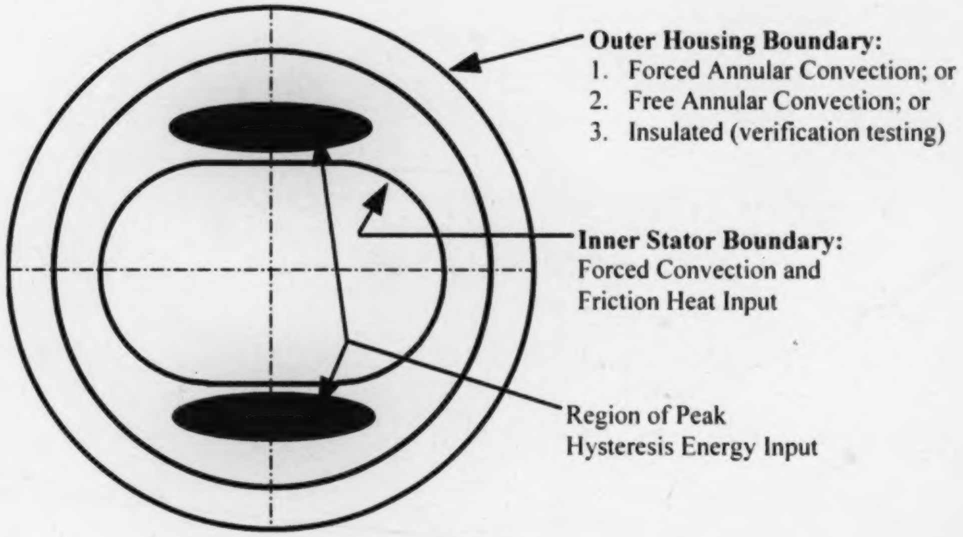

Figure 7.1. Heat transfer conditions in a single-lobe pump.

Key factors that affect the stabilised stator temperature distribution include the thermal conductivity of the elastomer and the housing, the pump geometry, thermal boundary conditions at the inner and outer surfaces of the stator, and the rates and distributions of hysteresis heat generation and friction heating within the elastomer.

7.1.1 Steady-state heat transfer

The tools developed through this investigation enable the prediction of stabilised operating loads in PCPs and PDMs. The goal of the thermal modelling strategy is to determine the steady-state temperature distribution in the stator. Transient thermal effects are ignored except to confirm the validity of the steady-state assumption in a cyclic loading application. As a result, modelling results do not include the time required for the stator to reach the stabilised operating temperature. Transient effects were observed during the experimental verification work and are discussed briefly in Chapter 9.

The instantaneous rate of hysteresis heat generation at a single point in the stator elastomer fluctuates as the rotor moves through its rotational path. Since steady-state modelling assumes unchanging loading conditions, the average heat generation per rotor cycle is used to characterise the hysteresis heat input to the stator. The implication of this assumption is that the thermal models provide an average temperature distribution rather than an indication of how the temperature varies through a rotational cycle. Temperature variations will be small as long as the rate at which hysteresis energy is generated (and dissipated) within a volume of elastomer is small compared to the total amount of heat energy that is held in the volume of elastomer. The total stored heat energy per unit mass of a substance per unit temperature is its specific heat. The specific heat of rubber is on the order of 1.84 kJ/(kg·K).[24] Sample calculations using the heat generation modelling strategy presented in Chapter 6 show that the hysteresis energy generation (and dissipation) per cycle is negligible compared to the stored heat energy. This means that fluctuations in the temperature will be small compared to the overall temperature increase. This modelling approach has been termed "pseudo-steady-state".

7.1.2 Heat transfer to rotor

For the purposes of this study, the role of the rotor in the heat transfer response of the stator is assumed to be insignificant. The rotor affects the results only if it enhances or inhibits heat transfer significantly compared to the convective heat transfer caused by the flow of production or drilling fluids through the pump. Given the short period of time that the rotor is in contact with any point on the stator profile and the nature of the internal fluid flow through the stator, very little error in the overall steady-state thermal response is expected from this assumption. A better understanding of the frictional and hydrodynamic interaction between rotor and stator is required before a more accurate representation of this behaviour can be obtained. This work is beyond the scope of this investigation.

7.1.3 Planar heat transfer

All thermal modelling is conducted using two-dimensional cross-sections of the stator taken in the same plane as the two-dimensional structural models. The pseudo-steady state approach to heat transfer modelling means that the thermal conditions in all cross-sections will be similar. Errors in the planar approximation are only expected in stators with high helix angles. In this case, the planar model is expected to overestimate the peak elastomer temperature because the hysteresis energy must be conducted through a longer distance than if the helix were present. The extent to which the planar models are in error will be loosely tied to the magnitude of the out-of-plane component of the surface normal vector on the inside of the stator, defined graphically in Figure 7.2.

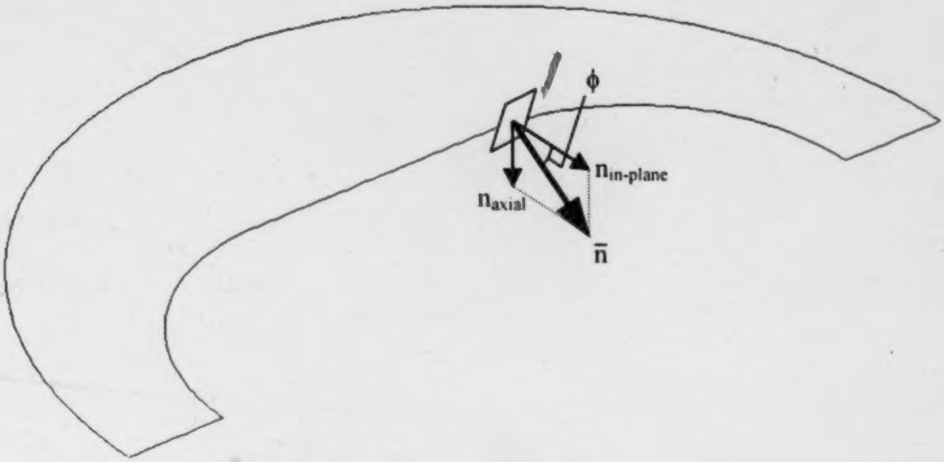

Figure 7.2 Surface normal vector at inner profile of stator elastomer.

The angle ϕ represents the smallest angle between the surface normal vector and the modelling plane. For a single-lobe pump (1:2 lobe configuration) in the vicinity of the peak expected elastomer temperature, the value of ϕ varies from a minimum at one end of the straight section on the inner elastomer profile of the minor seal line to zero at the centre of the straight section to a maximum at the opposite end of the minor seal as shown in Figure 7.3. The absolute maximum value of ϕ is equal to the helix angle defined in Equation 5.16.

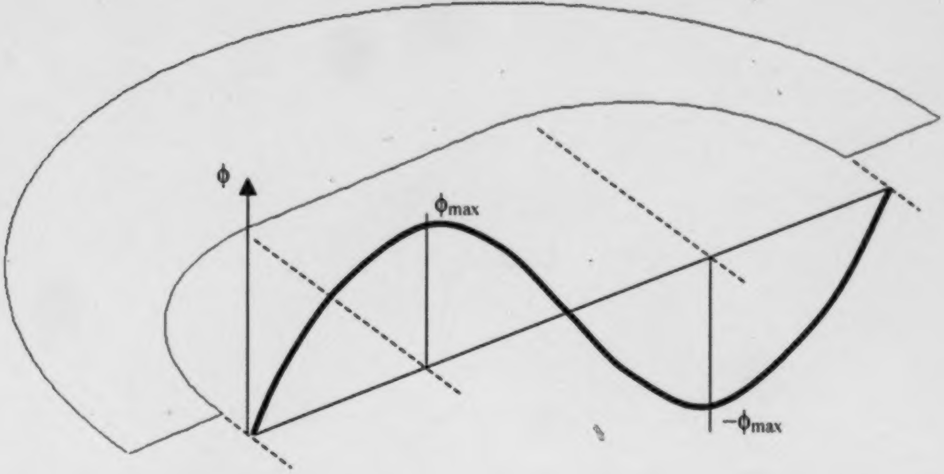

Figure 7.3 Description of out-of-plane normal component along inner profile of single-lobe stator.

Helix angles for typical single-lobe pumps may be as high as 30°, resulting in helix cosines as low as 0.86. This means that the planar heat transfer assumption overestimates the distance to the inner elastomer profile by approximately 14% at the ends of the straight section on the inner profile.

7.1.4 Perfect bond at housing inside diameter

Thermal contact resistance typically results from surface roughness effects between two surfaces that are in contact. It is assumed that the thermal contact resistance between the elastomer and steel housing does not affect the overall thermal response of the stator. This assumption is made because the stator manufacturing process involves the injection of liquefied elastomer into the housing. However, the effect of bonding agents used to ensure shear strength at the bond is unknown. If this effect is deemed to be significant, it may be incorporated into the modelling strategy using a thin layer of transition elements of representative conductivity between the elastomer and housing. The effects of bonding agents and imperfections in the bond on thermal response are not addressed in the present work.

7.2 Material Considerations (Thermal Modelling)

The pertinent material properties required for steady-state thermal finite element modelling are the thermal conductivities of the elastomer and the housing material (steel), k_e and k_h. The typical thermal conductivity of nitrile elastomers is 0.25 W/m·K [25], while steel conductivity ranges from 40 W/m·K to 60 W/m·K depending on composition.[26] The elastomer conductivity is of primary importance to the temperature distribution as it governs the temperature change associated with a given heat flux from the heat generation source to the elastomer boundary. Elastomer conductivity may be temperature-sensitive, and this information should be used in the material description if available. The ADINA-T thermal finite element package is capable of modelling temperature-sensitive conductivities using interpolation between specified values. Sensitivity of the response to steel thermal conductivity is low because the values are so high compared to the thermal conductivity of the elastomer.

7.3 Thermal Finite Element Formulations

Thermal modelling strategies use two-dimensional planar finite elements. The planar heat transfer assumption means that no thermal gradients exist out of the modelling plane.

7.3.1 Continuum elements

Heat transfer behaviour within the stator elastomer and housing is analysed using 9-node isoparametric elements analogous to those used for structural modelling. Quadratic shape functions are used to describe the element shape and variations in temperature within each element.

7.3.2 Convection elements

Convection elements are used to describe heat transfer behaviour to fluid at the inner and outer profiles of the stator. A single three-node convection element is meshed along the edge of each 9-node continuum element. Convection elements make use of quadratic shape functions.

7.4 Modelling Strategy

7.4.1 Mesh density

The density of the thermal finite element mesh is dictated by the mesh density in corresponding structural models. This approach is used because consistent element size and numbering facilitates the transfer of information between the thermal and structural models. The structural mesh density is adequate to describe variations in temperature and heat flux. Figure 7.4 shows the distribution of temperature and total heat flux (magnitude) in a sample single-lobe stator using the mesh density from the corresponding structural model. The temperature and heat flux profiles shown represent the average values over each cycle. As indicated in Section 7.1.1, the thermal response is not expected to change significantly during each rotational cycle of the rotor.

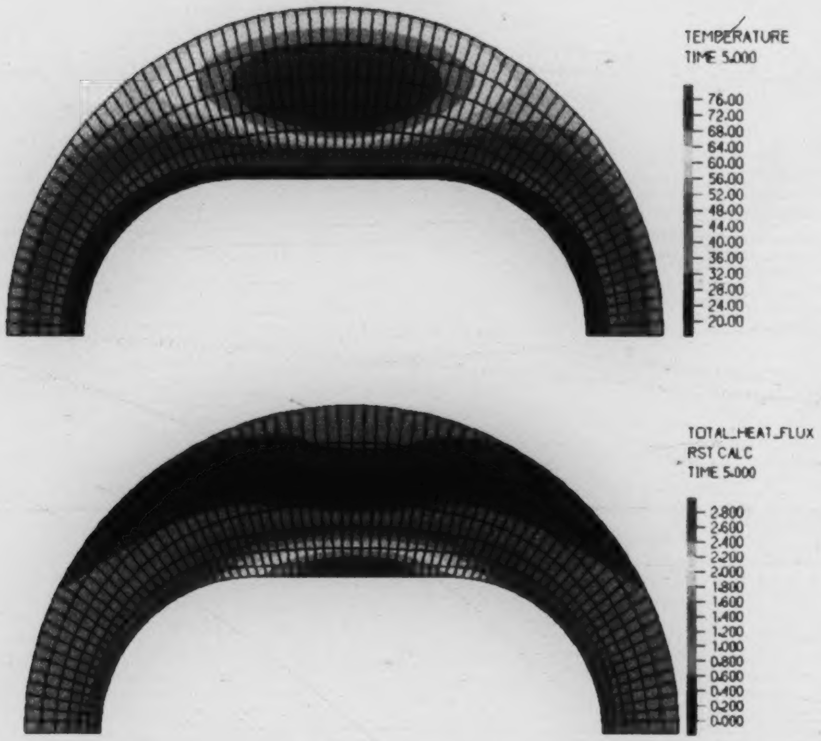

Figure 7.4. Sample contour plots of temperature (top) and magnitude of total heat flux (bottom) in the elastomer from thermal finite element model showing suitability of structural mesh density. (Temperature units °C, Flux units mW/mm^2)

7.4.2 Boundary conditions

A number of representative convective boundary conditions at the inner and outer surfaces of the stator are possible. The complex nature of the flow within the stator and the variation in downhole operating conditions make such conditions difficult to quantify.

The steady-state heat transfer analysis technique means that the choice of convective boundary conditions dictates the ratio of the energy that is transferred to the produced fluid to the energy transferred to the annular fluid and its distribution along the surfaces. Convection on the outer surface of the housing may be described using existing relationships for forced and free convection in an annulus. Heat transfer at the inner convective boundary of the stator may be approximated using a constant-temperature condition or a forced convection model.

7.4.2.a Heat transfer at housing outside diameter

The most common operating configuration for PCPs is to have fluid flowing from production perforations to the pump inlet through the annular space between the stator housing and casing inside diameter. Fluid is then pumped through the stator towards surface. This configuration creates a forced convective heat transfer condition at the outside diameter of the stator housing. PCPs may also operate with stagnant fluid in the external annulus if the perforations are located below the pump fluid intake. In this case, a free convective heat transfer condition is present. PDMs typically operate with drilling fluid flowing through the annulus outside of the stator housing, which is a forced convection condition.

Convective heat transfer descriptions for free and forced convection in an infinite-length annulus are well established.[26,27] For practical purposes, the infinite-length assumption is accurate for most of the length of the stator because the typical ratio of the length of a stator to its diameter tends to be large. The validity of the convective descriptions for the annular space outside the stator housing is not addressed as part of this investigation.

A third external boundary condition is used for thermal models created to predict temperatures seen during the verification testing described in Chapter 9. The exterior housing surface of the single-lobe pump was insulated in an effort to obtain a higher peak elastomer temperature and to maintain a consistent test environment. For thermal analyses of this situation, the heat flux at the housing outside diameter is set to zero. It is assumed that the fluid flowing through the pump dissipates all hysteresis and frictional energy.

7.4.2.b Heat transfer at stator inner profile

The boundary condition at the inner profile of the stator elastomer is much more difficult to characterise than that at the outside diameter. While heat transfer relationships exist for forced convection through symmetrical geometries such as cylinders or flat plates, a stabilised thermal boundary layer is unlikely to develop within the mixing flow of a working pump or motor.

It is proposed that the flow of fluid within the cavities of a single-lobe progressing cavity pump is analogous to the constant-volume plug of fluid moving through a pipe shown in Figure 7.5. Pistons moving along the pipe carry a fixed volume of fluid and form seals with the pipe surface to contain the fluid. The constant-volume fluid cavities formed between the rotor and stator are similar as they move axially through the pump as the rotor is rotated. No investigation of flow patterns within fluid cavities is included as part of this study. The fluid likely circulates within the cavity as it progresses through the pump because the no-slip condition at the stator surface must be satisfied. Figure 7.6 shows this concept graphically.

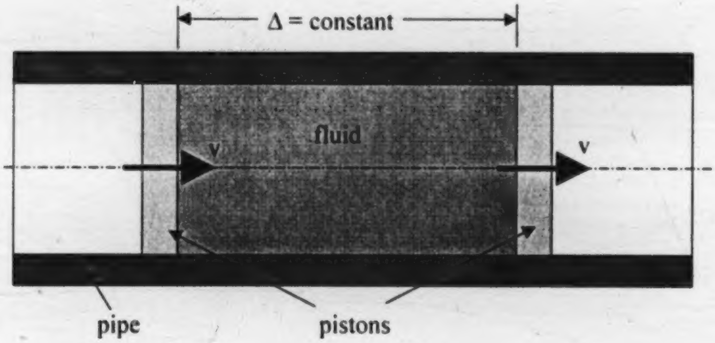

Figure 7.5. Flow situation that is analogous to cavity flow within PCPs and PDMs.

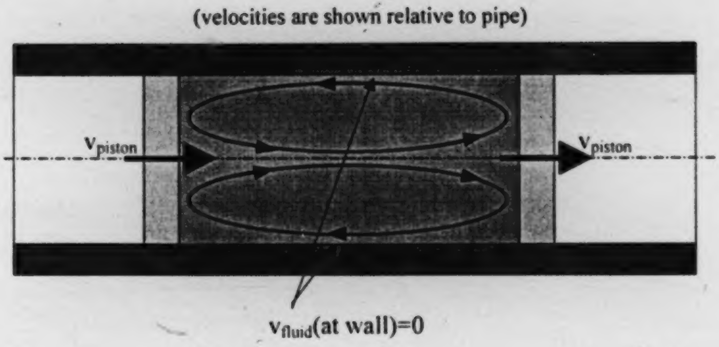

Figure 7.6. Circulating flow pattern within pipe that is analogous to flow in cavity.

Two boundary conditions are proposed to describe heat transfer at the inner profile of the stator for the thermal modelling work in the absence of any empirical or analytical relationships to describe this condition. A constant-temperature boundary condition at the fluid temperature assumes that there is perfect energy transfer between the stator and fluid. The circulating flow within the cavity will encourage heat transfer because the temperature of all of the fluid in the cavity will tend to increase. A second boundary condition assumes a constant heat transfer coefficient along the inner profile of the elastomer. This assumption provides more flexibility with respect to sensitivity analyses. An infinite convection coefficient yields identical results to the constant-temperature condition.

Errors resulting from an inaccurate description of the inner boundary condition are likely to change the observed stator temperature distribution considerably. The steady-state heat transfer assumption dictates that the rate of energy generation within the elastomer must be balanced by the energy dissipation at the boundaries. If the stator is externally insulated, all energy will be transferred to the fluid within the stator. An error in the convective description at the inner profile will result in an error in the resulting fluid/surface temperature difference and/or the distribution of temperature along the surface. If convection is also present at the outer stator diameter, an added error could be present in the ratio of energy convected at the inner profile to that convected at the housing outside diameter. This would affect the estimated temperature distribution significantly.

7.4.3 Thermal loading

7.4.3.a Hysteresis heat input

Energy generated through cyclic loading of the stator elastomer is incorporated into thermal models by specifying the average heat input density per unit time for each element in the thermal model obtained using the procedure outlined in Chapter 6. Thermal models are generated so that the finite element mesh and associated node locations and numbering match that of the structural models. Structural heat input results are easily introduced into the thermal models by specifying the heat input density for each element. This meshing strategy also facilitates the introduction of the temperature field obtained through thermal modelling into the structural model for subsequent iterations of the thermomechanical solution procedure. Further detail pertaining to the thermomechanical solution strategy is presented in Chapter 8.

7.4.3.b Friction heat input

The motion of the rotor passing along the inner profile of the stator elastomer and the associated interference fit creates frictional energy losses. The magnitude of this frictional energy may contribute to further heating of the elastomer. A method of accounting for this friction is proposed as part of this investigation. While the actual friction behaviour is likely coupled with hydrodynamic lubrication effects, an approximation to the friction heat input that neglects hydrodynamic lubrication provides a preliminary indication of the sensitivity of the PCP/PDM to heating at the inner elastomer surface.

The primary contact mode between the rotor and stator is sliding friction. In a single-lobe configuration, the velocity of the rotor surface relative to the stator is dependent on the pump rotational speed and the rotor position within the stator cross-section. In certain instances a rolling friction scenario may be encountered. This condition is momentary and will occur in a maximum of four points for each rotation of the rotor cycle. It is assumed that the contribution of rolling friction to the heating process is negligible.

The energy generated due to friction is completely dissipated in the form of heat. The heat input may thus be obtained by quantifying the frictional energy along the inner elastomer profile. This may be done at each contact node for calculation efficiency. The frictional energy, $E_{friction}$, at any point on the inner profile may be described generally by the following relationship:

$$E_{friction} = F_{friction} \cdot d_{app} \qquad [7.1]$$

where: $F_{friction}$ is the frictional force, obtained directly from finite element output; and

d_{app} is the distance through which the frictional force travels.

The discretised nature of the available structural results leads to an approximation through the n substeps conducted for the analysis. The frictional energy at any given point on the interior stator profile can be described in terms of the friction force and distance travelled during each of the n substeps. The distance the rotor surface travels relative to the stator surface at the minor seal during the n^{th} substep may be described as a function of the rotor position, θ,

$$\Delta d^{n}_{app} = D^{minor}_{rotor} \cdot \pi \cdot \frac{(\theta_n - \theta_{n-1})}{360} + 2e_{actual} \cdot (\sin\theta_n - \sin\theta_{n-1}) \qquad [7.2]$$

where: Δd^{n}_{app} is the distance the contact patch travels in the n^{th} substep (mm);

θ_n is the rotor position at the n^{th} substep (°); and

e_{actual} is the operating eccentricity (mm).

The friction force at each contact node for each static load step is available as a result of the finite element models. The total frictional energy generated at each point on the interior profile may be calculated from the friction force results and the analytical description of the rotor position over the n substeps:

$$E_{friction} = \sum_{n} F_{friction_n} \cdot \Delta d_{app}^{n} \qquad [7.3]$$

Frictional heating loads are applied to the FEA models on a node-by-node basis.

7.5 Sample Results

Thermal modelling results highlight the insulative properties of the elastomer. Large gradients in the elastomer temperature are observed at the thickest part of the elastomer, while little temperature change is evident as energy travels through the stator housing. Significant changes in the stator temperature distribution are evident when the convective boundary conditions are modified.

Figure 7.7 and Figure 7.8 show temperature distributions in a conventional single-lobe PCP with convective and insulated thermal boundary conditions on the stator housing surface respectively. A convective boundary is used at the inner profile of the stator in both cases. The applied hysteresis heat input field is identical for both analyses and friction is ignored. The insulated case generates a temperature increase that is almost 50% higher than that seen in the case with annular convection. This increase is a result of the longer distance the heat must travel in order to escape to the inner boundary in the insulated case.

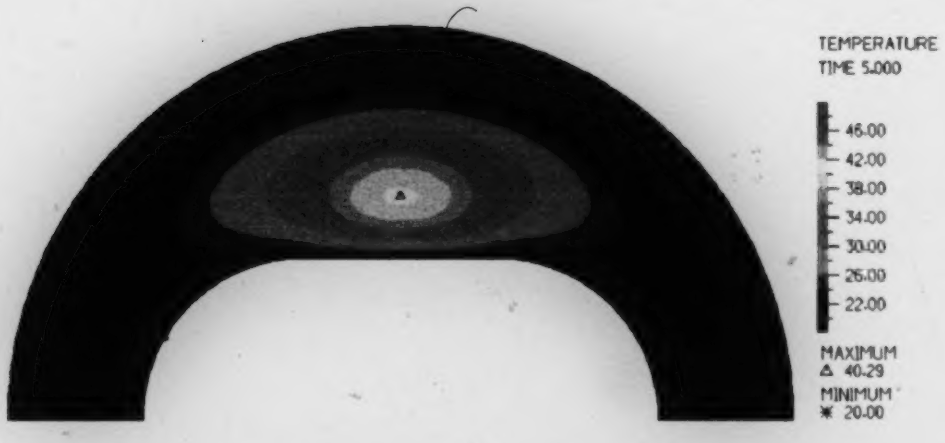

Figure 7.7. Sample temperature distribution in stator with annular convection boundary condition on housing outside diameter. (Units in °C)

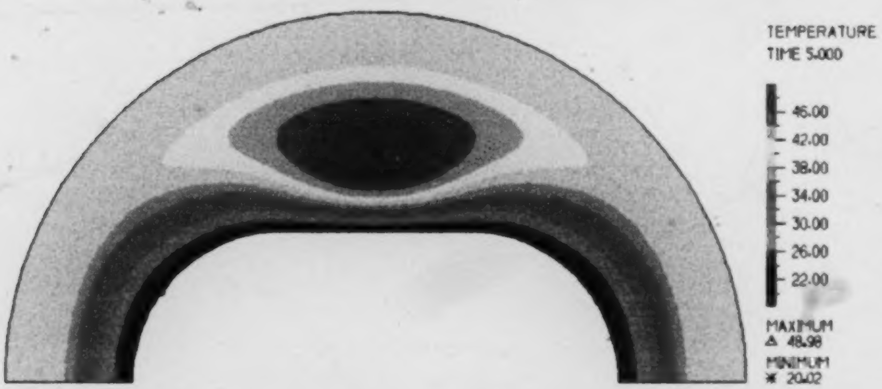

Figure 7.8. Sample temperature distribution in stator with insulated boundary condition on housing outside diameter and hysteresis heat input distribution used in Figure 7.7. (Units in °C)

The introduction of frictional heating does not appear to affect the temperature distribution significantly for a sample single-lobe pump. Figure 7.9 shows the modified temperature distribution for the insulated housing case in the presence of friction. The temperature at the surface of the elastomer at the minor diameter increases only 0.3 °C using a uniform coefficient of friction of 0.3 and the hysteresis input field used for the frictionless analysis. The peak elastomer temperature changes by approximately 0.2 °C. The impact of frictional heating on the temperature field is small because gradients in elastomer temperature are an artefact of the elastomer thickness. Energy generated at the rotor/stator interface is in the immediate vicinity of a convective boundary and will increase the temperature at this boundary. For the insulated outer boundary case, there will be a corresponding temperature increase in the elastomer.

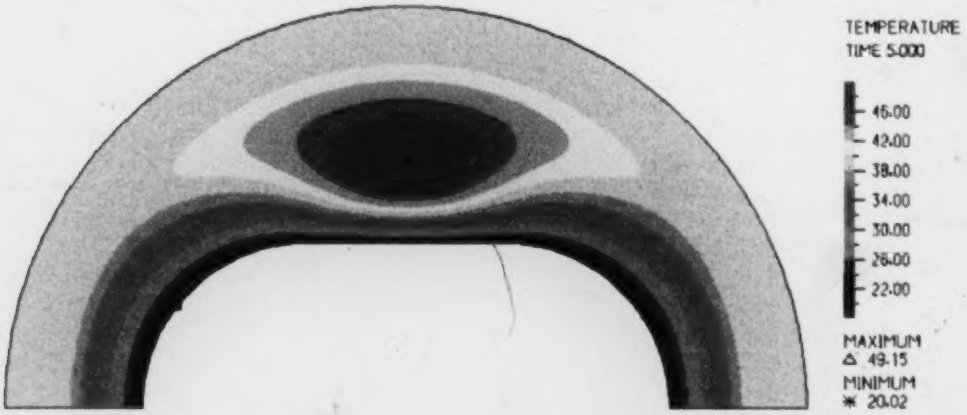

Figure 7.9 Sample temperature distribution in stator with friction heat input for insulated boundary condition on housing outside diameter and hysteresis heat input distribution used in Figure 7.7. (Units in °C)

Sample results are presented above to demonstrate the capabilities of the modelling strategy. The actual thermal response of the stator will depend on the pump geometry and the nature of the convective heat transfer at the inner and outer boundaries.

8 COUPLED THERMO-MECHANICAL MODELLING

Stabilised pump or motor operating loads are dependent on the temperature distribution in the stator. Thermal strains cause changes in the dimensions of the stator cavity, effectively increasing the rotor/stator interference. This sensitivity to temperature changes is due to the high thermal expansion coefficient of the elastomer material and the confinement induced on the outside diameter of the elastomer by the more rigid stator housing. In operation, the stator will stabilise to a temperature at which a balance between heat generation and heat removal is achieved with the thermally strained elastomer geometry. Temperature sensitivity of structural and thermal material properties may also be a contributing factor to the stabilised operating point. An iterative solution strategy for finding compatible thermal and structural solutions that represent the stabilised operating point of the pump or motor is presented in this chapter.

8.1 General Thermo-Mechanical Considerations

Depending on the component being analysed, a thermo-mechanical analysis can be as simple as obtaining the structural response of the component to an applied thermal expansion load. Usually, structural loads such as surface tractions accompany such thermal expansion loads. A more complex strategy for thermo-mechanical analyses is required when the structural loads and thermal expansion loads are dependent on one another. This dependency may relate to temperature-sensitive material properties or can result from modified loads resulting from a change in component geometry with temperature. For this investigation, both cases are true. Temperature may affect structural elastomer material properties and can also generate changes in rotor/stator interference.

Figure 8.1 shows sample temperature distributions in a single-lobe stator.

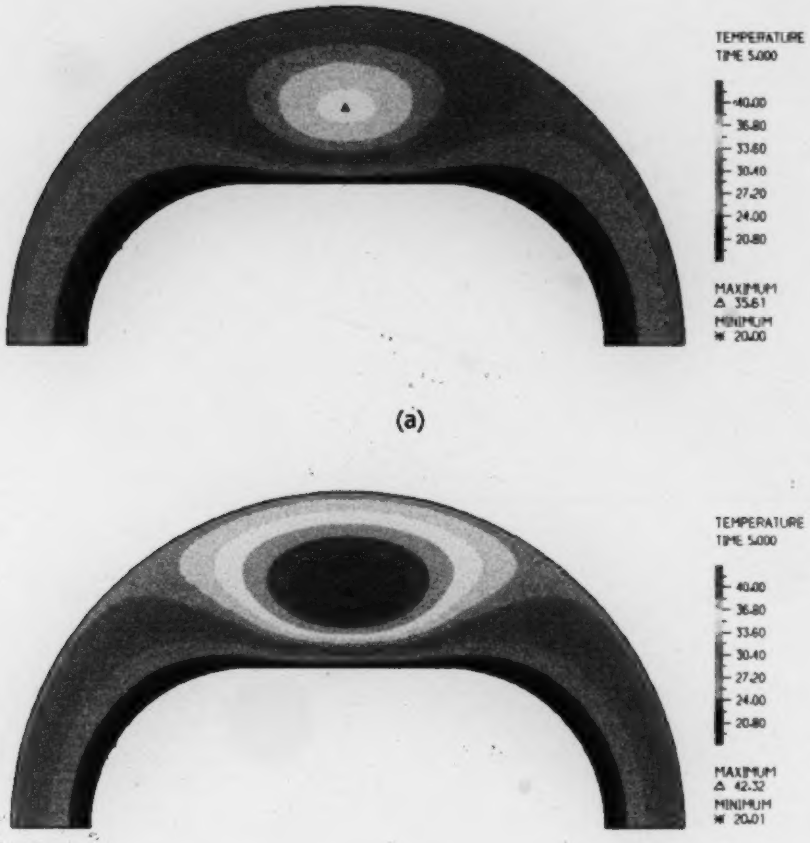

(a)

(b)

Figure 8.1. Temperature distributions in stator elastomer resulting from (a) interference loading at ambient temperature (20.0°C) and (b) interference loading at temperature profile shown in (a).

The temperature fields shown in Figure 8.1(a) is the result of a thermal analysis with an applied hysteresis heat input field for a representative rotor/stator interference fit. The structural analysis used to determine the hysteresis heat input field does not include any thermal expansion loads.

With an initial elastomer and fluid temperature of 20.0°C, the highest predicted temperature in the stator is 35.7°C. If the temperature field in Figure 8.1(a) is used to define a thermal expansion field in a subsequent structural analysis with the same rotor and stator geometries, the increased overall rotor/stator interference fit generates an increase in the amount of hysteresis heating in the stator. The temperature distribution shown in Figure 8.1(b) is obtained by using the increased hysteresis energy in a second thermal analysis. The predicted peak elastomer temperature increases from 35.6°C to 42.3°C.

If the process outlined above is continued, the temperature in the stator elastomer will either begin to approach a stable value or it will diverge. Figure 8.2 shows the peak temperature as a function of the number of iterations conducted. For the example shown in Figure 8.1, the peak temperature stabilises to 48.9°C after 13 iterations. This is a prediction of the peak pseudo-steady-state temperature in the stator under the applied thermal and structural operating conditions. Results of the corresponding structural analysis are the stabilised operating loads that may be expected after the stator has had a chance to adapt to its downhole environment and operating conditions. This represents an important step in the modelling process. While structural models at ambient temperature may provide an approximation of the downhole loading, the stabilised thermomechanical solution provides a better indication of what will actually happen when the stator runs downhole. The difference between ambient and stabilised structural results depends on the fluid temperature, rotational frequency, rotor/stator interference fit, elastomer properties, and a number of other operational variables.

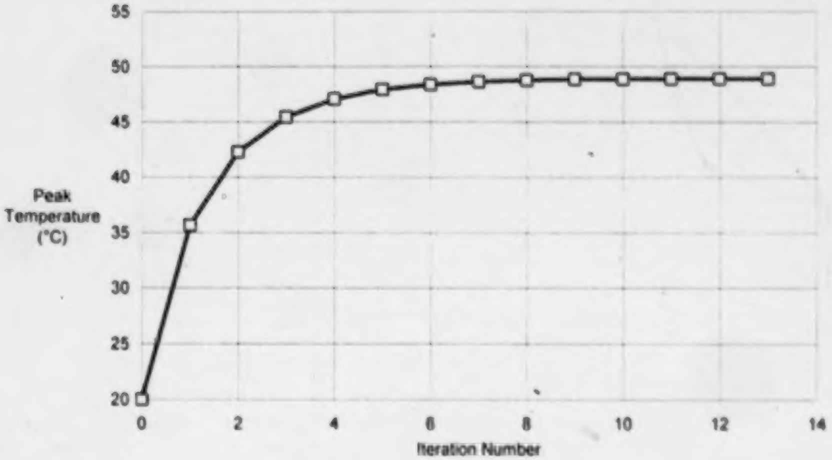

Figure 8.2. Progression of estimated peak elastomer temperature through successive iterations.

The example above illustrates the thermomechanical solution procedure that was developed and automated as part of this investigation. A full description of the procedure is provided in the next section. The validity of the solution depends on how well the structural FEA, heat generation, and thermal FEA models describe the physical processes they model.

8.2 Iterative Solution Procedure

8.2.1 Description

Figure 8.3 shows a flowchart of the iterative solution procedure developed for determining the stabilised stator operating state.

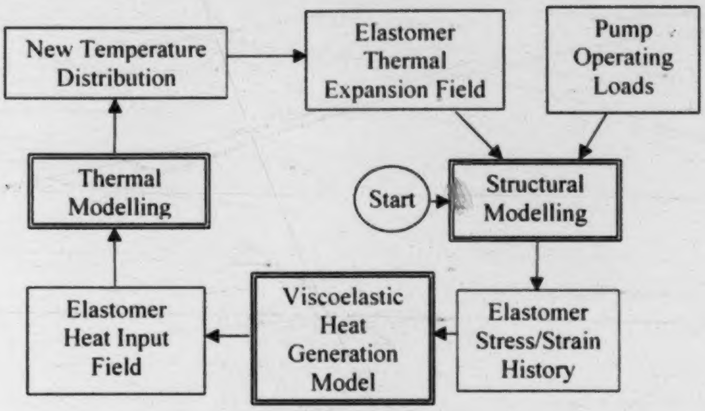
New Temperature Distribution
Elastomer Thermal Expansion Field
Pump Operating Loads
Thermal Modelling
Start
Structural Modelling
Elastomer Heat Input Field
Viscoelastic Heat Generation Model
Elastomer Stress/Strain History

Figure 8.3. Iterative solution strategy flowchart (also presented as Figure 4.1).

The analysis sequence begins with a structural analysis using representative pump operating loads without any form of temperature profile. Representative operating loads may include rotor/stator interference, internal stator pressure, differential pressure between stator cavities, a uniform temperature field at the fluid temperature, volumetric swell, and friction as described in Chapter 5. The structural analysis spans one rotational cycle of the rotor. Results extracted from the structural model include the components of deviatoric stress and strain at element integration points for each step in the analysis.

Heat generation in the elastomer is quantified according to the methods explained in Chapter 6 using custom Visual Basic routines. Static structural analysis results are characterised using Fourier sine and cosine series and converted to equivalent viscoelastic analysis results according to dynamic material property descriptions. The heat generated at each integration point is quantified and integrated over each element to find the average element heat input per cycle.

A steady-state thermal analysis uses the calculated element heat input quantity and the specified boundary conditions to obtain a temperature distribution in the stator elastomer and housing as described in Chapter 7. The temperature profile represents the average temperature at each point in the elastomer over the rotational cycle of the rotor.

The process described in the above paragraphs is repeated using the operating loads and the thermal expansion load generated by heat input to the elastomer. Structural material properties at some points in the elastomer may change considerably as the temperature increases from one iteration to the next. The thermomechanical solution is halted when a convergence criterion such as the change in peak temperature in the elastomer being less than some tolerance is satisfied. Convergence is checked before the start of each structural analysis. Further discussion of convergence criteria is given in Section 8.2.3.

8.2.2 Physical relevance of successive iterations

It is important to note that successive iterations of the thermomechanical solution procedure do not provide an indication of the actual amount of time for the stator to reach thermomechanical equilibrium. This is somewhat different from the results one might obtain from available viscoelastic finite element formulations. The benefit of performing this type of thermomechanical analysis is that the stabilised temperature distribution may be obtained after only a few iterations. By contrast, the viscoelastic analysis would require significantly more solution time and many more structural load increments. The benefit of the viscoelastic modelling approach would be a better understanding of transient heating effects.

8.2.3 Convergence criterion

The criterion used to check for convergence between successive iterations of the thermomechanical solution procedure is most easily obtained from thermal analyses. The temperature profile in the stator is a result of the structural, heat generation, and thermal modelling steps of the iterative solution process.

Suggested indicators that can be used in a convergence criteria include the peak temperature within the elastomer and the integral of the absolute elastomer temperature over the 2D thermal modelling area. The temperature integral provides a better indication that the temperature at all points in the stator has not changed in successive iterations. However, sample analyses show that the shape of the temperature profile in the elastomer does not change significantly as the magnitude of the temperature integral increases. For the sample thermomechanical analysis described in Section 8.1, the peak elastomer temperature varies linearly with the magnitude of the temperature integral as shown in Figure 8.4. Based on sample analyses, either quantity is an adequate indicator for use in a convergence criterion for single-lobe pumps but this should be checked for other stator configurations. Acceptable convergence tolerances provide an indication that the solution is not changing from one iteration to the next. For sample cases, the solution was considered to be converged if the change in peak temperature was less than 0.01°C or if the change in the temperature integral was less than 10°C·mm^2.

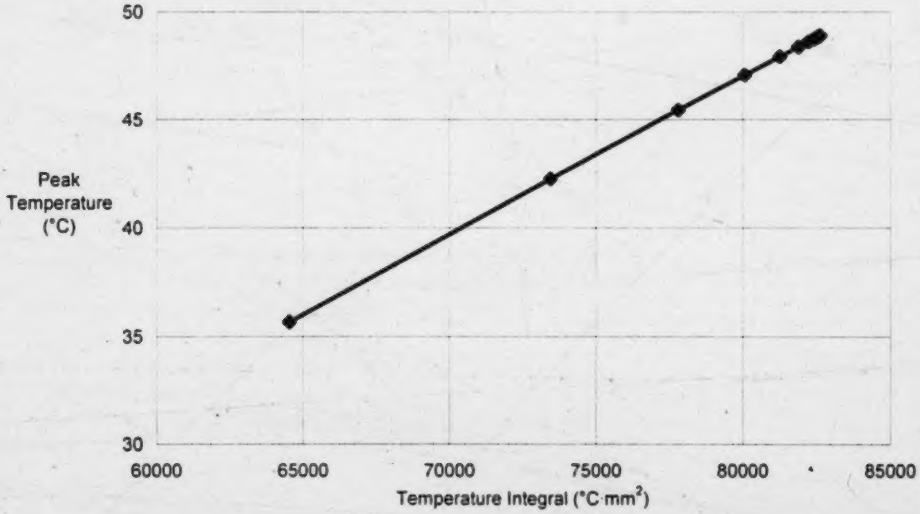

Figure 8.4. Comparison of convergence criteria for thermomechanical analysis of sample single-lobe pump.

8.2.4 Convergence considerations

Figure 8.5 shows the progression of peak temperature as the number of iterations performed increases for a sample single-lobe PC pump. The importance of the iterative strategy is highlighted by the fact that the peak temperature change for the stabilised solution is 84% higher than the peak temperature change observed after one iteration.

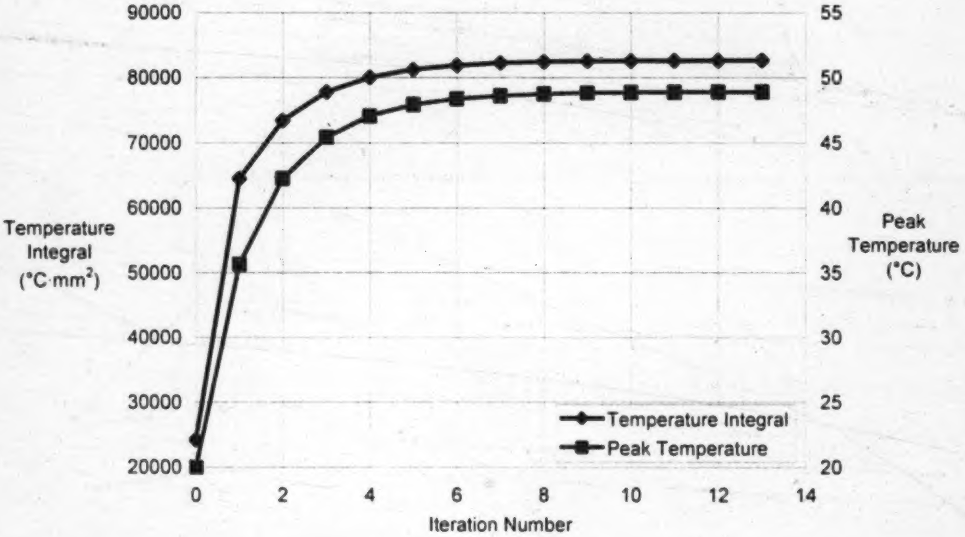

Figure 8.5. Convergence pattern for sample single-lobe thermomechanical analysis.

The true benefit of performing thermomechanical analyses on pumps and motors must be gauged according to design criteria. A 30°C increase in peak elastomer temperature like that shown in the above example may affect material properties to the extent that the life of the pump is significantly reduced. Similarly, thermal expansion from the temperature change may be significant enough to increase the rotor/stator interference and any associated operating considerations such as seal capacity. Comparisons between the predicted peak operating temperature and maximum allowable elastomer temperature may also aid in the design process.

Not all thermomechanical analysis cases are expected to converge. If the thermal expansion caused by hysteresis heating is severe enough, there may not be a thermally strained geometry which generates compatible structural and thermal loads. Figure 8.6 shows an example of converging and diverging solutions. The geometry, operating conditions, and material properties are identical for both solutions with the exception of the thermal expansion coefficient, which is higher for the diverging solution. Rather than achieving a stabilised value, the peak temperature increases with each successive iteration for the diverging case. The diverging solution means that there exists no thermally strained geometry configuration that generates hysteresis heat at a rate that does not cause further thermal expansion. From a practical standpoint, this may be a good indicator that the pump or motor will not be able to withstand downhole operation under the specified operating conditions. Other factors that could cause a solution to diverge include low elastomer thermal conductivity, high pump speed, high elastomer loss tangent, and other factors that increase heat generation or inhibit heat transfer from the elastomer to the convective boundaries. The relevance of predicted stator failures to actual field failures of pumps and motors must be quantified before any conclusions may be drawn about the present thermomechanical procedure as a failure prediction tool. Stator failures due to overheating and fatigue are common (particularly in the case of PDMs) and could possibly be averted with such a tool.

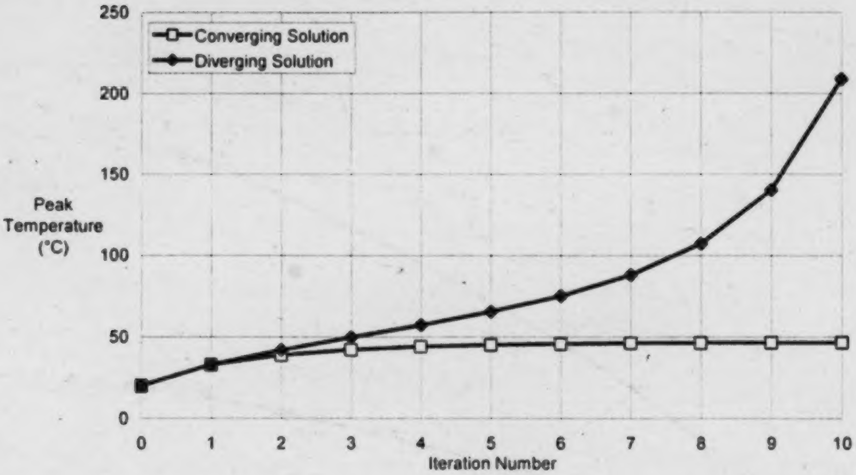

Figure 8.6. Sample converging and diverging thermomechanical analyses.

8.2.5 Convergence optimisation

The time required to obtain a stabilised thermal and structural response from the iterative solution procedure is dependent on the size of the models in use and the number of iterations required to reach this equilibrium solution. This section presents an optimisation method for reducing the number of iterations required to reach this point and to predict if solution convergence is expected. The convergence optimisation procedure is for analyses of single-lobe pump and motor geometries but may be extended to other pump and motor configurations.

Two key characteristics of stator response form the basis of the optimisation technique. First, the temperature distribution in the stator elastomer may be predicted by comparing the peak temperatures from one thermomechanical iteration to the next. The shape of the temperature distribution within the stator elastomer does not change drastically as the peak temperature in the medium increases. Figure 8.7 shows sample temperature profiles along a line through the thickest part of the elastomer in the single-lobe pump. In this example, efficient convective heat transfer to a 20°C fluid is present at the inner and outer boundaries of the stator, causing the temperatures at the inner and outer elastomer surface to be approximately equal to the fluid temperature. Boundary temperatures will not be equal if the convection is not as efficient or when the stator is insulated or exposed to free convective boundary conditions on the outside diameter. In general, the shape of the temperature profile remains unchanged through successive iterations even in the presence of these differing boundary conditions.

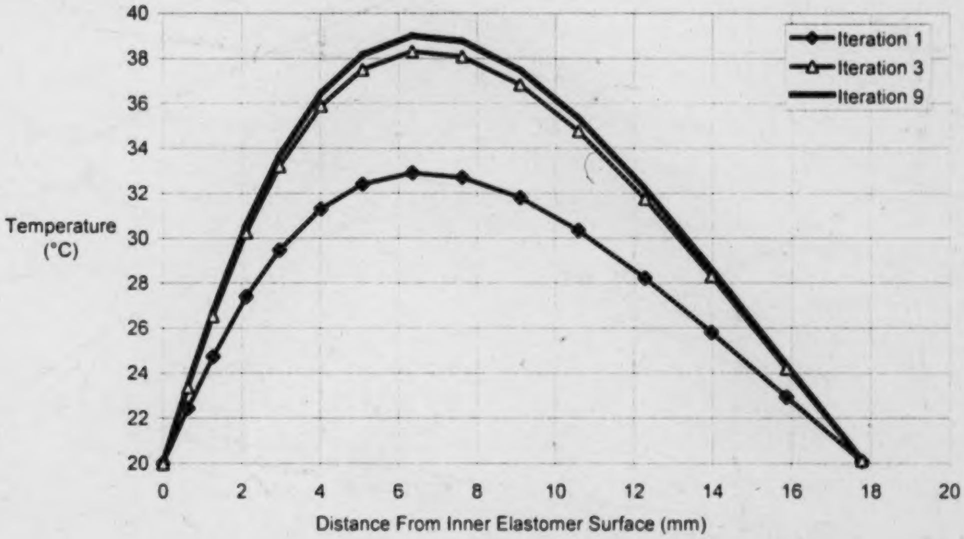

Figure 8.7. Sample temperature profiles through elastomer thickness from 1st, 3rd, and 9th (final) iterations of a thermomechanical analysis with convective boundary condition at housing outside diameter.

The second key response characteristic is that for single-lobe pumps, the peak elastomer temperature appears to increase as a function of the total rotor/stator interference at the minor diameter, where the elastomer is thickest. This function is of the form

$$\Delta T_{\max} = A \cdot interference^{n}, \qquad [8.1]$$

where: ΔT_{max} is the maximum temperature increase along a radial line through the thickest part of the elastomer;

interference is the minor diametral interference (defined in Section 2.2); and

A and n are scalar parameters.

If temperature-insensitive elastomer material properties are used for the analysis, the temperature varies as a quadratic function of the interference (i.e., $n = 2$), as shown in Figure 8.8. However, if temperature-sensitive elastomer material properties such as the elastic modulus and loss tangent vary considerably within the stator cross-section, n may vary. In this case it is suggested that a trial thermomechanical analysis be conducted without optimisation to determine the nature of the relationship between interference and peak temperature. Refer to Section 9.5.2 for a discussion of the observed relationship between interference and peak temperature for the pump and elastomer combinations used for verification testing.

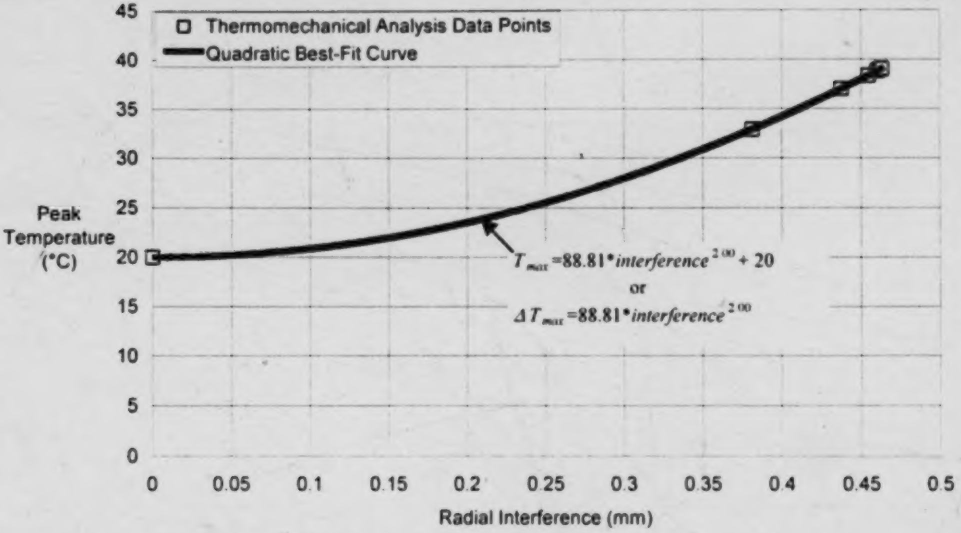

Figure 8.8. Relationship between radial rotor/stator interference and peak elastomer temperature for sample thermomechanical analysis of single-lobe pump with temperature-insensitive material properties.

Using the relationships described in the preceding paragraphs, a series of simple iterations analogous to those conducted during the complete thermomechanical solution procedure can be conducted on a spreadsheet to obtain an estimate of the final temperature distribution in the elastomer. The spreadsheet model uses the results from a single iteration of the complete thermomechanical procedure to predict changes in peak temperature and rotor/stator interference with each subsequent iteration. A worked example of the simple iterative technique is presented in Appendix B.

Figure 8.9 shows the iterative analysis process used in the spreadsheet model for single-lobe pumps. The peak interference along the minor seal line and the elastomer temperature profile along a line through the thickest part of the elastomer from the thermomechanical solution are used to characterise the stator elastomer response to thermal expansion loads with three constants. Scalar A (defined in equation 8.1) relates the peak temperature change along the profile line to the interference at the minor diameter. Scalar B describes the ratio of the peak elastomer temperature to the average temperature along the profile line. Scalar C relates the elastomer thermal expansion coefficient, elastomer thickness, and average temperature along the profile line to the thermal rotor/stator interference at the minor diameter (see Appendix B for definition of scalars B and C). Scalars B and C are used in conjunction with the temperature change obtained from the first thermomechanical iteration to obtain a new interference estimate, as demonstrated in Appendix B. Scalar A is then used to obtain a new peak temperature estimate from the new interference estimate. Subsequent interference and temperature estimates are obtained using the same values for A, B, and C until the change in predicted peak temperature between successive iterations is smaller than a convergence tolerance. The result is an estimate of the peak stabilised operating temperature based on a single thermomechanical iteration.

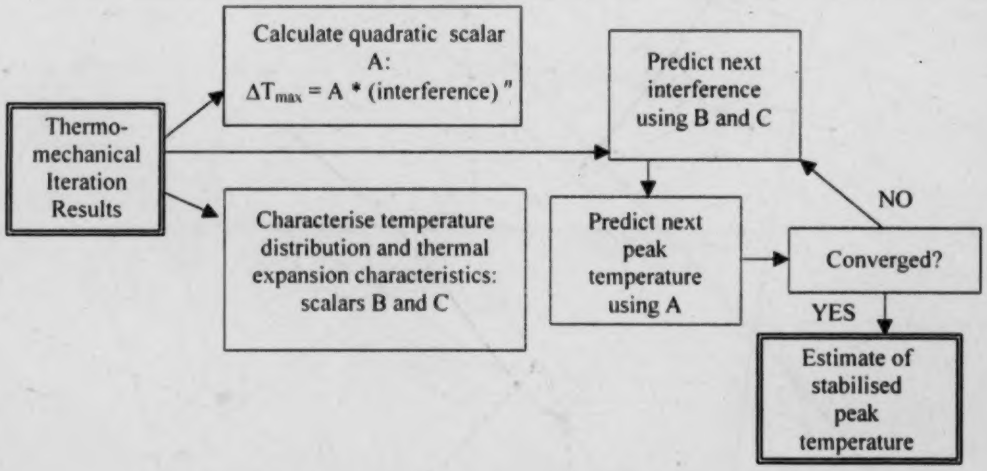
Thermo-mechanical Iteration Results
Calculate quadratic scalar A: $\Delta T_{max} = A * (interference)^n$
Characterise temperature distribution and thermal expansion characteristics: scalars B and C
Predict next interference using B and C
Predict next peak temperature using A
Converged?
NO
YES
Estimate of stabilised peak temperature

Figure 8.9. Convergence optimisation routine flowchart.

Studies that use temperature-insensitive elastomer properties show that the peak temperature at the equilibrium point can be predicted within 5% of the value yielded by the full thermomechanical solution procedure using the spreadsheet model. The spreadsheet model may be integrated into the full thermomechanical solution procedure to expedite convergence. The procedure used in the spreadsheet may be executed after each full thermomechanical iteration. The estimate of the peak equilibrium temperature from the spreadsheet is introduced into the full thermomechanical procedure as an initial guess for the next iteration. The modified temperature field is generated by re-running the thermal analysis with a modified elastomer conductivity, k_e. For models with temperature-insensitive material properties, this method is so effective that only three or four iterations of the full thermomechanical procedure are required to obtain a converged solution that might take ten or more iterations without the optimisation routine. Figure 8.10 shows the optimised convergence pattern for the example thermomechanical analysis presented in Section 8.1. Thirteen iterations are required to satisfy the convergence criterion for the non-optimised solution process, while only five iterations are required for the optimised process.

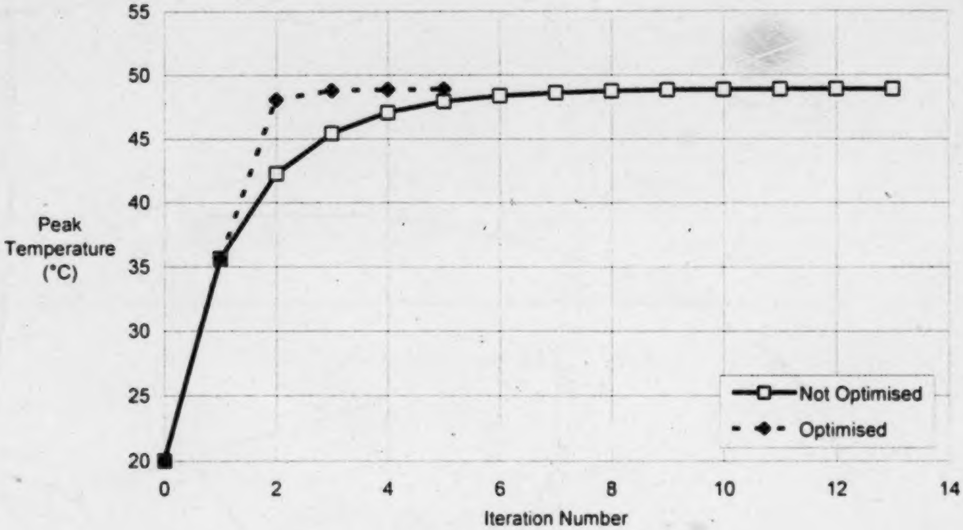

Figure 8.10. Convergence pattern for optimised and non-optimised sample thermomechanical analyses of single-lobe pump with temperature-insensitive material properties.

An added benefit of using the spreadsheet model to optimise the thermomechanical analysis procedure is that diverging solutions may be predicted before divergence occurs. Without the optimised convergence method, a diverging solution cannot be detected until the solution begins to diverge. Using the spreadsheet model as part of the complete thermomechanical procedure provides an early indication that there may not be a stabilised operating point.

9 VERIFICATION TESTING

A key part of any numerical analysis work is verification that the numerical results accurately represent the behaviour of the device being modelled. For this study, the verification procedure involves the instrumentation of a single-lobe progressing cavity pump stator and the execution of a series of full-scale laboratory tests on the unit with parametric variations in the pump speed and rotor/stator interference. Thermo-mechanical analysis results corresponding to each of the test points are generated for comparison purposes. The key variables used for comparisons include the stabilised stator temperature profile and the hoop strain on the outside diameter of the housing.

9.1 Test Objectives

The testing portion of this project provides a verification of the numerical and analytical modelling work discussed in Chapters 4 through 8. While test results were not expected to match the modelling results exactly, enough agreement was expected to provide confidence in the overall modelling strategy. Of particular interest is agreement between predicted and experimental trends with variables that directly affect the hysteresis heat input to the stator elastomer, such as the rotor/stator interference and pump speed.

The structural modelling comparisons described in Section 5.6 show that the two-dimensional approximation to the three-dimensional geometry creates some error in the distribution of distortional strain energy, particularly at low p/d ratios. This is expected to create the largest discrepancy in results between experiment and modelling. In addition, the convective heat transfer description at the inner profile of the elastomer (described in Section 7.4) is a source of uncertainty because of the mixing, undeveloped flow that is thought to occur within stator cavities.

It is difficult to design a test program that can be used to verify the results of each of the individual modelling tasks. Key results of structural modelling such as peak effective stresses, contact stresses, and strain energy densities are difficult to isolate. Verification of heat generation provides a similar challenge, as there is no direct means of measuring hysteresis energy generation in an operating pump. Verification of thermal models is somewhat easier than structural and heat generation models because the temperature field may be measured directly. However, such verification is dependent on knowing the applied heat generation loads, which stem from the structural and heat generation response of the elastomer in this case. The approach used for testing and instrumentation of pumps provides an indicator of the overall suitability of the modelling strategies developed through the course of the study. The primary verification is the stabilised temperature distribution in the stator, which should behave predictably according to the variables that control the structural, heat generation, and thermal responses of the pump.

9.2 Test Program

The testing program consisted of a series of tests that provide representative variations in rotor/stator interference and pump speed. Each pump configuration was run at a constant speed and fluid temperature until a stabilised temperature distribution was achieved. A list of the pump configurations and associated test speeds is shown in Table 9.1. The pump used for verification testing has a p/d ratio of 1.85. One stator was used for all of the tests, while four different rotors provide a range of representative minor interference values of between 50% and 180% of the minor interference in a standard-interference pump.

Test Number	Rotor Number	Nom. Rotor/Stator Interference (% of interference in standard size pump)		Pump Speed (RPM)
		minor (θ = 0°)	major (θ = 90°)	
1	55	50	27	100
2				200
3				300
4				400
5	36	102	133	100
6				200
7				300
8				400
9	54	146	140	100
10				200
11				300
12				400
13	53	180	183	100
14				200
15				300
16				400

Table 9.1. Test program summary.

The test program was designed to verify that the structural modelling provides an adequate estimate of the amount of heat generated for a given interference and to check the sensitivity of the stator to changes in the amount of hysteresis heat generated in the elastomer. All tests provide an indication of the overall suitability of the thermomechanical solution procedure and each of the modelling stages. Comparisons of the predicted and observed relationships between the stator temperature distribution and the rotor/stator interference provide an indication of how well the structural models portray physical behaviour. Results from tests with a single rotor over a range of pump speeds may be compared with predicted trends to verify that the heat generation and thermal modelling strategies are suitable.

9.3 Test Setup and Instrumentation

Figure 9.1 shows a schematic of the setup used for the verification testing. An existing pump test flow loop at Weatherford Artificial Lift in Edmonton accommodated the specific testing and instrumentation objectives required for this project. The rotor numbers shown in Table 9.1 are identification numbers used by Weatherford.

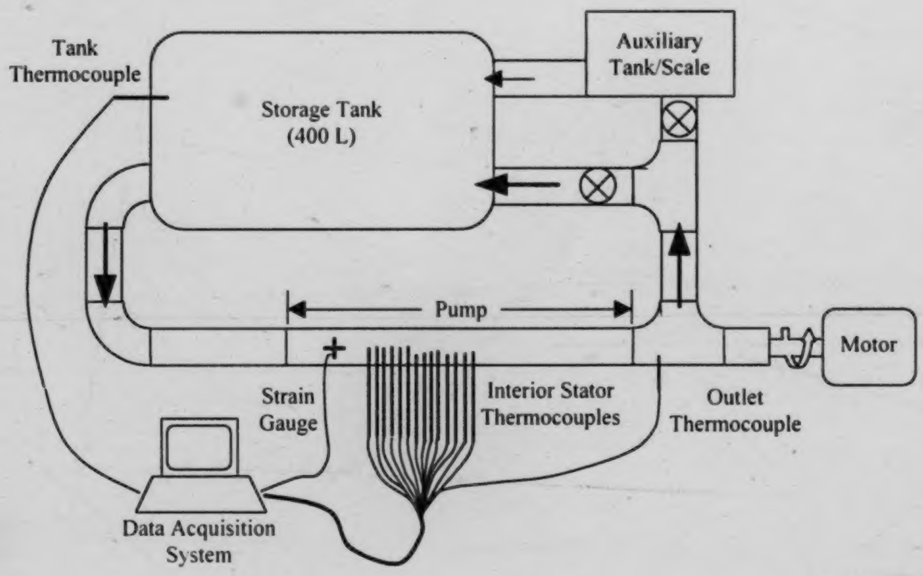

Figure 9.1. Setup for verification testing.

The pump was driven by an electric variable frequency drive system that provided speed control. The torque required of this system was minimal compared to that required in field installations because no pressure differential was applied to the pump. The flow loop included a 400 L tank that acted as a constant-temperature fluid reservoir. This helped to maintain the temperature of the fluid flowing through the pump, allowing a steady-state thermal operating condition to develop within the stator. A source of cold water was also available for mixing with the tank fluid in the event of significant fluid temperature changes during the test.

Some of the instrumentation required was built into the test flow loop. The average flow rate over a given period of time was obtained by measuring the rate of change of mass of the auxiliary tank into which the fluid flows using a data acquisition system. Thermocouples at the storage tank and pump discharge locations provided an indication of the fluid temperature before and after it passed through the pump. A load cell attached to the rotating drive shaft provided a means of measuring applied torque.

The bulk of the measurements used for comparisons were taken on the stator unit itself. The primary comparison variable is the distribution of temperature within the stator cross-section. The stator was instrumented with 18 type-J thermocouples in the locations shown in Figure 9.2. The leads of each thermocouple were spot-welded together to provide a single junction at which the temperature reading occurred. Holes were drilled perpendicular to the inner profile through the stator housing as shown in Figure 9.3 to minimise the cyclic axial load on the thermocouple.

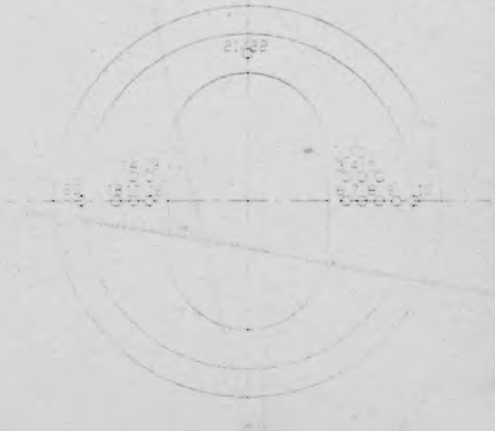

Primary #	Redundant #
1	n/a
2	n/a
3	13
4	14
5	n/a
6	16
7	17
8	18
9	n/a
10	20
21	22

Figure 9.2. Cross-sectional thermocouple distribution. Thermocouples 1 to 10 and 21 were primary thermocouples; the remainder were redundant.

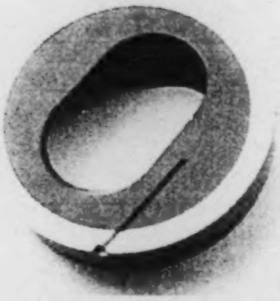

Figure 9.3. Photograph of thermocouple hole in stator cross-section.

A total of eleven different thermocouple locations were used to obtain the temperature profile within the stator. Seven redundant thermocouples were also present in the event of thermocouple failures. In order to minimise the effect of inserting the thermocouples on the stator response, only one thermocouple was used per side of the stator in any given cross-section. Thermocouple holes were drilled no closer than 1/8" from the inner wall of the stator because of the risk of puncturing the elastomer surface. Figure 9.4 shows the axial position of each thermocouple, and Figure 9.5 shows a photograph of the instrumented stator with the installed thermocouples.

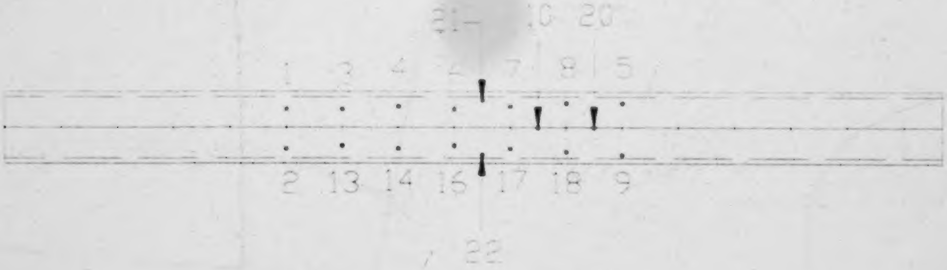

Figure 9.4. Axial thermocouple distribution showing hole locations in plan view.

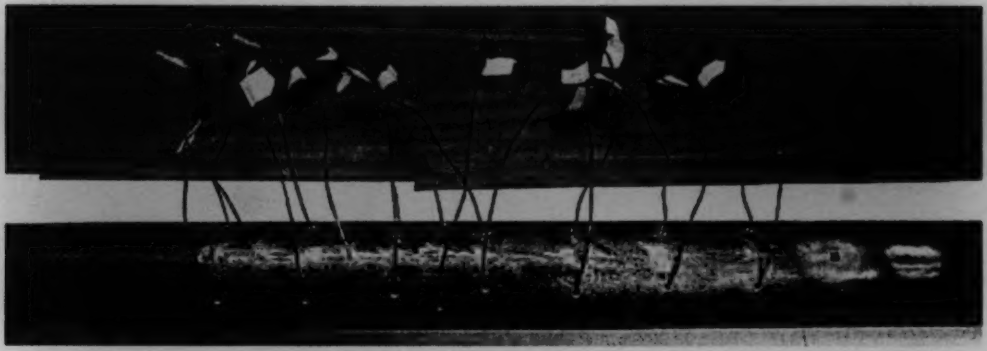

Figure 9.5. Photograph of stator showing thermocouples (along pump length) and uniaxial hoop strain gauge (at right).

A uniaxial foil strain gauge was installed on the outside diameter of the stator housing. This provided a more direct method of verifying structural modelling results than the temperature distribution. A quarter bridge was used to detect strains. Predicted hoop strains resulting from rotor/stator interference were between 2 and 20 microstrain. The measurement system was precise to ±0.75 microstrain.

The stator outside diameter was insulated to remove uncertainties involved with free convective heat transfer to the laboratory environment. This also provided a means of maximising the peak operating temperature increase in the elastomer. Figure 9.6 shows a photograph of the insulated stator on the test bench.

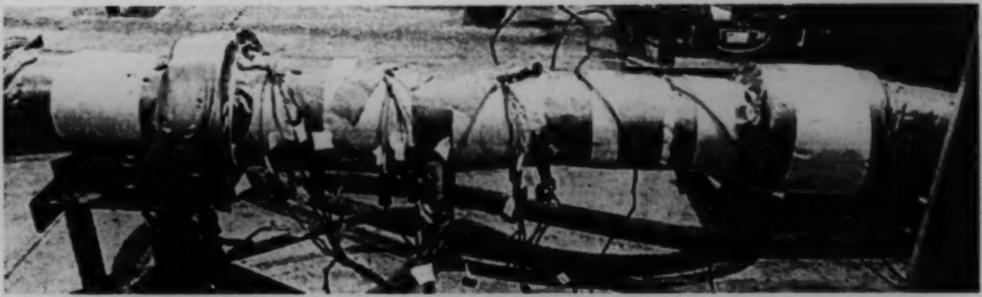

Figure 9.6. Photograph of insulated test stator.

9.4 Test Procedure

Rotors were tested in order of smallest to largest minor interference. For each rotor, the pump was connected to the flow loop and started at the lowest rotational speed, 100 RPM. The temperature of all stator thermocouples and the tank and pump discharge thermocouples was monitored as the test progressed. When all thermocouple readings reached a stabilised temperature, the torque and fluid flow rate were recorded. Typically this took about 1 hour. The speed was then increased to the next value and the procedure repeated. When the 400 RPM test was complete, the speed was reduced to 100 RPM to provide some cooling to the stator elastomer. The rotor was removed and the procedure repeated for the next test rotor. The total duration of the testing work for the four rotors was approximately three days.

Hoop strain measurements on the outside diameter of the housing at the major diameter were obtained after the flow loop testing was completed. The pump was disconnected from the flow loop. The smallest rotor was inserted into the stator with mineral oil acting as a lubricant. Strain readings were taken through a series of rotational steps of approximately 45° each. This procedure was conducted for all rotors except rotor 53, which was too tight to rotate manually. The strain gauge location is shown in Figure 9.7.

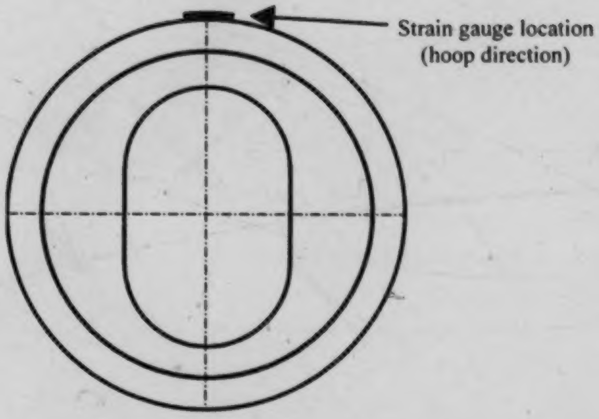

Figure 9.7. Position of strain gauge on housing outside diameter.

9.5 Test Results

All tests proposed were completed as planned. The selected rotor sizes and speeds generated an excellent range of pump responses for comparison with thermomechanical modelling results. Measured changes in the peak elastomer temperature ranged from 1.3°C to 56.7°C.

9.5.1 General discussion

Stabilisation tests were generally on the order of one hour long for each pump speed per rotor. Figure 9.8 shows a typical response history. Steady-state operation was obtained at each of the four operating speeds for rotors 36, 54, and 53. For all tests with these rotors, the inlet fluid temperature was maintained within 0.2°C of 23.0°C.

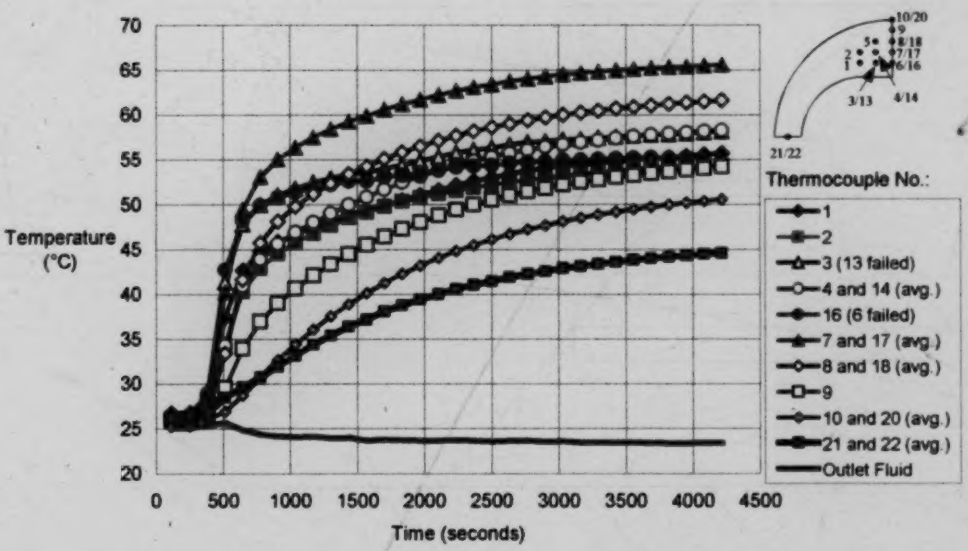

Figure 9.8. Elastomer and outlet fluid temperature readings for rotor 54, 400 RPM; pump speed was increased from rest to 400 RPM at t=400 seconds.

Problems with temperature control were encountered during testing of rotor 55, the first rotor to be tested. An adequate method of maintaining the inlet fluid temperature in the closed-loop system had not yet been established, and fluctuations of up to 1°C were apparent at the pump outlet. The temperature increase in the elastomer encountered during these tests was small and was therefore difficult to distinguish from variations in fluid temperature. While results from the rotor 55 tests are presented herein for completeness, the discussion in the following paragraphs will refer primarily to the other three rotors.

A wide range of transient responses is evident from the thermocouple readings. In general, thermocouples positioned closest to the inner profile of the stator elastomer respond to changes in operating speed much more quickly than those positioned further from the fluid cavity. Tests were run until each thermocouple reading stopped changing noticeably relative to the overall temperature increase. It is estimated that all reported temperature increases at thermocouple locations are within 5% of the steady-state value. This estimate was obtained by fitting an asymptotic exponential function to each of the time history responses of thermocouples 10 and 20, which are located farthest from the stator cavity. The limit of the function as time approaches infinity provides an approximation to the final temperature.

Some discrepancy was evident between thermocouples positioned at identical positions in the stator cross-section relative to the cavity. For instance, with rotor 54 operating at 400 RPM, thermocouples 7 and 17 showed stabilised temperature readings of 43.14 °C and 38.25 °C respectively. This type of discrepancy is common to all redundant thermocouple pairs (e.g., 3 and 13, 4 and 14, etc.) that were inserted into holes drilled parallel to the flat surface of the stator cavity. Figure 9.9 shows that thermocouples 3, 4, 6, 7, and 8 were all on the same side of the stator while the corresponding redundant thermocouples were all positioned on the opposite side. Two possible causes for this behaviour are:

1. The reading may have been affected by the orientation of the thermocouple holes relative to the direction of rotation of the rotor. The rotation of the rotor (and the resulting friction forces at the contact interface) are always in the same direction.

2. The stator cavity may not have been centred in the stator housing. In some cases, the core used to fill the stator cavity during manufacturing may not be concentric with the housing tube, creating an asymmetric geometry. This would affect the position of the thermocouples relative to the cavity and the structural and thermal responses of the stator elastomer.

The discrepancy in thermocouple readings may be tied to one or both of these phenomena. No attempt was made to verify if this was the case. Reported temperature readings for all thermocouple pairs are the average of the two readings when both thermocouples were working.

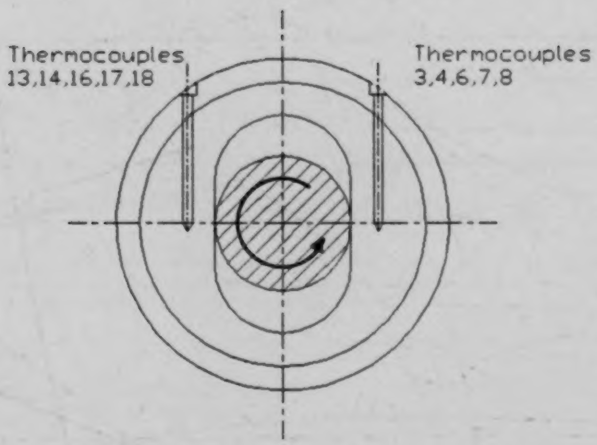

Figure 9.9. Orientation of thermocouple holes relative to direction of rotor rotation.

Numerous thermocouples stopped responding during the 300 and 400 RPM tests of rotors 53 and 54. Thermocouples that failed were primarily those positioned nearest to inner profile of the stator. An examination of the failed thermocouples suggests that the cyclic loads applied to the elastomer by the motion of the rotor may be transferred to the thermocouples, causing fatigue failures in the leads and the spot weld that joins the leads. Thermocouples were replaced after the completion of each test as required.

9.5.2 Peak stabilised temperatures

Temperatures in the elastomer reached values of up to 56°C above the fluid temperature in the most extreme loading case. The peak temperature increase in the stator elastomer is shown for all four rotors as a function of pump speed in Figure 9.10. All temperatures are reported relative to the fluid temperature at the pump outlet. The temperature increase appears to vary linearly with pump speed.

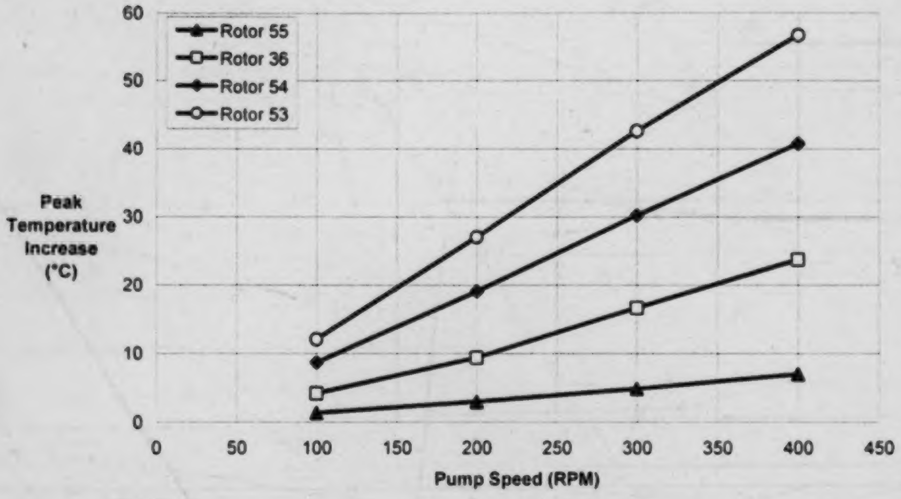

Figure 9.10. Test results showing relationship between pump speed and peak elastomer temperature change for four rotors.

The linear trend between pump speed and peak elastomer temperature shown in the above figure is the result of a number of counteracting factors that appear to balance one another. The response of nitrile rubber is such that the loss tangent, tan δ, increases with temperature and acts to generate more heat than would be described by a linear relationship between speed and hysteresis energy. Another factor that acts to magnify the quantity of heat generated with increasing speed is the increase in rotor/stator interference that accompanies higher temperatures. These effects are counteracted by the fact that the stiffness of the elastomer decreases with increasing temperature, reducing the amount of hysteresis energy generated per unit strain. If the structural material properties of the elastomer were not sensitive to temperature and the material did not incur any thermal expansion, the trend would also be linear. A generalisation to the overall response of single-lobe pumps to increasing pump speed is thus not possible from the test results because the linear relationship stems partly from elastomer material properties.

The peak elastomer temperature increase results presented in Figure 9.10 are shown in Figure 9.11 as a function of the nominal rotor/stator interference. The relationship between interference and peak temperature is nonlinear at all four speeds. At higher interferences, more temperature change results per unit interference.

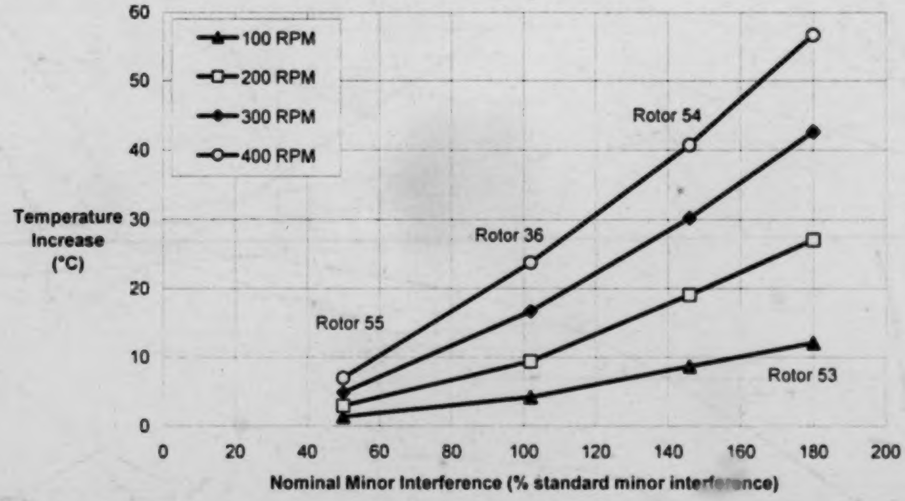

Figure 9.11. Test results showing relationship between nominal minor interference and peak elastomer temperature change at four speeds.

The nonlinear relationship between interference and temperature increase is partially governed by the series of counteracting factors identified in the preceding paragraphs. In Section 8.2.5, it was found that the peak temperature is expected to increase as a quadratic function of the interference in the absence of temperature-sensitive material properties. The introduction of variations in the loss coefficient and stiffness with temperature mean that this is not necessarily true.

Another factor that governs the relationship between interference and temperature increase is the degree to which the cross-sectional rotor path is elliptical (refer to Chapter 5). In one cycle of the rotor, the rotor contacts a point on the stator profile at the minor diameter twice. If the rotor path is elliptical, the interference that occurs is not the same for both contact events. Hence, a path that is not at all elliptical may generate a different peak temperature than one with a high eccentricity offset. While Figure 9.11 relates the temperature increase to the nominal interference, Figure 9.12 presents the test results in terms of the radial minor interference predicted by 3D models of the test rotors. The reported interference is taken at the rotor/stator contact point on the high-interference side of the cavity. The relationship between actual interference and temperature change appears to be more nonlinear than if the nominal interference values are used as the comparison basis.

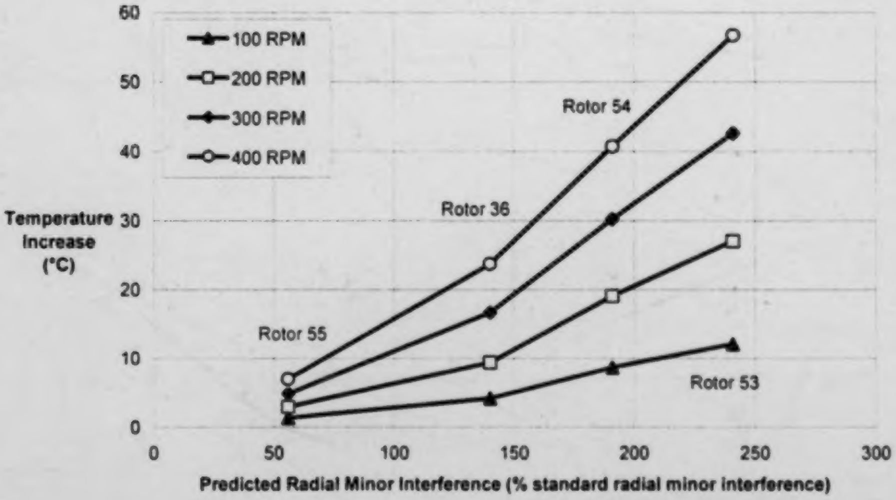

Figure 9.12 Test results showing relationship between radial minor interference predicted by 3D model and peak elastomer temperature change at four speeds.

9.5.3 Stabilised temperature distributions

Temperatures were measured at different points in the elastomer so the peak temperature could be found and so that the temperature profile in the stator could be compared to the profile predicted using the thermomechanical modelling strategy. Profiles from rotors 36, 54, and 53 showed consistent trends, while those from rotor 55 reflect the fact that the stabilised operating point had not been reached when the tests were stopped.

Figure 9.13 shows an example of the stabilised temperature profile in the stator. Temperature profiles are shown along three lines perpendicular to the straight section of the cavity along with the temperature halfway through the elastomer thickness at the major diameter. Temperatures through the thickest section of the elastomer are higher than those through the other sections.

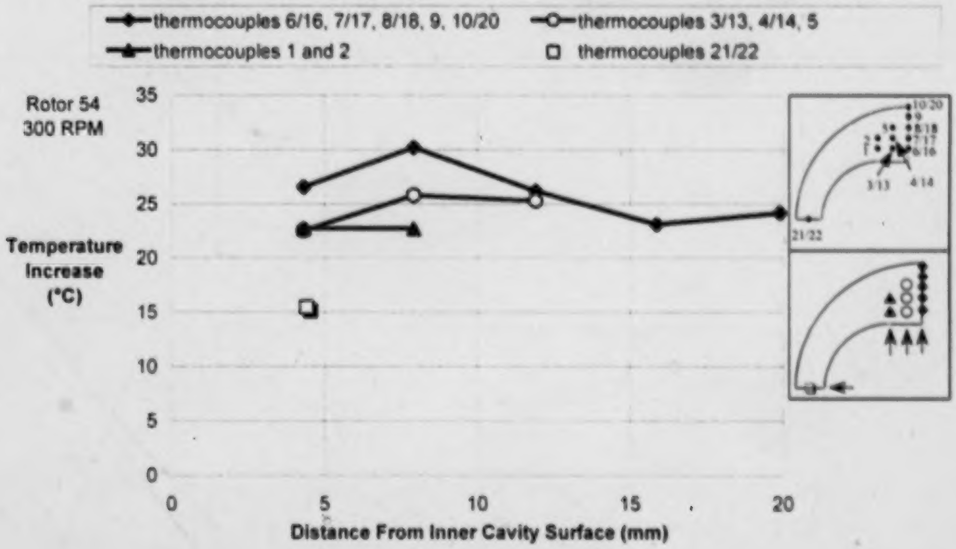

Figure 9.13. Stabilised elastomer temperature profiles for rotor 54 at 300 RPM.

The location of peak temperature and the temperature gradient in the elastomer is governed by the heat flux through the elastomer and the distance the heat must travel to reach the convective boundary at the stator cavity. The thickest part of the elastomer is the region of highest heat generation in the cross-section. Because of this, more heat must travel through a greater distance to reach the convective fluid boundary, causing a higher temperature in the thick section. It is unfortunate that readings closer to the inner surface of the stator were not possible, as the surface temperature would provide an indication of the temperature gradient near the surface and a better understanding of the convective boundary condition for thermal modelling.

The temperature profile observed through the thickest section of elastomer retained the same shape when the speed and interference were changed. Figure 9.14 shows the temperature profile through the thickest part of the elastomer for rotor 54 at four speeds. While the magnitude of the temperature increase changes with speed, the relative magnitudes of the temperatures along the profile remains similar. This is more easily seen in Figure 9.15, which shows the temperature profile for each speed normalised to the peak temperature at that speed.

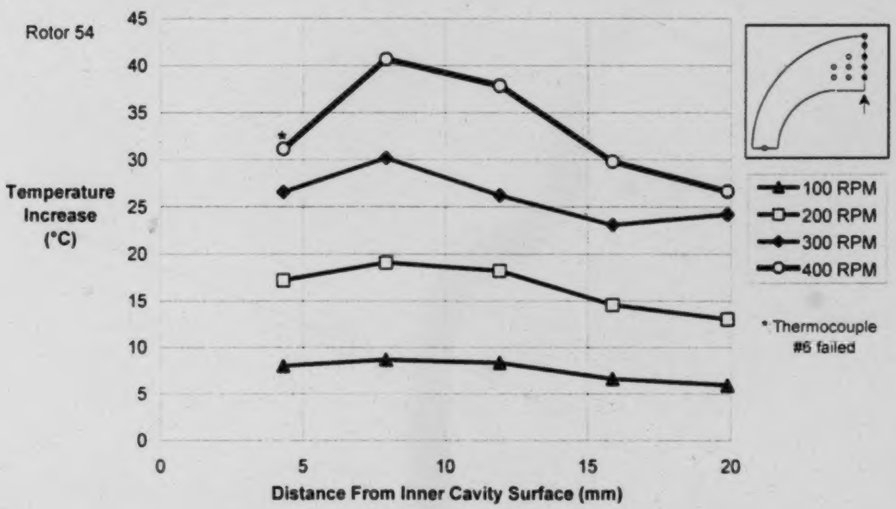

Figure 9.14. Stabilised temperature profile through thickest section of elastomer for rotor 54 at four speeds.

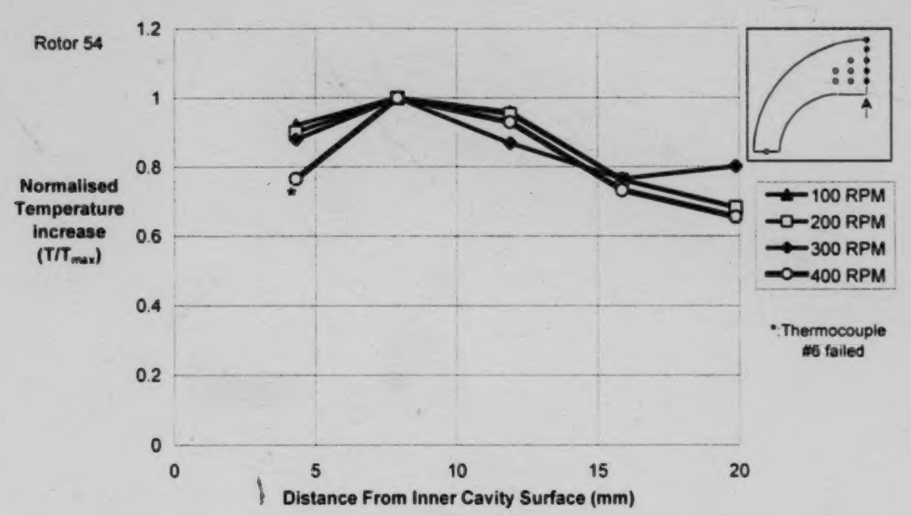

Figure 9.15. Stabilised temperature profile through thickest section of elastomer for rotor 54 at four speeds, normalised to peak temperature at each speed.

Figure 9.16 shows the stabilised temperature profile through the thickest section of the elastomer for the four rotors operating at 300 RPM. The same data is presented in Figure 9.17 with the temperatures normalised to the peak temperature. It is evident that the temperature profile in the stator is very different for the loosest rotor, rotor 55. This is likely a result of the stator not reaching a stabilised operating point. Profiles from the other three rotors are similar.

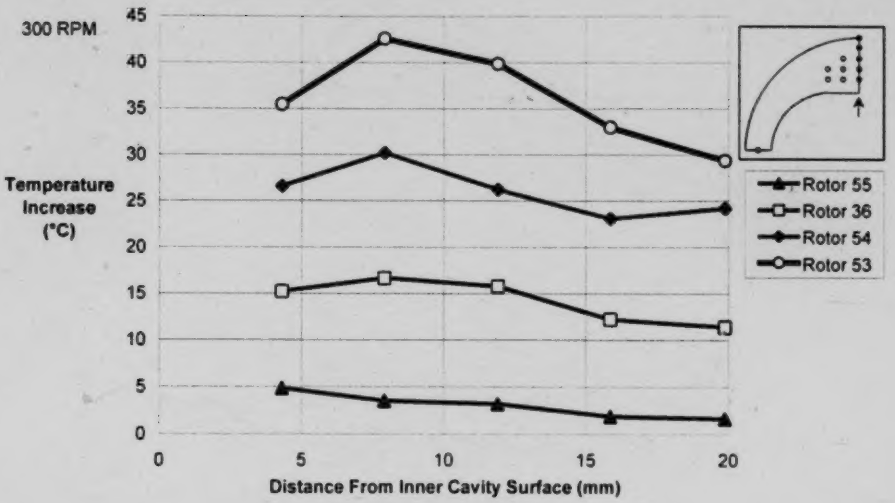

Figure 9.16. Stabilised temperature profile through thickest section of elastomer at 300 RPM for four rotors.

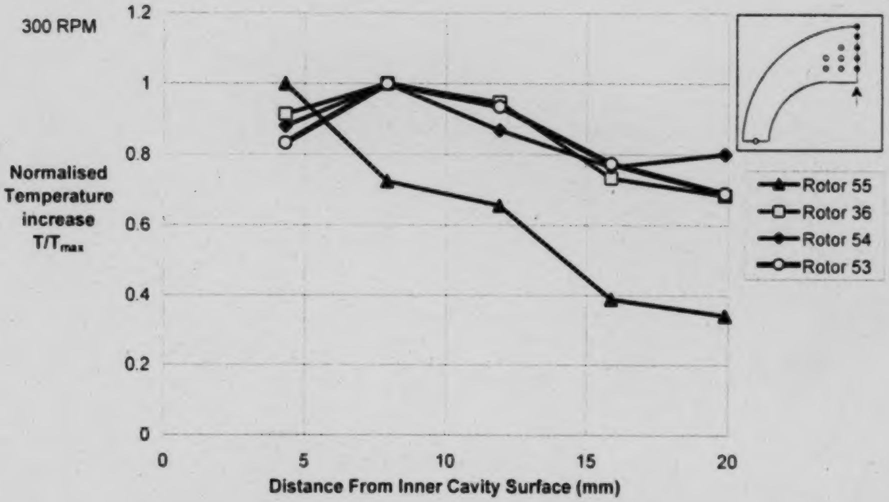

Figure 9.17. Stabilised temperature profile through thickest section of elastomer at 300 RPM for four rotors, normalised to peak temperature for each rotor.

9.6 Comparison to Thermo-Mechanical Modelling Results

Results from the stabilisation tests completed using rotors 36, 54, and 53 may be used to gauge the suitability of the modelling procedures described in Chapters 5 through 8. Results from tests performed with rotor 55 are presented, but it should be kept in mind that the stator did not reach its stabilised operating point. A total of 16 thermomechanical analyses corresponding to each rotor/speed combination in the test program were conducted for comparison purposes.

Structural models were created so that the eccentricity offset was accounted for in the rotor path using the method presented in Section 5.6. Frictional effects were ignored. Tensile stiffness response was obtained from samples of the nitrile rubber used to make the pump. Dynamic material properties for use with the heat generation model were obtained over a representative range of frequencies and temperatures. A thermal expansion coefficient of 0.00016 1/°C was used. Thermal properties specific to the test elastomer were not available, but Hoffmann[25] lists a thermal conductivity value of 0.25 W/m·K for nitrile rubbers.

9.6.1 Stabilised temperature comparisons

Table 9.2 shows a summary of the peak temperatures obtained from the thermomechanical analyses and the associated test results. The accuracy of the predictions varies for each rotor and each speed. The majority of predictions underestimate the temperature increase. The measured peak temperature increase is underestimated by as much as 70% for the loosest rotor (number 55). The best agreement occurs with the tightest rotors (numbers 54 and 53), where the predicted temperature is as close as 9% of the measured value. In absolute terms, the maximum error is on the order of 12°C. Figure 9.18 shows a graphical comparison of the measured and predicted peak temperature increase for all of the tests.

Rotor Number	Pump Speed (RPM)	Peak Elastomer Temperature Increase (°C)		Error	
		test result	modelling result	(°C)	(%)
55	100	1.3	0.7	-0.7	-50.7
	200	3.0	1.2	-1.8	-60.5
	300	4.9	1.6	-3.2	-66.5
	400	7.0	2.1	-4.9	-70.7
36	100	4.2	3.2	-1.1	-25.0
	200	9.4	6.1	-3.3	-35.5
	300	16.7	9.0	-7.7	-46.0
	400	23.7	12.2	-11.5	-48.4
54	100	8.7	7.7	-1.0	-11.3
	200	19.1	16.1	-3.0	-15.5
	300	30.2	25.7	-4.5	-15.0
	400	40.7	37.3	-3.4	-8.3
53	100	12.1	13.4	1.3	11.1
	200	27.1	29.4	2.3	8.4
	300	42.6	47.1	4.5	10.6
	400	56.7	66.8	10.1	17.8

Table 9.2. Comparison of peak stabilised elastomer temperature increases obtained from testing and modelling.

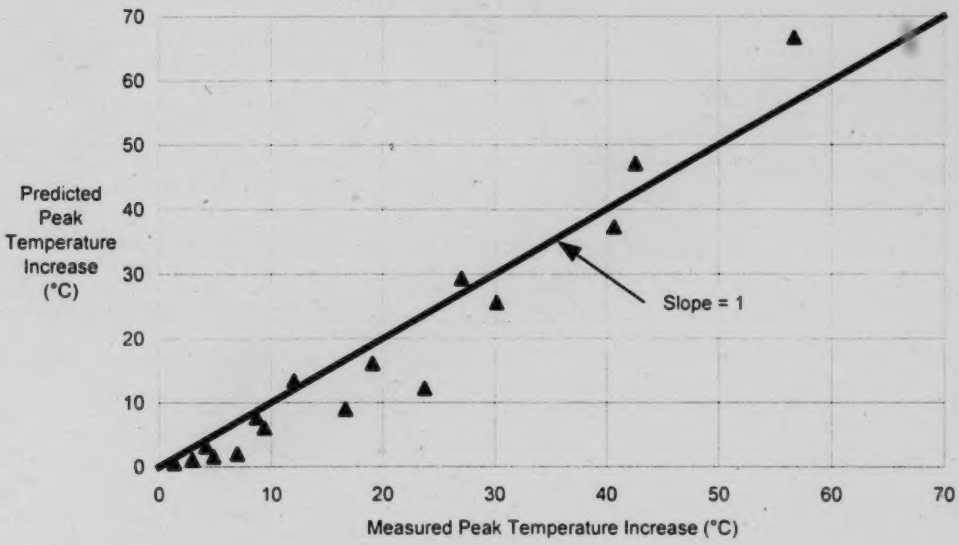

Figure 9.18. Comparison of peak predicted and measured temperature increases in the stator elastomer.

The testing program provides an indication of the sensitivity of pump response to the pump speed and the rotor/stator interference. The errors in predicted peak temperature values may be examined in terms of these sensitivity variables. Figure 9.19 shows the relationship between the measured peak temperature increase and the error in the predicted temperature as a function of pump speed. It is clear that there is no strong relationship between the speed and the error in the predicted temperature. Table 9.3 shows that for each of the four test speeds, the range of errors in the predicted temperature is at least 60%.

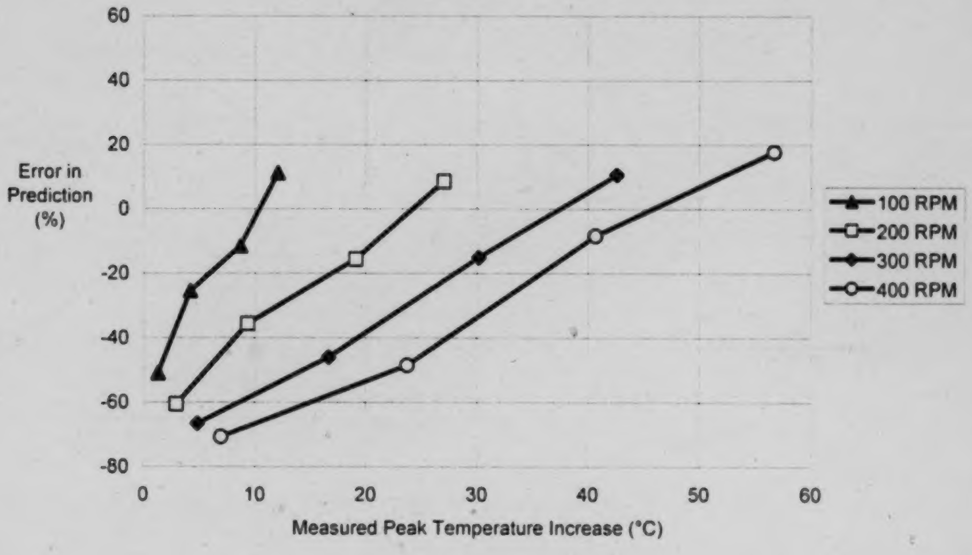

Figure 9.19. Errors in predicted temperature increase showing weak correlation between pump speed and error.

Pump Speed (RPM)	Range of Error in Peak Temperature Increase
100	-50.7% to 11.1%
200	-60.5% to 8.4%
300	-66.5% to 10.6%
400	-70.7% to 17.8%

Table 9.3. Range of error in predicted temperature increase for four speeds.

Figure 9.20 and Table 9.4 show that there is a strong correlation between the error in the predicted temperature increase and the rotor used for the test. While errors for rotor 55 (the loosest rotor) range from −70% to −50%, the magnitude of errors appears to decrease for tighter rotors.

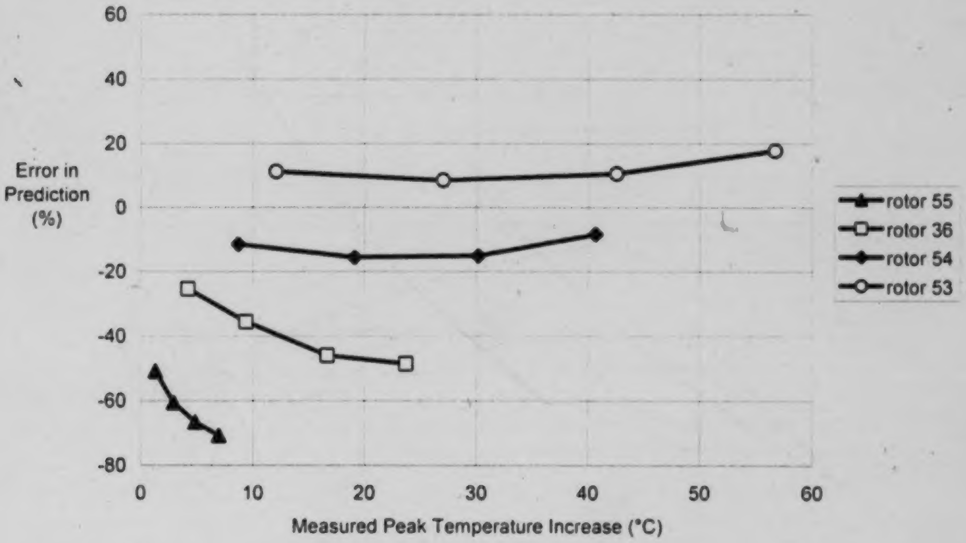

Figure 9.20 Errors in predicted temperature increase as a function of rotor number showing a strong correlation between error and rotor number.

Rotor Number	Range of Error in Peak Temperature Increase
55 (loosest)	-70.7% to -50.7%
36	-48.4% to -25.0%
54	-15.5% to -8.3%
53 (tightest)	8.4% to 17.8%

Table 9.4. Range of error in predicted temperature increase for rotors.

The error in the predicted temperature increase varies approximately linearly with the minor interference, as shown in Figure 9.21. Assuming that this trend applies to the full range of possible interferences, it may be concluded that there is a shortcoming in some part of the modelling or testing description that relates directly to the rotor/stator interference. The following paragraphs attempt to identify this error more closely.

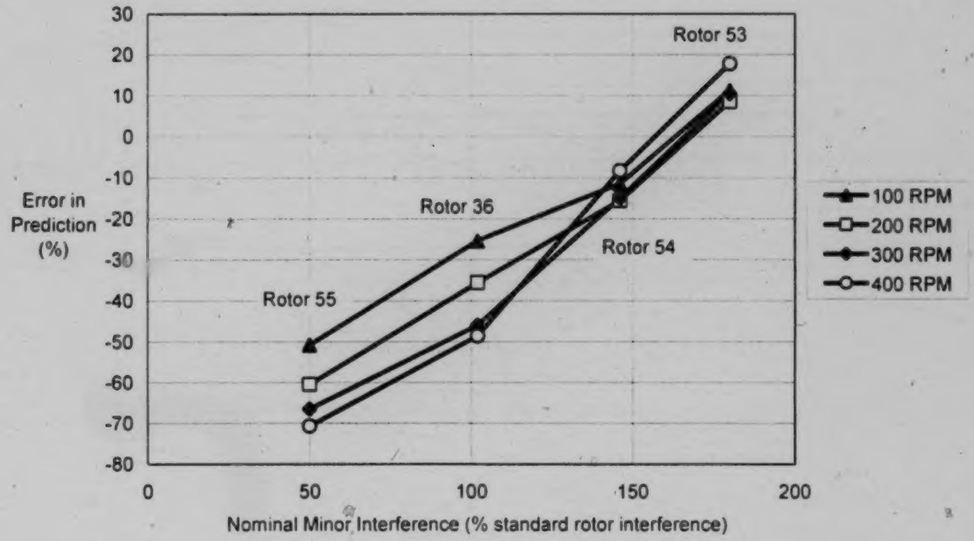

Figure 9.21. Error in peak temperature prediction as a function of rotor/stator interference.

In Section 9.5.2, general trends in the response of the test stator to speed and interference are identified. The peak temperature increase is a linear function of the pump speed for each test rotor, while the relationship between interference and peak temperature increase is nonlinear. The predicted thermomechanical response may be analysed in the same fashion.

Figure 9.22 shows the relationship between the rotor/stator interference and the peak temperature predicted by the thermomechanical model. As with the test results, the relationship is nonlinear. The normalised temperature increase, T_{norm}, is defined as the ratio of the peak temperature increase at a given rotor/stator interference, T, to the peak temperature increase for rotor 53 at the same pump speed, $T_{Rotor\ 53}$,

$$T_{norm} = \frac{T}{T_{Rotor\ 53}}. \qquad [9.1]$$

The normalised temperature increase provides a simple method of examining the trend in temperature change with interference for all four speeds. Figure 9.23 shows that the normalised temperature increase with interference is the same for each speed.

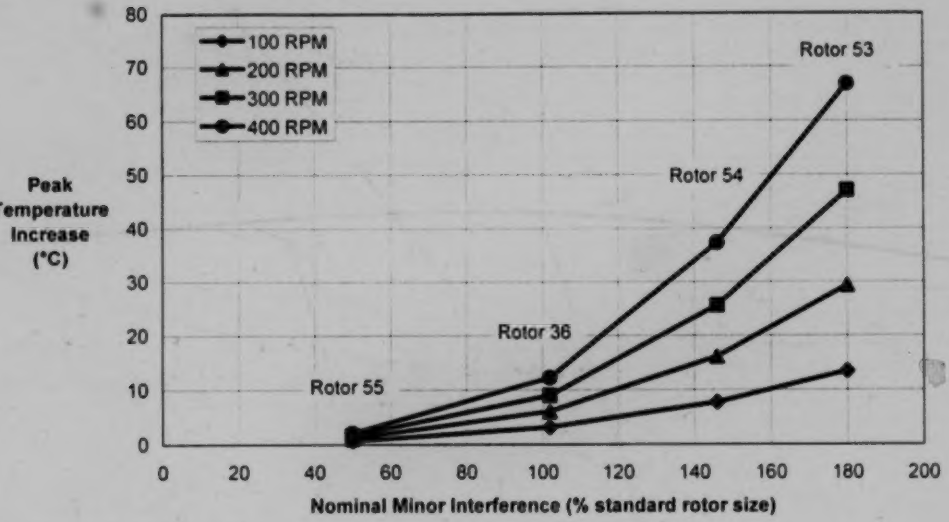

Figure 9.22. Predicted peak temperature increase as a function of pump speed.

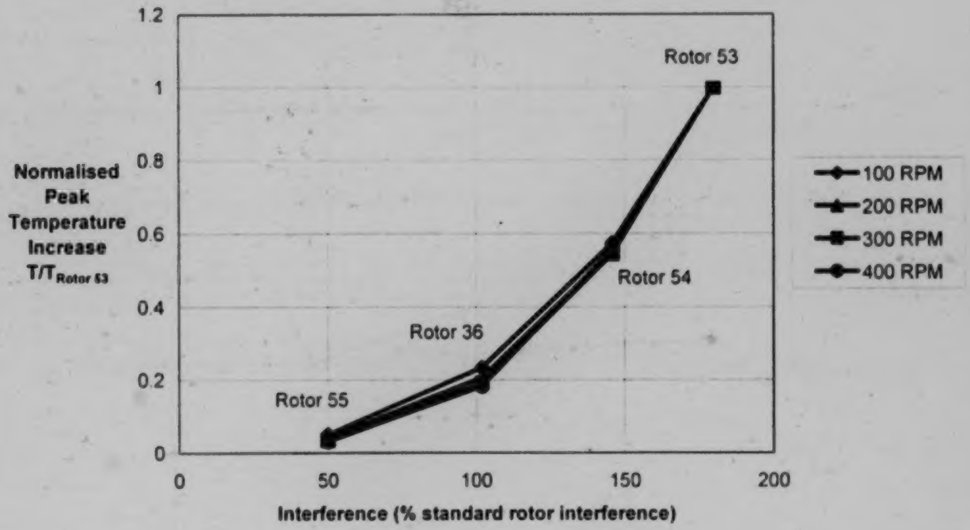

Figure 9.23. Trend in predicted temperature increase with pump speed, normalised to 400 RPM.

A comparison of the trends in temperature increase with interference from modelling and testing is shown in Figure 9.24. This figure provides a good indication of the nature of the errors observed in the modelling results. In Section 8.2.5, it is shown that the relationship between rotor/stator interference and peak temperature increase may be related by the power-law relationship

$$\Delta T_{max} = A \cdot interference^{n}, \qquad [9.2]$$

where n is equal to approximately 2 when material properties are not sensitive to temperature changes. A similar description may be used to characterise the testing and modelling results. If the relationship between the interference and the normalised peak temperature increase is fit to a power-law description for the testing and modelling results, it is found that n is 1.70 for the testing results and 2.53 for the modelling results. It should be noted that in this case, the relationship shown in Equation 9.2 relates the temperature to the initial rotor/stator interference rather than the interference in the deformed configuration. As it was not possible to measure the interference change during testing, the values of n should not be compared to the value of 2 obtained from the temperature-insensitive thermomechanical models in Section 8.2.5.

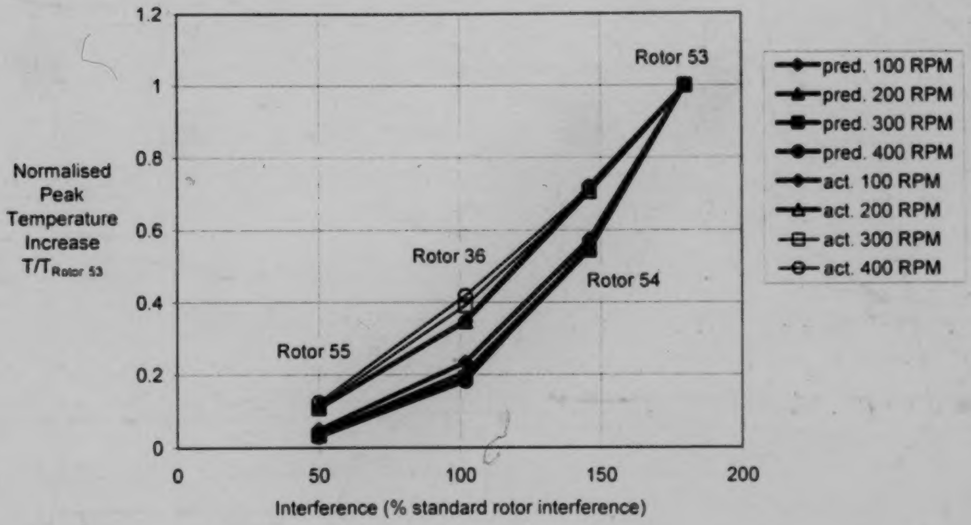

Figure 9.24. Comparison of predicted and actual trends in peak temperature increase with interference.

The power-law relationships described above show that the discrepancy between trends of predicted and measured peak temperature increase with interference is independent of test speed. Possible sources for the discrepancy between testing and modelling results are discussed in Section 9.6.4.

9.6.2 Temperature profile comparisons

Figure 9.25 shows the predicted and observed temperature profiles through the elastomer thickness at the minor seal for rotor 54 running at 300 RPM. As indicated in Section 9.6.1, the peak temperature change predicted by the thermomechanical model underestimates the peak measured temperature by 4.5°C (15%). However, the shape of the predicted temperature profile appears to be similar to that of the observed temperature profile. Figure 9.26 shows the same temperature profiles normalised to the peak temperature for each set of results. The predicted peak temperature is approximately 2 mm (10% of the elastomer thickness) further from the inner elastomer surface than the observed peak temperature.

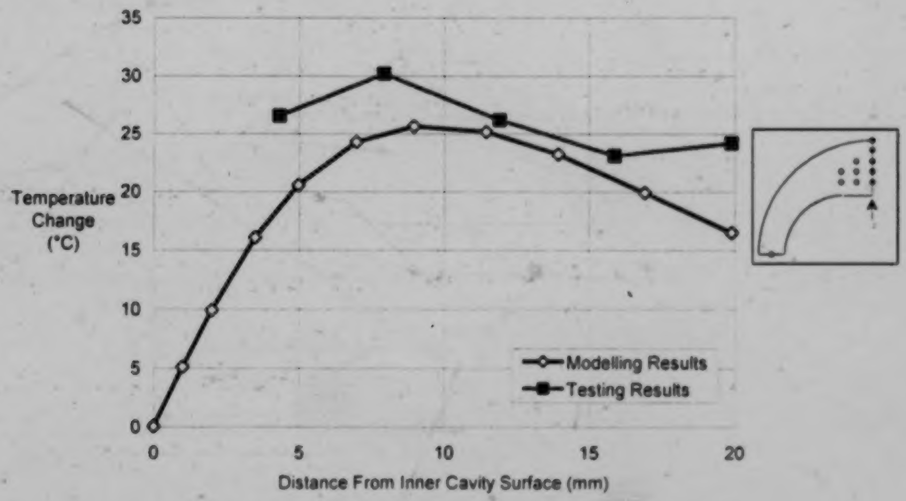

Figure 9.25. Comparison of predicted and measured temperature profiles through elastomer thickness at minor seal.

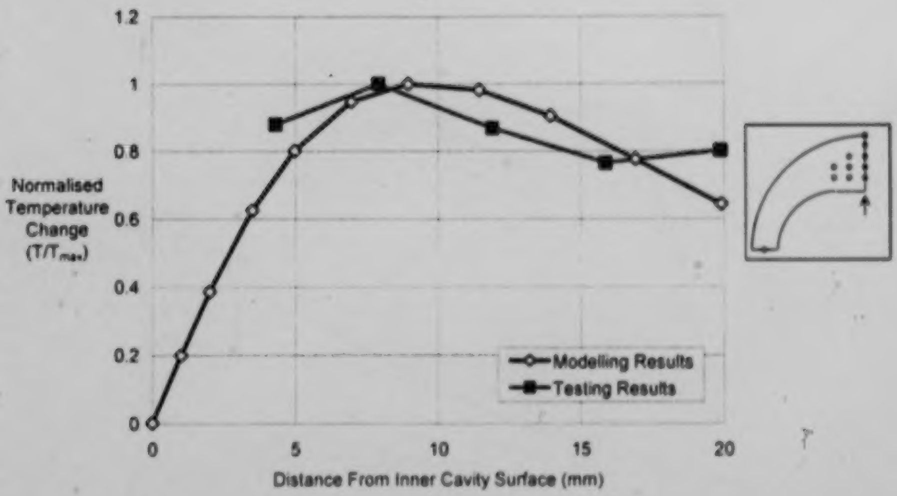

Figure 9.26 Comparison of normalised predicted and measured temperature profiles through elastomer thickness at minor seal.

The agreement between the measured and predicted temperature profiles is encouraging. It provides an indication that the predicted distribution of hysteresis heat is similar to the actual behaviour and that the thermal modelling strategy correctly describes the heat transfer behaviour within the pump.

9.6.3 Hoop strain comparisons

Hoop strain measurements were taken on the outside diameter of the stator in an effort to provide an independent means of verifying that the static structural modelling accurately represents the actual static response of the stator. Table 9.3 provides a summary of the measured and predicted strains obtained from the tests. Measurements were not obtained for rotor 53 because the interference was too high to manually rotate the rotor.

rotor	hoop strain at major diameter (microstrain)		error in prediction (%)
	measured	predicted (3D)	
55	5.80	1.27	-78.10
36	10.30	11.14	8.16
54	14.00	13.22	-5.57
53	N/A		

Table 9.5. Comparison of measured and predicted hoop strains at gauge on outside diameter of housing at major diameter.

While peak measured strains for rotors 36 and 54 are within 10% of the predicted value, the predicted strain for rotor 55 underestimates the measured value by almost 80%. All observed strain magnitudes are extremely small and may have been susceptible to a number of sources of error. The error due to fluctuations in the output voltage in the bridge is estimated at +/-0.75 μs. While care was taken in obtaining the measurements, any load applied to the stator housing may also have created additional strain at the gauge location that was not a result of the rotor/stator interference. It is important to note that the observed strain from rotor 55 is much greater than the predicted value. Also recall that the thermomechanical analysis results for this rotor underestimated the peak temperature increase by betweeen 50% and 70%. It is possible that the same factors that affect the hoop strain may contribute to the error in the thermomechanical results. An investigation of the sensitivity of the thermomechanical response to changes in key modelling variables (see Section 9.6.4) shows that the thermomechanical response is very sensitive to rotor/stator interference, particularly when the rotor/stator interference is small.

9.6.4 Error identification

Given the discrepancy between some of the predicted and measured peak temperature values and the observed trends between rotor/stator interference and temperature increase, it is important to try to identify possible sources of error. These can be divided into errors that could have resulted from the modelling process and those that may have arisen from the testing procedure. The discrepancy between modelling and testing results is likely a combination of a number of these factors.

Errors in predicted peak temperature could be a result of the following:

1. Incorrect description of rotor and/or stator geometry. Typical variations in the minor and major diameters along the length of the rotor are ±4% of the nominal minor interference of a standard rotor. For the loosest rotor tested (rotor 55), the potential error is ±8% of the minor interference and ±30% of the major interference. Similar variations may be present in the major and minor stator diameters. It was also assumed that the stator geometry was measured at 20°C, whereas the actual temperature when the stator was measured may have been as high as 27°C. Modelling suggests that this expansion could create an underestimation of the minor interference in the thermomechanical model of as much as 11% for the loosest rotor, #55.

2. Incorrect rotor path. The rotor path within the stator cavity is governed by the geometry of both components. If the geometry description is incorrect, it is unlikely that the rotor path used for modelling will be representative of the actual path.

3. Non-concentric stator cavity. It is possible that the cavity position within the stator elastomer was not perfectly centred because of deflection of the core during the elastomer forming process or thickness variations in the stator housing tube. This would cause the rotor to move in a different path than expected and would result in different structural and thermal responses on either side of the stator.

4. Two-dimensional approximation to three-dimensional geometry. The helical three-dimensional geometry of the pump is modelled using two-dimensional thermal and structural models. While an attempt was made to benchmark 2D models for heat generation modelling using the results of 3D structural models, some error is still possible. In Section 5.6, it is

shown that the biggest discrepancy between 2D and 3D models can be expected for low p/d ratios. The p/d ratio of the test pump is 1.85, very low for a single-lobe pump.

5. Incorrect structural or thermal material property descriptions. The results of the thermomechanical modelling procedure are very sensitive to the material properties used for modelling, as shown later in this chapter. Errors in the small-strain elastic modulus of the elastomer over a range of temperatures may cause errors in the stress response of the elastomer for an applied strain field. Errors in the loss tangent, tan δ, over a range of temperatures and frequencies would lead to an incorrect description of the amount of heat generated for a given stress and strain field. The thermal conductivity of the elastomer dictates the temperature increase for a given heat flux in the elastomer. Errors in this quantity could cause significant errors in the resulting temperature field even if the structural and heat generation models provide accurate results. Similarly, errors in the thermal expansion coefficient of the elastomer would lead to an incorrect description of the deformed geometry at the operating temperature and would create an error in the amount of interference resulting from hysteresis heating.

Errors resulting from the testing program could include some or all of the following:

1. Intrusive temperature measurement technique. The stator geometry was modified somewhat because of the presence of the thermocouple hole. While localised stress and strain fields in the vicinity of the thermocouple were likely affected by the hole, it is unlikely that the global stator response was changed.

2. Incorrect thermocouple positioning. Thermocouple holes were positioned and drilled to a specified depth using a precision milling machine, but the positions of the thermocouple junctions within the stator were difficult to verify.

3. Thermocouple accuracy. The accuracy of the thermocouples is estimated to be ±0.8°C. The accuracy of a single thermocouple is not expected to change over the range of operating conditions.

The errors discussed in Section 9.6.1 include absolute and relative temperature variations. It is likely that the factor(s) contributing to the errors are dependent on the operating conditions. For instance, part of the discrepancy between the measured and predicted interference/temperature relationships shown in Figure 9.24 is likely a result of the accuracy of the temperature-sensitive material property description. However, this is not the case when temperature increases are small. At low interferences, the stator response would be more sensitive to the uncertainty in the geometrical description of the rotor and stator used for modelling.

As it is difficult to isolate the amount of error that results from errors in the modelling strategy, a series of additional thermomechanical analyses were conducted to gauge the sensitivity of the predicted results to some of the error sources listed above. These analyses provide an indication of how much of the error in the predicted temperature increase could have resulted from improper modelling descriptions. Table 9.6 shows a list of the additional thermomechanical analyses conducted.

Analysis	Variable	Original Value	Change From Original	Rotor	Notes
1	minor interference	50% standard int.	+20%	55	Rotor major diameter is unchanged
2		180% standard int.	+6%	53	
3	thermal expansion coefficient, α	0.000160 1/°C	+0.000016 1/°C	53	
4	thermal conductivity, k	0.25 W/m/K	-0.025 W/m/K	55	
5				53	
6	$\tan\ \delta$ at 20°C	confidential[1]	+10%	55	Slope with temperature is unchanged
7	slope of $\tan\ \delta$ vs. temperature curve	confidential[1]	-10%	53	$\tan\ \delta$ value at 20°C is unchanged
8	elastomer stiffness at 20°C	confidential[1]	+10%	55	Temperature-sensitivity relationship scaled with stiffness
9		confidential[1]		53	

Table 9.6. Thermomechanical analyses conducted for error identification. All analyses were conducted at 400 RPM.

Variables used for the sensitivity study include the minor interference between the rotor and stator, the thermal expansion coefficient of the elastomer, the thermal conductivity of the elastomer, the loss tangent of the elastomer, and the elastic modulus (stiffness) of the elastomer. In each case, a single variable was changed while the remainder of the values were fixed at the values used for the original analyses. Each variable was changed by 10% except the minor interference, which was changed by 20% for rotor 55. Results of the study are presented in Table 9.7 and discussed in the following paragraphs.

---

[1] Material properties were measured by Weatherford Artificial Lift and are confidential.

Analysis	Variable	Change in Variable	Rotor	Peak Temperature Increase (°C)			Change in Predicted Temperature Increase (%)	Error in prediction (%)	
				Original Prediction	New Prediction	Test Result		Original Prediction	New Prediction
1	minor interference	+20%	55	2.05	3.45	6.99	68.4	-70.7	-50.6
2		+6%	53	66.78	74.06	56.71	10.9	17.8	30.6
3	thermal expansion coefficient, α	+10%	53	66.78	74.31	56.71	11.3	17.8	31.0
4	thermal conductivity, *k*	-10%	55	2.05	2.32	6.99	13.2	-70.7	-66.8
5			53	66.78	77.50	56.71	16.0	17.8	36.7
6	*tan δ* at 20°C	+10%	55	2.05	2.24	6.99	9.3	-70.7	-68.0
7	slope of *tan δ* vs. temperature curve	-10%	53	66.78	62.27	56.71	-6.8	17.8	9.8
8	elastomer stiffness at 20°C	+10%	55	2.05	2.28	6.99	11.2	-70.7	-67.4
9			53	66.78	76.47	56.71	14.5	17.8	34.8

Table 9.7. Results of thermomechanical analyses conducted for error identification.

Interference considerations are addressed in the first two analyses. As indicated previously, there may be a significant error in the modelling description of the rotor and/or stator geometry. To gauge the sensitivity of the model to changes in interference, an increase of 20% in the minor interference of rotor 55 is reasonable given the uncertainty in rotor and stator geometries. The diameter of rotor 36 is larger by the same amount, changing the overall interference by 6%. The predicted temperature change for rotor 55 increases by 68.4% to 3.45°C. This reduces the error in the prediction from approximately 70% to 50%. The same interference change in the large rotor causes an increase of about 11% in the peak predicted temperature, increasing the error in the prediction from 17.8% to 30.6%. Errors in the geometrical description of rotors with lower interferences clearly have a bigger impact on the error in predicted elastomer temperature.

The effect of changing the thermal expansion coefficient is only investigated for rotor 53 (sensitivity analysis 3) because of the relatively small temperature change expected with rotor 55. A 10% increase in the thermal expansion coefficient causes an increase of 11.3% in the predicted temperature change. This increase occurs because the elastomer expands more for a given amount of hysteresis heating. The effect of reducing this expansion coefficient by the same amount would likely cause an equivalent decrease in the temperature change. This may be responsible for part of the discrepancy between testing and modelling results at higher temperatures.

The thermal conductivity of the test elastomer is obtained from Hoffmann's discussion[25] of the properties of nitrile rubber. This thermal material property dictates the temperature gradient through the elastomer for a given heat flux. Sensitivity analyses 4 and 5 show that reducing the conductivity by 10% creates an increase in the peak temperature change of 13% for rotor 55 and 16% for rotor 53. This may explain part of the modelling error for low-interference rotors, but it clearly has the same effect for rotors with high interference.

The loss tangent of the elastomer is sensitive to temperature, increasing approximately linearly as the temperature increases. The value of this quantity at low temperatures (20°C to 30°C) is expected to impact the temperature change for the loose rotor. Results of sensitivity analysis 6 show that a 10% increase in the loss tangent creates an increase of 9.3% in the peak predicted temperature. At high temperatures, the pump response is expected to be sensitive to both the absolute value and the slope of the curve relating $\tan\delta$ to temperature. The slope of the curve (increase in $\tan\delta$ per unit temperature) is reduced from the original value by 10% for sensitivity analysis 7. The resulting temperature increase is 7% lower than in the original analysis.

Sensitivity analyses 8 and 9 show the thermomechanical response of the stator is sensitive to changes in the small-strain elastic modulus of the elastomer. An increase of 10% in the small-strain modulus at all temperatures results in an increase of 11.2% in the peak temperature change for the loose rotor (rotor 55) and 14.5% for the tight rotor (rotor 53).

A single thermomechanical analysis combining changes in the variables shown in Table 9.6 may be used to observe the effect of the combined increase on the peak predicted temperature. If the effects of each variable affect the peak temperature independently, it is expected that the overall increase in temperature will be approximately 132% of the original predicted temperature for rotor 55. The analysis shows an increase in the peak predicted temperature of 141%. It may be concluded that the peak predicted temperature increase for the 400 RPM analysis using rotor 55 could be as high as 4.95°C if each of the variables in sensitivity analyses 1, 4, 6, and 8 were in error by the amounts listed in Table 9.6. This would bring the predicted temperature increase to within 30% of the increase observed during testing, whereas the reported error from the original modelling results was 70%. This shows that the uncertainty in modelling variables may be creating a large part of the errors observed at low interferences. More sensitivity analysis and a smaller uncertainty in the modelling inputs would provide more insight into the accuracy of the thermomechanical modelling strategy.

9.7 Test Conclusions

The testing program provides evidence of significant temperature increases within progressing cavity pumps with representative rotor/stator interferences. For the pumps tested, the peak temperature change in the elastomer increases linearly with pump speed and nonlinearly with the rotor/stator interference.

Results of testing and thermomechanical modelling of the test conditions show some discrepancy, but this is considered to be reasonable given the amount of uncertainty in the elastomer material response and pump geometry. The primary comparison criterion between measured and predicted results is the temperature distribution in the stator elastomer. The distribution of temperature in the test stator is similar to that seen in thermomechanical modelling results, with the peak elastomer temperature occurring near the centre of the thickest section of elastomer. Thermomechanical models provide estimated peak temperature changes within 20% of the test values for high-interference rotors, while predicted temperature increases for loose rotors underestimate the test results by as much as 70%. The primary discrepancy between modelling and testing results appears to be in the relationship between temperature change and rotor/stator interference. A series of thermomechanical sensitivity analyses provide an indication of the potential errors in predicted temperature resulting from uncertainties in modelling inputs. The uncertainty in rotor/stator interference may account for a significant part of the error in the low-interference rotors. It is likely that the errors in modelling results are partly a result of the numerous errors that may result from testing procedures and modelling inputs and partly a result of inaccuracies in the modelling strategy. Testing was done using a pump with a p/d ratio of 1.85, which is considered to be low for a single-lobe pump. It was shown in Section 5.6 that the two-dimensional structural models for single-lobe pumps provided the best agreement with three-dimensional models for pumps with higher p/d ratios; correlation between modelling and testing results is expected to improve for such pumps . The discrepancy between testing and modelling results warrants further investigation.

10 CONCLUSIONS AND RECOMMENDATIONS

10.1 Conclusions

The analysis strategies developed through the course of this study add a valuable tool in the design of progressing cavity pumps (PCPs) and positive displacement motors (PDMs). The thermomechanical solution procedure enables the prediction of the stress and strain fields and temperature distribution in the stator elastomer during stabilised operation, which is the primary goal of the investigation.

Structural modelling work shows that the operation of a PCP or PDM is dependent on the path of the rotor within the stator. Consideration of the two-dimensional cross-sectional geometry without accounting for out-of-plane deformation effects is not an adequate method of quantifying elastomer response. In a single-lobe pump, three-dimensional geometrical effects cause the rotor to move in an elliptical path in the stator cross-section. This has implications for design parameters such as the seal stress between the rotor and stator and the peak effective stress in the elastomer. The most accurate method of determining the actual rotor path is to conduct a three-dimensional analysis. The three-dimensional result may then be used as a benchmark for two-dimensional models. Better agreement exists between results of two-dimensional and three-dimensional modelling as the pitch-to-diameter ratio of the pump increases. In this investigation, the rotor path in two-dimensional models was modified so the two-dimensional models would reflect hysteresis heat generation equivalent to that seen in three-dimensional models.

A hysteresis heat generation model that uses the results of static structural finite element analyses is an efficient way of quantifying the heat generated in a dynamic system without employing a viscoelastic material model within a dynamic finite element strategy. Readily available dynamic material properties are incorporated into the heat generation calculations to account for the viscoelastic response of the elastomer.

The elastomer in PCP and PDM applications is exposed to non-sinusoidal variations in stress and strain as the pump or motor operates. Fourier sine/cosine series provide an excellent method of characterising non-sinusoidal variations in the stress and strain fields in the elastomer for use in heat generation calculations. Using the Fourier series, hysteresis energy generated within the elastomer may be calculated exactly at each point of interest with a relatively simple calculation.

Elastomer temperatures may exceed the temperature of the downhole operating fluid considerably because of the hysteresis energy generated within the elastomer during operation. Thermal modelling shows that the operating temperature is generally highest at the thickest section of elastomer because of the poor thermal conductivity of the material. Boundary conditions at the inner profile and outside diameter of the stator may have a significant effect on the peak temperature and temperature profile in the stator cross-section.

The stress and strain states reported from static finite element analysis using nominal rotor and stator geometries may be drastically different from those that occur when the pump operates at its stabilised operating point. Thermal expansion of the elastomer caused by hysteresis heating may increase the rotor/stator interference considerably. Static and dynamic material responses may also be affected significantly by the temperature increase that results from hysteresis heating in the elastomer.

A thermomechanical solution strategy that accounts for thermal expansion effects and temperature-sensitive material properties is capable of characterising the response of the elastomer in the downhole environment. Testing shows that the analysis strategy provides a reasonable approximation to the stabilised temperature profile in a single-lobe stator over a range of representative speeds and interferences. Uncertainties in the geometry and material descriptions likely account for some of the discrepancy between measured and predicted temperature increases. It is impossible to quantify the errors caused by shortcomings of the modelling strategy without a better understanding of the uncertainties in modelling inputs.

10.2 Recommendations

The majority of this study is focussed on the development of an analysis strategy for determining the stabilised operating point in pump and motor stators. The conventional single-lobe progressing cavity pump is used in all sample models used to demonstrate the capabilities of the strategy. The generic nature of the structural, heat generation, thermal, and iterative modelling strategies should make the analysis of other types of single-lobe pumps and multi-lobe pumps and motors relatively easy. Three-dimensional effects must be addressed in each case. Of particular interest is the use of the iterative strategy to optimise positive displacement motor designs because of the extreme temperatures that are thought to develop in the stator.

Improvements to some of the modelling strategies developed in this study are possible. A more accurate depiction of the static response of the elastomer could be obtained using a temperature-sensitive hyperelastic material model. A better understanding of three-dimensional effects in pumps and motors could also be obtained. The comparisons between two- and three-dimensional models described in Section 5.6 were performed in the context of heat generation, not structural response. In particular, differential pressure effects should be further investigated. Another possible improvement is the incorporation of a non-linear viscoelastic model for describing dynamic response that could provide more accuracy in heat generation calculations. Thermal modelling could be improved with a better understanding of the fluid mechanics and heat transfer mechanisms within stator cavities. This would also provide more insight into the nature of the friction that occurs between the rotor and stator.

The ability to predict the stabilised structural and thermal operating conditions in the stator elastomer provides a missing link in the process of optimising pump and motor operating life. With the stabilised structural analysis results, failure modes such as elastomer fatigue or temperature degradation of elastomer properties may be addressed on a quantitative basis.

The immediate benefit of this work is that the thermomechanical modelling strategy may be employed for design purposes. More accurate sizing and a better estimation of actual rotor position should generate more efficient pumps that will generate less heat to produce the same amount of sealing capability over a longer period of time.

REFERENCES

[1] Moineau, R. J. L., "Gear Mechanism", U.S. Patent #1892217, Dec. 27, 1932, Pages 1-9.

[2] Tirapolsky, W., *Hydraulic Downhole Drilling Motors: Turbodrills and Positive Displacement Rotary Motors*, Gulf Publishing Company, 1985.

[3] Gent, A.N., "Rubber Elasticity: Basic Concepts and Behavior." *Science and Technology of Rubber*, Eirich, F. R., Ed., Academic Press, Pages 1-21, 1978.

[4] Charlton, D.J., Yang, J., Teh, K.K., "A review of methods to characterise rubber elastic behaviour for use in finite element analysis." *Rubber Chemistry and Technology*, Volume 67, Number 3, Pages 481-503, 1994.

[5] Kramer, O., Ferry, J.D., "Dynamic Mechanical Properties." *Science and Technology of Rubber*, Frederick R. Eirich, Ed., Academic Press, Pages 179-221, 1978.

[6] Lamba, R.G., Meinecke, E.A., "Dynamic Properties of Elastomers." Educational Symposium of The Energy Rubber Group, September 1995.

[7] Medalia, A.I., "Heat Generation in Elastomer Compounds: Causes and Effects." *Rubber Chemistry and Technology*, Volume 64, Number 3, Pages 481-492, 1990.

[8] Reed, T.F., "Heat buildup of dynamically loaded engineering elastomeric components - I". *Elastomerics*, Volume 121, Number 12, Pages 22-28, 1989.

[9] Reed, T.F., "Heat buildup of dynamically loaded engineering elastomeric components - II". *Elastomerics*, Volume 121, Number 12, Pages 28-35, 1989.

[10] Mackerle, J., "Rubber and rubber-like materials, finite-element analyses and simulations: a bibliography (1976-1997)". *Modelling and Simulation in Materials Science and Engineering*, Volume 6, Number 2, Pages 171-198, 1998.

[11] Bathe, K-J., *Finite Element Procedures*, Prentice-Hall, 1996.

[12] McAllen, J., Cuitino, A.M., Sernas, V., "Numerical investigation of the deformation characteristics and heat generation in pneumatic aircraft tires Part II. Thermal Modeling." *Finite Elements in Analysis and Design*, Volume 23, Number 2-4, Pages 265-290, 1996.

[13] Charlton, D.J., Teh, K.K., "Thermo-mechanical FEA for rubber components." *Plastics, Rubber and Composites Processing and Applications*, Volume 23, Number 3, Pages 185-192, 1995.

[14] Sridhar, S, Prasad, N.S., Seetharamu, K.N., "Estimation of temperature in rubber-like materials using non-linear finite element analysis based on strain history." *Finite Elements in Analysis and Design*, Volume 31, Number 2, Pages 85-98, 1998.

[15] Brackbill, C.R., Lesieutre, G.A., Smith, E.C., Govindswamy, K., "Thermomechanical modelling of elastomeric materials". *Smart Materials and Structures*, Volume 5, Number 5, Pages 529-539, 1996.

[16] Sao-oui, P., Freakley, P.K., Oubridge, P.S., "Prediction of hysteretic temperature increase in rubber components by finite element analysis." *Plastics, Rubber, and Composites*, Volume 28, Number 2, Pages 69-73, 1999.

[17] Delpassand, M.S., "Mud Motor Stator Temperature Analysis Technique." *ASME Drilling Technology – Proceedings of the Energy Sources Technology Conference and Exhibition*, Pages 259-264, 1995.

[18] *ADINA/ADINA-T Version 7.3 Finite Element Software*, ADINA R&D, Inc., 1999.

[19] Beatty, J.R., Studebaker, M.L., "Physical Properties Required of a Rubber Compound". *Elastomerics*, Volume 109, Number 8, Page 35, 1977.

[20] *Theory and Modelling Guide, Volume 1: ADINA*, May 1999, Pages 251-263.

[21] Brown, R.P., *Physical Testing of Rubber*, Second Edition, Elsevier Applied Science Publishers, 1986.

[22] Sussman, T., Bathe, K-J., "A Finite Element Formulation for Nonlinear Incompressible Elastic and Inelastic Analysis." *Computers and Structures*, Volume 26, Number 1, Pages 357-409, 1987.

[23] Hepburn, C., Reynolds, R.J.W., eds., *Elastomers: Criteria for Engineering Design*, Applied Science Publishers Ltd, 1979.

[24] Cengel, J.A., Boles, M.A., *Thermodynamics: An Engineering Approach*, McGraw-Hill, Page 766, 1989.

[25] Hoffmann, W., "Nitrile Rubber". *Rubber Chemistry and Technology*, Volume 37, Number 2, Page 165, 1964.

[26] Incroprera, F. P., DeWitt, D.P., *Introduction to Heat Transfer (Second Edition)*, Wiley, 1990.

[27] Rosenhow, W.M., Hartnett, J.P., Ganic, E.N., Eds., *Handbook of Heat Transfer Fundamentals (Second Edition)*, McGraw-Hill Book Company, 1985.

APPENDIX A: SAMPLE CALCULATION – ITERATIVE ANALYSIS PROCESS FOR OPTIMISED CONVERGENCE

Refer to discussion in Section 8.2.5, *Convergence Optimisation*

Purpose:

To provide a method of estimating the stabilised temperature distribution in the elastomer based on the results of one or more iterations of the complete thermomechanical procedure described in Section 8.2.1. This procedure may be implemented after each thermomechanical iteration to expedite convergence.

Given:

- the radial interference, $i_{ambient}$, between the rotor and stator at ambient temperature, T_{amb};
- the temperature increase, $\Delta T(z)$, through the elastomer at the minor seal location (shown in Figure B.1) after the k^{th} thermomechanical iteration; and
- the thermal radial interference (from a structural FEA model), $\Delta i_{thermal}$, resulting from the temperature increase, $\Delta T(z)$.

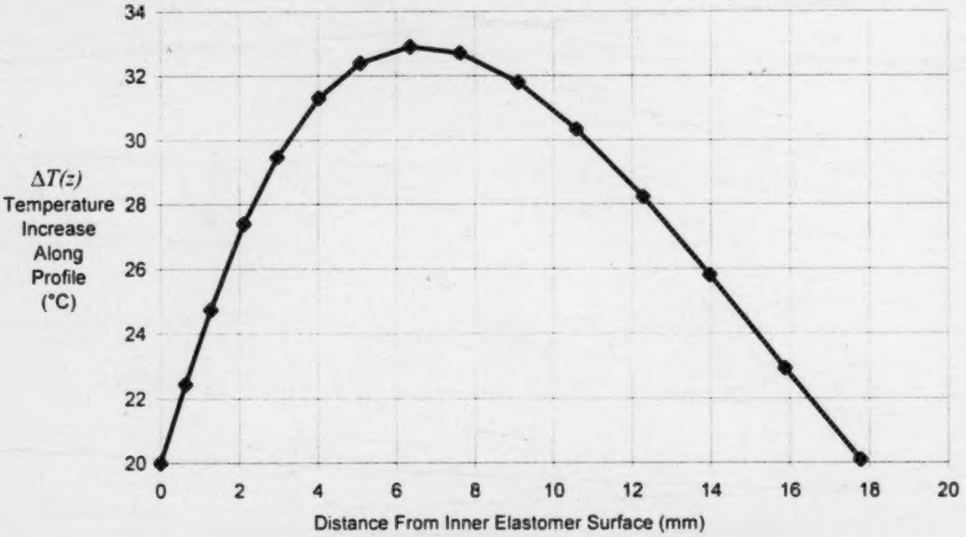

Figure B.1. Sample temperature profile through elastomer at minor diameter after thermomechanical iteration #1.

Three scalar parameters, A, B, and C, are required for the iteration procedure. Using the sample temperature profile shown in the above figure, B may be calculated. Scalar B is equal to the ratio of the peak elastomer temperature increase along the profile, $\Delta T(z)_{max}$, to the average temperature increase along the profile, $\Delta T(z)_{avg}$:

$$B = \frac{\Delta T(z)_{\max}}{\Delta T(z)_{avg}}. \qquad [B.1]$$

Here, $\Delta T(z)_{max}$ = 12.91°C and $\Delta T(z)_{avg}$ = 7.79°C. B =1.66.

Scalar C relates the observed increase in interference, $\Delta i_{thermal}$, to the thermal expansion coefficient of the elastomer. If a block of rubber with edge length L is subjected to a uniform temperature increase ΔT, the expected elongation on each side is:

$$\Delta L = L \cdot \alpha \cdot \Delta T. \qquad [B.2]$$

Using this equation and the average temperature along the profile, $\Delta T(z)_{avg}$, and assuming that the elastomer is free to expand in all directions, the change in interference at the minor seal is expected to be:

$$\Delta i_{calc} = t \cdot \alpha \cdot \Delta T(z)_{avg}, \qquad [B.3]$$

where t is the elastomer thickness at the minor seal. Here, t=17.998 mm, α=0.000160 1/°C, and $\Delta T(z)_{avg}$ is 7.79°C. The calculated value of the interference, Δi_{calc}, is 0.022 mm. The observed increase in interference, $\Delta i_{thermal}$, is much higher than the calculated value, at 0.060 mm. This discrepancy occurs because the elastomer is not free to expand in all directions. Scalar C is defined as the ratio of the observed to actual increases in interference,

$$C = \frac{\Delta i_{thermal}}{\Delta i_{calc}} \qquad [B.4]$$

and a value between 2 and 3 is expected because of the confinement present in the axial direction in the plane-strain model. In this case, C=2.73.

Using the results of the k^{th} iteration, a third scalar , A, may be calculated. A relates the peak temperature change in the elastomer to the total interference:

$$\Delta T(z)_{\max} = A(i_{ambient} + \Delta i_{thermal})^{n}, \qquad [B.5]$$

where the exponent n must be determined through other means. Through modelling, it has been observed that n is equal to 2 for temperature-insensitive material properties. This value of n will be used for this example. $\Delta T(z)_{max}$, $i_{ambient}$ and $\Delta i_{thermal}$ are known, so A may be calculated directly as 89.39.

Based on the values of A, B, and C, a prediction of the final temperature and interference may be obtained. The scalars B and C provide an indication of how much the minor interference will change for a given temperature increase. Given the temperature profile in Figure B.1, an estimate of the total interference may be calculated using:

$$i_1 = i_{ambient} + \alpha \cdot t \cdot \frac{C}{B} \cdot \Delta T_{\max}. \qquad [B.6]$$

The subscript in i_1 indicates the iteration number, as a number of iterations are typically required to find the final temperature. For the example, $i_{ambient}$ equals 0.381 mm and i_1 equals 0.441 mm.

Given the interference i_1, a corresponding temperature increase may be predicted using scalar A:

$$\Delta T_1 = A(i_1)^n \, . \qquad [B.7]$$

Here, ΔT_1 equals 17.35°C.

Next, the value of i_2 may be calculated using the same equation as i_1, but with ΔT_1 in place of ΔT_{max}. This procedure may be continued until the j^{th} temperature increase, ΔT_j, is within a specified tolerance of the increase observed in the $(j-1)^{th}$ iteration. Table B.1 shows the convergence pattern for the example over the eight iterations it takes for the solution to satisfy a convergence tolerance of 0.1°C.

Iteration Number	Total Interference (mm)	Temperature Change (°C)
0	0.3800	12.908
1	0.4406	17.350
2	0.4614	19.030
3	0.4693	19.686
4	0.4724	19.945
5	0.4736	20.048
6	0.4741	20.089
7	0.4742	20.105
8	0.4743	20.111

Table B.1. Convergence history for sample analysis.